Drift-Diffusion-Reaction Model for Time-Domain Analysis of Charging Phenomena in Electron-Beam Irradiated Insulators

Raftari Tangabi, Behrouz

DOI
10.4233/uuid:d823ad12-60ea-49d0-b8c0-0ccd1449387f

Publication date
2018

Document Version
Final published version

Citation (APA)
Raftari Tangabi, B. (2018). *Drift-Diffusion-Reaction Model for Time-Domain Analysis of Charging Phenomena in Electron-Beam Irradiated Insulators*. [Dissertation (TU Delft), Delft University of Technology]. https://doi.org/10.4233/uuid:d823ad12-60ea-49d0-b8c0-0ccd1449387f

Important note
To cite this publication, please use the final published version (if applicable).
Please check the document version above.

Drift-Diffusion-Reaction Model for Time-Domain Analysis of Charging Phenomena in Electron-Beam Irradiated Insulators

PROEFSCHRIFT

ter verkrijging van de graad van doctor
aan de Technische Universiteit Delft,
op gezag van de Rector Magnificus Prof.dr.ir. T.H.J.J. van der Hagen,
voorzitter van het College voor Promoties,
in het openbaar te verdedigen op
23 oktober 2018 om 12:30 uur

door

Behrouz RAFTARI TANGABI
Master of Science in Applied Mathematics, Amirkabir University of Technology, Iran

geboren te Gasreshirin

Dit proefschrift is goedgekeurd door de promotor en de copromotor.

Samenstelling promotiecommissie:

Rector Magnificus,	voorzitter
Prof.dr.ir. C. Vuik	Technische Universiteit Delft, promotor
Dr. N.V. Budko	Technische Universiteit Delft, copromotor

Onafhankelijke leden:

Prof.dr. U. Ebert	Technische Universiteit Eindhoven CWI, Amsterdam
Dr.ir. S. Sluyterman	FEI Company, Eindhoven
Dr. C.W. Hagen	Technische Universiteit Delft
Prof.dr. B.J. Thijsse	Technische Universiteit Delft
Prof.dr.ir. A.W. Heemink	Technische Universiteit Delft

TU Delft

Drift-Diffusion-Reaction Model for Time-Domain Analysis of Charging Phenomena in Electron-Beam Irradiated Insulators
Dissertation at Delft University of Technology.

ISBN 978-94-6186-960-9

Printed by: ProefschriftMaken || www.proefschriftmaken.nl
Cover design by: ProefschriftMaken || www.proefschriftmaken.nl

Dedicated to my father-in-law, Hussein Amirkhani, who was one of the most good-natured and honourable men I've ever met in my life.

Contents

Samenvatting

Elektronenmicroscopen maken gebruik van een bundel elektronen om een monster te verlichten en halen de benodigde informatie uit de interactie van deeltjes met materie om een beeld met hoge resolutie te produceren. De belangrijkste onderzoeksvraag van de huidige studie is ontstaan uit het feit dat deze resolutie vermindert wanneer een gegeven exemplaar isolatiematerialen bevat. In de elektronenmicroscopie van isolatoren staat het effect achter de afbraak van een beeldresolutie bekend als het oplaadeffect. Het oplaadeffect moet in het bijzonder worden bestudeerd en begrepen, omdat biologische monsters ofwel isolatoren zijn of isolerende delen bevatten.

Hoewel laadverschijnselen toepassingen hebben gevonden en voor sommige gebieden gunstig zijn geweest, zoals elektrostatische replicatie en op triboelektriciteit gebaseerde apparaten, is het opladen vaak destructief en kan het apparaten beschadigen. Daarom is het doel om het laden te elimineren, of op zijn minst het effect ervan te minimaliseren, en hiervoor is een duidelijk begrip van de betrokken factoren essentieel. In de literatuur zijn verschillende strategieën voorgesteld om het oplaadeffect te minimaliseren, en de meeste daarvan verschaffen zorgen voor een doorgang voor ladingen weg van het monster. Een metalen coating van het monster is waarschijnlijk de meest praktische manier om opladen tijdens beeldvorming bij elektronenmicroscopie te voorkomen. Het verwarmen van het monster en het aanpassen van de bundelspanning en stroom zijn ook nuttig gebleken bij het verminderen van de lading. Echter, dezelfde of soortgelijke behandelingen kunnen niet worden toegepast op alle gebieden die worden blootgesteld aan de destructieve effecten van opladen.

De natuurkundige basis achter het opladen van isolatoren is goed begrepen. Wanneer echter al deze relevante natuurkunde in één wiskundig model wordt samengevoegd, wordt het model te gecompliceerd voor analytische behandeling en zijn numerieke simulaties onvermijdelijk.

De bovengenoemde complexiteit van laadfenomenen biedt voldoende rede-

nen om zowel experimenteel als theoretisch onderzoek uit te voeren. De natuurkunde is goed beschreven door de Boltzmann transportvergelijking aangevuld met botsingsmechanismen die specifiek zijn voor isolatoren. De wiskundige complexiteit van de Boltzmann transportvergelijking verhindert echter de directe numerieke oplossing op praktisch relevante schalen. De gebruikelijke benadering is om stochastische simulaties van deeltjestrajecten uit te voeren met de Monte Carlo (MC) methode, wat overkomt met de statistische schatting van de kansdichtheidsfunctie beschreven door de Boltzmann transportvergelijking. MC-simulaties van in de tijd varirende kansdichtheidsfunctie's zijn uiterst moeilijk en hebben grote verschillen. Daarom richt het merendeel van het onderzoek zich op het simuleren van het everwicht van het systeem, en niet op het tijdsafhandelijke gedrag dat voorafgatt aan het everwicht.

De tijdsdomeinanalyse van laadfenomenen is de focus van dit proefschrift. Daartoe hebben we een dynamisch continuümmodel ontwikkeld op basis van de eerste twee momenten van de Boltzmann transportvergelijking.

Het resulterende model, bekend als de Drift-Diffusion-Reaction (DDR) benadering, wordt veel gebruikt in simulaties van halfgeleiderapparaten. Het is echter niet direct toepasbaar op door elektronenstraal bestraalde isolatoren als gevolg van de aanvankelijk zeer niet-evenwichtstransport/ionisatiestadium en de mogelijkheid van elektronenemissie door het vacuüm-monsterinterface.

De belangrijkste bijdrage van het huidige proefschrift is een aangepast DDR-model dat een effectieve bronfunctie bevat die de injectie van primaire elektronen en de initiële ionisatiefase beschrijft, en een nieuwe randvoorwaarde die rekening houdt met zowel de emissie als de tegenstroom. Vergelijkingen van dit aangepast DDR-model zijn numeriek opgelost met de eindige-elementenmethode. Een optimale configuratie van de oplosser (onder de standaard beschikbare opties) is gevonden, inclusief de discretiseringsstrategie, de tijdintegrator, de niet-lineaire en lineaire solvers en preconditioners.

De tweede belangrijke bijdrage van dit proefschrift is de kalibratie van het voorgestelde model op basis van experimentele gegevens voor ongeladen isolatoren. Deze procedure maakt precieze afstemming mogelijk van de paar parameters waarvan de effectieve aard voortvloeit uit de modelbenaderingen. Een van deze parameters is de oppervlakte-recombinatiesnelheid van het monster-vacuüminterface, die hier is bepaald voor aluminiumoxide- en siliciumoxidemonsters. Een andere afgestemde parameter is de effectieve gemiddelde penetratiediepte van het primaire elektron, waarvan is gebleken dat het zich gedraagt volgens een algemeen gebruikte vergelijking voor hogere energieën, maar daarvan afwijkt bij lagere energieën.

Verder zijn de tijdsdomeinvoorspellingen van het aangepast DDR-model vergeleken met de voorspellingen van een alternatieve eendimensionale benadering. Hoewel de twee modellen algemene kwalitatieve en kwantitatieve overeenstemming vertonen, zijn er enkele verschillen in de waarde van het voor-

spelde oppervlaktepotentiaal bij hogere energien. Daaropvolgend onderzoek heeft aangetoond dat deze verschillen gedeeltelijk kunnen worden toegeschreven aan het effect van ladingscreening door de Dirichlet-rand in onze simulaties.

Ten slotte is het aangepast DDR-model toegepast om laadeffecten te simuleren in verschillende realistische scenario's. De evolutie van opbrengst en oppervlaktepotentiaal in de tijd is berekend voor aluminiumoxide- en siliciumoxidemonsters bestraald met geconcentreerde bundels van verschillende energieën en stromen. De beweging van de bundel over een samengesteld monster is ook gesimuleerd evenals de transmissieopbrengst van het membraan van een nieuwe deeltjesdetector.

Summary

Electron microscopes take advantage of a beam of electrons to illuminate a specimen and extract the needed information from the interaction of particles with matter in order to produce a high resolution image. The main research question of the present study arose from the fact that this resolution is degraded when a given specimen contains insulating materials. In the electron microscopy of insulators the effect behind the degradation of an image resolution is known as the charging effect. The charging effect needs to be studied and understood, in particular, since biological specimens are either insulators or contain insulating parts.

Although charging phenomena have found applications and have been beneficial in some areas such as electrostatic replication and triboelectricity based devices, the charging is often destructive and may damage devices. Therefore, the aim is to eliminate charging or at least to minimize its effect and in order to do so a clear understanding of the involved factors is essential. Several strategies have been proposed in the literature to minimize the charging effect and most of them provide a passage for charges away from the specimen. A metallic coating of the sample is probably the most practical way to prevent charging during imaging in electron microscopy. Heating the specimen and adjusting the beam voltage and current have also proven to be useful in reducing the charge. However, the same or similar treatments cannot be applied in all areas that are exposed to the destructive effects of charging.

The basic physics behind charging of insulators is well understood. However, when all this relevant physics is put together in one mathematical model the latter becomes too complicated for analytical treatment and numerical simulations are unavoidable.

The above-mentioned complexity of charging phenomena provides enough reasons to perform both experimental and theoretical investigations. The physics is well-described by the Boltzmann Transport Equation (BTE) supplemented with collision mechanisms specific to insulators. However, the

mathematical complexity of the BTE prevents its direct numerical solution on practically relevant scales. The usual approach is to perform stochastic simulations of particle trajectories with Monte Carlo (MC) method, which is equivalent to statistical estimation of the probability density function (PDF) described by the BTE. MC simulations of time-varying PDF's are extremely difficult and suffer from large variances. That is why the majority of MC studies aim at simulating the steady state of the system and say very little about the transient behavior preceding the steady state.

The time-domain analysis of charging phenomena is the focus of the present dissertation. To this end, we have developed a dynamic continuum model based on the first two moments of the BTE.

The resulting model, known as the Drift-Diffusion-Reaction (DDR) approximation, is widely employed in simulations of semiconductor devices. However, it is not directly applicable to e-beam irradiated insulators due to the initial highly non-equilibrium transport/ionization stage and the possibility of electron emission through the vacuum-sample interface.

The main contribution of the present Thesis is a modified DDR model that includes an effective source function describing the injection of primary electrons and the initial ionization stage, and a novel boundary condition that takes both the emission and the reverse currents into account. Equations of this modified DDR model have been solved numerically with the finite element method. An optimal configuration of the solver (among the standard available options) has been found including the discretization strategy, the time integrator, and the nonlinear and linear solvers.

The second major contribution of this Thesis is the calibration of the proposed model against experimental data for uncharged insulators. This procedure allows precise tuning of the few parameters whose effective nature stems from the model approximations. Among them is the surface recombination velocity of the sample-vacuum interface, which has been determined here for alumina and silica samples. Another tuned parameter is the effective mean penetration depth of the primary electron, which has been found to follow a commonly used formula for higher energies, but deviates from it at lower energies.

Further, the time-domain predictions of the modified DDR model have been compared to the predictions of an alternative one-dimensional approach. While the two models show general qualitative and quantitative agreement, there are some differences in the value of the predicted surface potential at higher energies. Subsequent investigation revealed that these differences can be partially attributed to the charge screening effect by the Dirichlet boundary in our simulations.

Finally, the modified DDR model has been applied to simulate charging effects in several practical scenarios. The evolution of yield and surface poten-

tial with time has been calculated for alumina and silica samples irradiated by focused beams of different energies and currents. The motion of the beam across a composite sample has also been simulated as well as the transmission yield from the membrane of a novel particle detector.

1 Introduction

1.1 Basic concepts

A microscope is an instrument used to produce an enlarged image of objects that are invisible or too small for the naked eye. The science of studying objects using microscope is called microscopy. There are many types of microscopes. The first invented and most common microscope is optical (or light) microscope which uses light to form an image of an object. Other types are: atomic force, near-field scanning, tunneling, acoustic and electron microscopes.

An electron microscope is a microscope that instead of light uses electrons to create an image of the object. The main advantage of using an electron microscope over a light microscope is a much higher resolution allowing to see much smaller objects in detail. Transmission electron microscope (TEM) and scanning electron microscope (SEM) are the two most common types of electron microscopes that are widely used in science and industry. Scanning electron microscopy is the main focus of the present research.

The scanning electron microscope uses a moving beam of electrons (primary electrons) to produce various signals from the specimen. These signals contain information about the specimen and can be used to form the final image. The origins of these signals are secondary electrons, backscattered electrons and x-rays each detected with a specific detector.

A specimen is either uniform or a composite of several materials. Materials can be categorised into three groups according to their electrical resistance: conductors, semiconductors and insulators. Conductors have a very low resistance while semiconductors and insulators have a much higher resistance. The difference in conduction can be explained by the band theory which distinguishes between the conduction band and the valance band. Electrons with relatively low energies occupy the valance band and are called valance elec-

trons. When a valance electron gains some energy it can leave the valance band, cross the energy band gap and end up in the conduction band. The width of the gap between the valance and conduction bands -the band gap- determines the conductivity of materials.

A conductor does not have a band gap and electron can move more or less freely subject to collisions. A semiconductor has a relatively small band gap and, for instance, room temperature is able to provide sufficient energy to transfer some electrons to the conduction band. The band gap is large in insulators so an electron from valance band should receive a high enough energy in order to cross the band gape.

What is of particular interest and importance here is that crossing the band gap, either from the valance band to the conduction band or vise versa, is usually not a direct process especially for those materials with a wide band gap like insulators. In fact, this is a multistep process involving trapping and detrapping of electrons at discrete energy levels inside the band gap. These energy levels are caused by the imperfections of the crystal lattice and are associated with spatially localized trapping sites. Basically, an insulator by its very nature has a significant amount of trapped electrons and accordingly also trapped holes. Any disturbance in the balance between the amount of trapped electrons and holes causes a charging effect and this effect is known to be a particular response of insulators to electron-beam bombardment in scanning electron microscopy. This charging effect needs to be studied and understood since it degrades the quality and complicates the interpretation of images in scanning electron microscopy and is important in other applications, such as particle detectors.

1.2 Literature review and motivation

Charging phenomena in insulators have long been studied due to their importance in such areas as scanning electron microscopy (SEM), memory-based technologies, particle detectors, ceramic surfaces, industrial cables, and the safety of spacecraft [1, 2, 3, 4, 5]. Probably, the earliest systematic studies of electron-irradiation effects in solids and charging phenomena in insulators, as parts of research on electrets, were carried out by B. Gross who has had a great impact on this research field. In his seminal works on irradiation phenomena [6, 7] Gross investigated the electron trapping and charge buildup in high-resistivity solid insulators bombarded with energetic electrons. Further studies by Gross and coworkers produced new experimental techniques and mathematical models [8, 9, 10, 11].

These and more recent [12, 13, 14, 15, 16, 17, 18] studies have not yet been able to provide a complete and coherent account of all observed phenomena.

This could be due to the prevailing emphasis on static (stationary) models [19, 20, 21] rather than time-domain analysis. Studying the dynamics of charging in time domain is especially important in the analysis of response times in particle detectors [2] and in designing novel scanning strategies for SEM [18]. The existing dynamic models are either one-dimensional [14, 15] or do not include some of the essential physical processes, e.g., dynamic recombination, trapping, etc [16, 17].

While the prevailing semi-classical Monte-Carlo (MC) method [22] makes very few assumptions about the complicated electron-sample interaction process, realizing its full theoretical potential is technically very challenging. First of all, MC simulations are slowed down by the need to continuously update the long-rage electrostatic potential. Secondly, it is computationally difficult to keep track of all the trapped and de-trapped electrons. Finally, achieving acceptable variance not only in particle numbers, but also in the times of events (e.g. emission times), may require a prohibitive number of statistical realizations.

For these and other reasons an alternative and in many ways a much simpler self-consistent approach originating in semiconductor physics has been proposed [23, 24, 15, 14, 25, 26, 27, 28]. This so-called Rostoc Program takes the current density point of view, considering currents rather than charge densities to be the fundamental quantities. Some of the advantages of the current-based approach are: the possibility to model the sample-vacuum interface via a reflection-transmission coefficient formalism and to include the reverse electrons returning to the sample into the model. On the other hand, it is more difficult to describe proper ohmic contacts in this way and it is hard to extend this approach to two and three spatial dimensions.

Instead of sampling the probability space, the drift-diffusion-reaction (DDR) approach, mainly used to model low-energy transport in semiconductors [29, 30], directly describes the space-time evolution of a continuous probability density function. The pertaining partial differential equations are obtained from the semi-classical Boltzmann equation applying the method of moments and a few assumptions about the distribution of particles over the momentum space. From the mathematical point of view the DDR approach assumes that the symmetric part of the secondary electrons (SE) probability density function is isotropic about the origin of the momentum space and is well-described by a shifted Maxwellian distribution. Some parts of the DDR model have already been applied to the SEM problem [16, 31, 17, 32, 33, 34]. However, these previous studies have omitted the trapping rate equations thereby missing an important feature of the charging dynamics. Also, the model employed relies on an MC treatment of the primary electrons (PE), their initial scattering, and the emission of the secondary electrons (SE) through the sample-vacuum interface. Hence, the question remains whether a fully self-consistent contin-

uum DDR model without any MC parts can adequately describe the charging of dielectric samples by a focused electron beam.

The main challenges one faces in developing a fully self-consistent DDR model for the SEM problem are: the non-equilibrium charge injection mechanism followed by the generation of secondary particles via ionization, the fact that secondary electrons may leave via the sample-vacuum interface, the back-coupling effect of the accumulated charges on the primary beam, and the multi-scale nature of the problem (spatial as well as temporal). Here we show that all these problems can be successfully solved and that the traditional DDR approach represents a viable alternative to MC simulations.

In our first publication [35] we argued that the DDR approach can be applied to electron-beam irradiated insulators if the initial high-energy transport stage is approximated by an empirical source function. We showed that this pulsed source function allows modeling both the short-time processes immediately following the primary electron (PE) impact and the long-time charge evolution due to sustained bombardment. Importantly, we demonstrated that the sustained irradiation can also be modeled by a continuous current source, which gives practically the same secondary electron (SE) emission current as the time-averaged SE emission produced by many single-impact pulsed sources.

However, the original DDR model [35] had serious shortcomings as well. First of all, it was not calibrated against experimental data. Although we were able to reproduce any SE yield at a chosen PE energy by tuning a single parameter – the surface recombination velocity at the sample-vacuum interface, it was not clear which yield should be taken as a reference, since yields tend to change over time and depend on beam currents. Secondly, using the same SE emission velocity for all PE energies resulted in curves not fully compatible with published SE yield data over the whole range of PE energies. And more seriously, the model produced nonphysical results in the case of prolonged irradiation. Namely, the surface potential at low PE energies could reach very large positive values, which is not possible, since positive potential attracts secondary electrons back to the sample leading to the neutralization of any potentials exceeding ~ 10 V.

We have identified the main reasons behind the bad long-time behavior of the original DDR approach [35]. These were the employed steady-state generation-recombination model, which is not really suitable for the analysis of transient effects, and the neglected reverse electron current. The electrons that are being pulled back to the sample by a positive surface potential are called reverse electrons (REs). Incorporating fully dynamic generation and recombination processes is relatively easy. Here we employ the so-called trap-assisted generation-recombination model, which also reduces the number of equations to be solved and charge species to be tracked.

In hybrid MC-DDR methods [16, 17] reverse currents are estimated with direct MC simulations of particle trajectories. Here we propose an alternative approach that keeps intact the self-consistent nature of the DDR model. Namely, we introduce a novel boundary condition at the sample-vacuum interface that accounts not only for the total number of electrons returning to the sample, but also for the spatial distribution of this reverse current along the sample interface.

We have also developed and implemented a clear calibration procedure for our DDR model. It uses the fact that certain types of yield measurements – the so-called standard-yield measurements – correspond to the situation where single PE impacts happen sufficiently far enough from each other across the sample surface for their mutual interaction to be neglected. As our code is able to simulate single impacts, its calibration can be performed in this single-impact mode.

1.3 Outline

This dissertation consists of five chapters and a conclusion followed by one appendix.

Chapter 2 starts with the general form of the Boltzmann transport equation (BTE) and describes the relevant physics concerning the interaction of energetic electrons with insulator. Owing to its complexity, the BTE in its original form is not the target for practical modeling purposes. Hence, in the Chapter 2 we describe the procedure to simplify the BTE towards a more practical DDR model. In the subsequent sections, the DDR model is discussed in more detail, including the charge generation/recombination mechanism and the boundary conditions required for the modeling of contacts and interfaces in SEM with a particular focus on the electron flow through the sample-sample interface. Charge injection with respect to different beam modes is discussed in a separate section of Chapter 2, including pulsed, focused and defocused beams. Chapter 2 ends with a summary of approximations assumed in the modified DDR model.

Our strategy for solving the DDR equations is described in Chapter 3, which starts with an introduction followed by a section on the importance of numerical scaling. The finite element method is introduced in Section 3.2. In later sections, we discuss the details of the solver including the weak form of DDR equations, the strategies for meshing, type and order of basis functions, linear/nonlinear system solver and the time integration method.

Chapter 4 is devoted to the calibration of the DDR solver against experimental data and comparison with other methods. In particular, the standard

yield of insulators is reproduced based on the investigation of a single electron-impact event. The standard yield data are used to study the relative influence of material parameters such as the trapping site densities and cross-sections, as well as to tune the maximum penetration depth of primary electrons and the surface recombination velocity of the sample-vacuum interface. Further, the proposed time-averaged source model for the sustained bombardment is validated by comparing it with the pulsed model. The last section of the chapter is devoted to comparing the results of the DDR model with a self-consistent one-dimensional approach.

Chapter 5 studies charging effect in insulators subjected to electron bombardment by focused stationary and moving electron beams. Simulation experiments for time-domain analysis of the SE yield and surface potential variations in e-beam irradiated insulators are presented followed by the quantitative analysis of a more realistic scenario with a moving beam, including a dynamic line-scan of a laterally inhomogeneous target. The final section of Chapter 5 deals with the simulation of electron emission from a thin membrane pertaining to the transmission electron multiplier (Tynode).

2

Carrier transport modelling

An in depth understanding of how charge carriers travel through a given medium requires both experimental and theoretical investigations. A formal theoretical model describing this transport in the semi-classical approximation is the Boltzmann Transport Equation (BTE). BTE was initially introduced for describing dilute gases at the kinetic level, but has found applications in modeling of charge carrier transport in semiconductors as well. In this chapter the BTE model is reduced to a simpler Drift-Diffusion-Reaction (DDR) model augmented with appropriate source function, generation-recombination mechanism and boundary conditions.

2.1 Drift-Diffusion-Reaction model

The general form of the BTE appropriate for semiconductor physics can be written as

$$\frac{\partial f}{\partial t} + \frac{\hbar}{m}\mathbf{k} \cdot \nabla_{\mathbf{x}} f + \frac{1}{\hbar}\mathbf{F} \cdot \nabla_{\mathbf{k}} f = \mathcal{S}, \tag{2.1}$$

where $f(\mathbf{x}, \mathbf{k}, t)$ is a probability density function (PDF), $\hbar$ is the reduced Plank constant, $\mathbf{k}$ is the wave vector, $\mathbf{F}$ is the force, $\nabla_{\mathbf{x}} = \langle \partial/\partial x, \partial/\partial y, \partial/\partial z \rangle$ and $\nabla_{\mathbf{k}} = \langle \partial/\partial k_x, \partial/\partial k_y, \partial/\partial k_z \rangle$. The right-hand-side of Eq. (2.1) corresponds to the effect of collisions, specifically, here the collision integral $\mathcal{S}$ describes the electron impact ionization and the electron trapping/detrapping (capture/emission) processes.

According to the Lorentz force law, the force $\mathbf{F}$ acting on a particle with the electric charge q and velocity $\mathbf{v}$ due to the electric field $\mathbf{E}$ and the magnetic field $\mathbf{B}$ is given by

$$\mathbf{F} = \pm q \left(\mathbf{E} + \mathbf{v} \times \mathbf{B} \right), \tag{2.2}$$

where the first and second terms represent the electric and magnetic forces. Neglecting the magnetic force (due to small carrier velocities) leads to the following form of the BTE:

$$\frac{\partial f}{\partial t} + \frac{\hbar}{m}\mathbf{k} \cdot \nabla_{\mathbf{x}} f - \frac{q}{\hbar}\mathbf{E} \cdot \nabla_{\mathbf{k}} f = \mathcal{S}, \quad \text{(for electrons)}. \tag{2.3}$$

The phase space is 6-dimensional $(\mathbf{x}, \mathbf{k}) = (x, y, z, k_x, k_y, k_z)$ and the particle probability density function f is defined in such way that

$$dN = f(\mathbf{x}, \mathbf{k}, t)\, d\mathbf{x}\, d\mathbf{k} \tag{2.4}$$

is the expected number of carriers in the phase space element $d\mathbf{x}\, d\mathbf{k}$ at time t. The total number of carriers in the considered domain can be obtained by integrating over the phase space

$$\begin{aligned} N &= \int_{\text{phase space}} f(\mathbf{x}, \mathbf{k}, t)\, d\mathbf{x}\, d\mathbf{k} \\ &= \int_{\text{position}} \int_{\text{wave vector}} f(\mathbf{x}, \mathbf{k}, t)\, d\mathbf{x}\, d\mathbf{k} \\ &= \iiint_{\text{position}} \iiint_{\text{wave vector}} f(x, y, z, k_x, k_y, k_z, t)\, dx\, dy\, dz\, dk_x\, dk_y\, dk_z. \end{aligned} \tag{2.5}$$

The BTE, in its most general form, is a seven-dimensional integro-differential equation (six dimensions in the phase space and one in time) that can be solved by one or another numerical method. The Monte Carlo approach is a stochastic method that includes complex energy band structure and scattering processes. Deterministic solution of the BTE is also possible by reducing it to a simplified form of such as drift diffusion (DD) or hydrodynamic (HD) models. The drift-diffusion approximation is the main focus of the present study and in this section we show how the DDR model can be derived from the BTE.

Considering the BTE for electron transport, the probability density function $f(\mathbf{x}, \mathbf{k}, t)$ describes electrons of all possible energies and momenta. We deal with two types of electrons in our model (Fig. 2.1): high-energy electrons that are able to move and also escape the sample, and low-energy electrons that can not escape, but can still move. Accordingly, if we consider these two energy bands, f can be expressed as follows:

$$f(\mathbf{x}, \mathbf{k}, t) = \begin{cases} f_a(\mathbf{x}, \mathbf{k}, t), & |\mathbf{k}| > k_a; \\ f_{ca}(\mathbf{x}, \mathbf{k}, t), & k_c \le |\mathbf{k}| \le k_a; \\ 0, & |\mathbf{k}| < k_c; \end{cases} \tag{2.6}$$

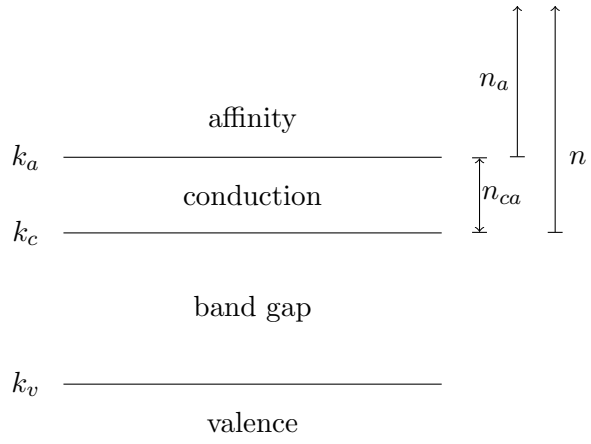

Figure 2.1: *Schematics of the energy-band diagram in DDR.*

where f_a and f_{ca} are the probability density functions that correspond to the high-energy electrons (above electron affinity), low-energy electrons (below electron affinity but inside the conduction band), respectively. The k_a and k_c denote the magnitude of the wave vectors corresponding to the electron affinity and the lower edge of the conduction band, respectively.

The function f can be rewritten as follows

$$f(\mathbf{x}, \mathbf{k}, t) = f_a(\mathbf{x}, \mathbf{k}, t) + f_{ca}(\mathbf{x}, \mathbf{k}, t), \tag{2.7}$$

where the extensions are defined as

$$f_a(\mathbf{x}, \mathbf{k}, t) = \begin{cases} f_a(\mathbf{x}, \mathbf{k}, t) & |\mathbf{k}| > k_a; \\ 0 & \text{Otherwise;} \end{cases} \tag{2.8}$$

and

$$f_{ca}(\mathbf{x}, \mathbf{k}, t) = \begin{cases} f_{ca}(\mathbf{x}, \mathbf{k}, t) & k_c \leq |\mathbf{k}| \leq k_a; \\ 0 & \text{Otherwise.} \end{cases} \tag{2.9}$$

The density of electrons in space-time can be obtained by integrating over $\mathbf{k}$. Therefore

$$\begin{aligned} n(\mathbf{x}, t) &= \int_{\mathbb{R}^3} f(\mathbf{x}, \mathbf{k}, t)\, d\mathbf{k} \\ &= \int_{\mathbb{R}^3} f_a(\mathbf{x}, \mathbf{k}, t)\, d\mathbf{k} + \int_{\mathbb{R}^3} f_{ca}(\mathbf{x}, \mathbf{k}, t)\, d\mathbf{k} \\ &= n_a(\mathbf{x}, t) + n_{ca}(\mathbf{x}, t), \end{aligned} \tag{2.10}$$

where n, n_a and n_{ca} are the densities of "free", energetic and low-energy electrons, respectively.

The first step towards simplifying the BTE can be achieved by integrating equation (2.3) over $\mathbf{k}$, which gives the first moment of the BTE

$$\int_{\mathbb{R}^3} \frac{\partial f}{\partial t}\, d\mathbf{k} + \frac{\hbar}{m} \int_{\mathbb{R}^3} \mathbf{k} \cdot \nabla_{\mathbf{x}} f \, d\mathbf{k} - \frac{q}{\hbar} \int_{\mathbb{R}^3} \mathbf{E} \cdot \nabla_{\mathbf{k}} f \, d\mathbf{k} = \int_{\mathbb{R}^3} \mathcal{S} \, d\mathbf{k}. \tag{2.11}$$

Since $\nabla_{\mathbf{k}} \cdot \mathbf{E} = 0$,

$$\frac{\partial n}{\partial t} + \frac{\hbar}{m} \nabla_{\mathbf{x}} \cdot \int_{\mathbb{R}^3} \mathbf{k} f \, d\mathbf{k} - \frac{q}{\hbar} \int_{\mathbb{R}^3} \nabla_{\mathbf{k}} \cdot (f\mathbf{E})\, d\mathbf{k} = S_n - R_n + G_n, \tag{2.12}$$

where S_n, R_n and G_n correspond to the impact ionization, trapping and de-trapping local rates, respectively.

Applying the divergence theorem, we obtain

$$\int_{\mathbb{R}^3} \nabla_{\mathbf{k}} \cdot (f\mathbf{E})\, d\mathbf{k} = \lim_{R \to \infty} \int_{S_R} (f\mathbf{E}) \cdot \boldsymbol{\nu} \, dS = 0, \tag{2.13}$$

where

$$S_R = \{\mathbf{k} \in \mathbb{R} \ \text{ such that } \ |\mathbf{k}| \leq R\}. \tag{2.14}$$

Therefore,

$$\frac{\partial n}{\partial t} + \frac{\hbar}{m} \nabla_{\mathbf{x}} \cdot \int_{\mathbb{R}^3} \mathbf{k} f \, d\mathbf{k} = S_n - R_n + G_n. \tag{2.15}$$

Intruding the concept of current density $\mathbf{J}_n$, Eq. (2.15) can be stated as

$$\frac{\partial n}{\partial t} + \nabla_{\mathbf{x}} \cdot \mathbf{J}_n = S_n - R_n + G_n, \tag{2.16}$$

where

$$\mathbf{J}_n = \frac{\hbar}{m} \int_{\mathbb{R}^3} \mathbf{k} f \, d\mathbf{k}. \tag{2.17}$$

The second moment of the BTE can be extracted by multiplying the equation (2.3) with $\mathbf{k}$ and integrating over $\mathbf{k}$, thus

$$\frac{\partial}{\partial t} \int_{\mathbb{R}^3} \mathbf{k} f \, d\mathbf{k} + \frac{\hbar}{m} \int_{\mathbb{R}^3} \mathbf{k} (\mathbf{k} \cdot \nabla_{\mathbf{x}} f)\, d\mathbf{k} - \frac{q}{\hbar} \int_{\mathbb{R}^3} \mathbf{k} (\mathbf{E} \cdot \nabla_{\mathbf{k}} f)\, d\mathbf{k} = \int_{\mathbb{R}^3} \mathbf{k} \mathcal{S} \, d\mathbf{k}. \tag{2.18}$$

The first term in the left-hand side simplified to

$$\frac{\partial}{\partial t}\int\limits_{\mathbb{R}^3} \mathbf{k} f \, d\mathbf{k} = \frac{m}{\hbar}\frac{\partial \mathbf{J}_n}{\partial t}. \tag{2.19}$$

Further we employ the relaxation-time approximation for the collision term $\mathcal{S}$:

$$\mathcal{S} \approx \frac{f_0 - f}{\tau}, \tag{2.20}$$

where f_0 is the equilibrium density function and τ is a time constant (relaxation time). This approximation and the symmetry of f_0 with respect to $\mathbf{k}$, i.e., $f_0\left(\mathbf{x}, |\mathbf{k}|\right)$, allow to simplify the term in the right-hand side of (2.18) as follows:

$$\begin{aligned}\int\limits_{\mathbb{R}^3} \mathbf{k}\mathcal{S} \, d\mathbf{k} &= \frac{1}{\tau}\int\limits_{\mathbb{R}^3} \mathbf{k}(f_0 - f) \, d\mathbf{k} \\ &= 0 - \frac{1}{\tau}\int\limits_{\mathbb{R}^3} \mathbf{k} f \, d\mathbf{k} \\ &= -\frac{m}{\tau\hbar}\mathbf{J}_n.\end{aligned} \tag{2.21}$$

If we split f into its two symmetric and anti-symmetric parts ($f = f_S + f_A$), for the second term in the left-hand side of the equation (2.18) we obtain

$$\begin{aligned}\frac{\hbar}{m}\int\limits_{\mathbb{R}^3} \mathbf{k}(\mathbf{k}\cdot\nabla_{\mathbf{x}} f) \, d\mathbf{k} &= \frac{\hbar}{m}\nabla_{\mathbf{x}} \cdot \int\limits_{\mathbb{R}^3} \mathbf{k}\mathbf{k} f \, d\mathbf{k} \\ &= \frac{\hbar}{m}\nabla_{\mathbf{x}} \cdot \int\limits_{\mathbb{R}^3} \mathbf{k}\mathbf{k} f_S \, d\mathbf{k} \\ &= \frac{\hbar}{m}\nabla_{\mathbf{x}} \cdot \int\limits_{\mathbb{R}^3} D_3 f_S \, d\mathbf{k},\end{aligned} \tag{2.22}$$

where

$$D_3 = \begin{pmatrix} k_x^2 & 0 & 0 \\ 0 & k_y^2 & 0 \\ 0 & 0 & k_z^2 \end{pmatrix}, \tag{2.23}$$

since the symmetry eliminates all the elements outside the main diagonal, i.e.,

$$\int\limits_{\mathbb{R}} k_l f_S \, dk_l = 0, \quad l = x, y, z. \tag{2.24}$$

Since

$$\int_{\mathbb{R}^3} k_x^2 f_S \, d\mathbf{k} = \int_{\mathbb{R}^3} k_y^2 f_S \, d\mathbf{k} = \int_{\mathbb{R}^3} k_z^2 f_S \, d\mathbf{k} = \frac{1}{3} \int_{\mathbb{R}^3} (k_x^2 + k_y^2 + k_z^2) f_S \, d\mathbf{k}, \tag{2.25}$$

we can relate this integral to the expected energy

$$\begin{aligned} \frac{\hbar}{m} \int_{\mathbb{R}^3} \mathbf{k}(\mathbf{k} \cdot \nabla_{\mathbf{x}} f) \, d\mathbf{k} &= \frac{\hbar}{m} \nabla_{\mathbf{x}} \cdot \frac{1}{3} I_3 \int_{\mathbb{R}^3} (k_x^2 + k_y^2 + k_z^2) f_S \, d\mathbf{k}, \\ &= \frac{\hbar}{3m} \nabla_{\mathbf{x}} \int_{\mathbb{R}^3} |\mathbf{k}|^2 f_S \, d\mathbf{k}, \\ &= \frac{\hbar}{3m} \nabla_{\mathbf{x}} \int_{\mathbb{R}^3} |\mathbf{k}|^2 f \, d\mathbf{k}, \\ &= \frac{2}{3\hbar} \nabla_{\mathbf{x}} \int_{\mathbb{R}^3} \frac{\hbar^2}{2m} |\mathbf{k}|^2 f \, d\mathbf{k}, \\ &= \frac{2}{3\hbar} \nabla_{\mathbf{x}} \mathcal{E}_n, \end{aligned} \tag{2.26}$$

where the expected electron energy is defined as

$$\mathcal{E}_n = \int_{\mathbb{R}^3} \frac{\hbar^2}{2m} |\mathbf{k}|^2 f \, d\mathbf{k}. \tag{2.27}$$

The last term on the left in the equation (2.18) can be simplified as follows:

$$\begin{aligned} \frac{q}{\hbar} \int_{\mathbb{R}^3} \mathbf{k}(\mathbf{E} \cdot \nabla_{\mathbf{k}} f) \, d\mathbf{k} &= \frac{q}{\hbar} \mathbf{E} \cdot \int_{\mathbb{R}^3} \mathbf{k} \nabla_{\mathbf{k}} f \, d\mathbf{k} \\ &= \frac{q}{\hbar} \mathbf{E} \cdot \int_{\mathbb{R}^3} \left(\nabla_{\mathbf{k}} (\mathbf{k} f) - f I_3 \right) \, d\mathbf{k} \\ &= -\frac{q}{\hbar} \mathbf{E} \cdot I_3 \int_{\mathbb{R}^3} f \, d\mathbf{k} + \frac{q}{\hbar} \mathbf{E} \cdot \int_{\mathbb{R}^3} \nabla_{\mathbf{k}} (\mathbf{k} f) \, d\mathbf{k} \\ &= -\frac{q}{\hbar} n \mathbf{E} + 0 \\ &= -\frac{q}{\hbar} n \mathbf{E}. \end{aligned} \tag{2.28}$$

Therefore, the equation (2.18) can be written as

$$\frac{\partial \mathbf{J}_n}{\partial t} + \frac{2}{3m} \nabla_{\mathbf{x}} \mathcal{E}_n + \frac{q}{m} n \mathbf{E} = -\frac{1}{\tau} \mathbf{J}_n. \tag{2.29}$$

As can be seen, equation (2.16) couples the zero's moment of f, i.e., n, to its first moments $\mathbf{J}_n$. Whereas, equation (2.29) couples the first moment $\mathbf{J}_n$ and the second moment $\mathcal{E}_n$. In the present case, considering f to be a shifted Maxwell distribution as shown in [36], the expected energy can be approximated as

$$\mathcal{E}_n \approx \frac{3}{2} k_B T_n n, \tag{2.30}$$

where k_B is the Boltzmann constant and T_n is the effective temperature.

Hence, the equation (2.29) becomes

$$\frac{\partial \mathbf{J}_n}{\partial t} + \frac{k_B}{m} \nabla_{\mathbf{x}} (T_n n) + \frac{q}{m} n \mathbf{E} = -\frac{1}{\tau} \mathbf{J}_n. \tag{2.31}$$

This equation can be further simplified by assuming that the time variation of the current density is relatively insignificant with respect to its magnitude, and that the effective temperature of electrons is spatially uniform. Therefore,

$$\mathbf{J}_n \approx -\frac{k_B \tau}{m} T_n \nabla_{\mathbf{x}} n - q \frac{\tau}{m} n \mathbf{E}. \tag{2.32}$$

This constitutes the drift-diffusion approximation of $\mathbf{J}_n$.

The system of the equations (2.16) and (2.32) is known as the transport equation for the free electron density. Expressing the electric field through its potential, $\mathbf{E} = -\nabla V$, the transport equation can be written in its common form:

$$\frac{\partial n}{\partial t} + \nabla \cdot \mathbf{J}_n = S_n - (R_n - G_n), \tag{2.33}$$

$$\mathbf{J}_n = -D_n \nabla n + \mu_n n \nabla V, \tag{2.34}$$

where

$$\mu_n = \frac{\tau}{m} q \quad \text{and} \quad D_n = \frac{\mu_n k_B T}{q}$$

are the electron mobility and the diffusion constant, respectively, and $\nabla = \nabla_{\mathbf{x}}$. The above relation between the electron mobility and the diffusion constant is known as the Einstein relation. Both the temperature and the relaxation time are lumped into the macroscopic mobility and diffusivity parameters. Although one might expect that these parameters become "effective" and require tunning, a perfect match against experimental data is obtained with the usual low-energy table values of μ_n and Einstein relation between μ_n and D_n.

By following a similar path, the transport equations for the free hole density is obtained as follows:

$$\frac{\partial p}{\partial t} + \nabla \cdot \mathbf{J}_p = S_p - (R_p - G_p), \tag{2.35}$$

$$\mathbf{J}_p = -D_p \nabla p - \mu_p p \nabla V, \tag{2.36}$$

where μ_p is the hole mobility and D_p is the diffusion coefficient.

The electrostatic potential $V(\mathbf{x}, t)$ satisfies the Poisson equation:

$$-\nabla \cdot (\varepsilon \nabla V) = \frac{q}{\varepsilon_0} \left(\frac{N_T}{2} + p - n - n_T \right), \tag{2.37}$$

where $V(\mathbf{x}, t)$ is the electrostatic potential and $n_T(\mathbf{x}, t)$ is the density of trapped electrons. As will be explained in Section 2.4 , $N_T/2$ is the equilibrium value of the trapped electrons density. Thus, the local excess of trapped electrons $n_T > N_T/2$ causes additional negative charging, whereas, the local lack of trapped electrons $n_T < N_T/2$ causes additional positive charging. The constant ε_0 is the dielectric constant of vacuum and the function $\varepsilon(\mathbf{x})$ is the (static) relative permittivity of the sample.

Thus, this method transforms the BTE into an infinite set of coupled moment equations. One can reduce this set to just a few equations by a process called *closure*, where the highest moment is approximated in terms of the lower ones.

2.2 Generation and recombination

Carrier generation is a process in which electron-hole pairs are formed by promoting an electron from the valence band into the conduction band and by that generating a hole in the valence band. The process where an electron falls down from the conduction band to annihilate a hole in the valence band, is called recombination of carriers. Several forms of generation/recombination mechanism are known in semiconductor physics, with the most common being the Auger and the Shockley-Read-Hall (SRH) models [30].

It is known that the Auger model is more appropriate at higher carrier concentrations caused, e.g., by heavy doping or high-level injection under concentrated sunlight. Therefore in the present case, where the concentrations are not that high, we opt for the SRH model. The SRH, also known as a trap-assisted generation/recombination, is a two step process that emits a phonon rather than a photon.

The process that causes low-energy charges in insulators to be transferred to a localized state is called trapping. Trapping occurs at a trapping site. The charges that have been trapped at a certain site at one time, due to several reasons, for instance, the field-induced detrapping, can get detrapped and become free at a later time. The process can continue which means, this free charge can get trapped again somewhere else [37]. A detailed analysis of the electron and hole trapping in insulators can be found in [38].

In the present approach the dynamic SRH model is implemented. Here we explain it along the lines of the PhD study by Robert Entner conducted at TU

Wien [29] (more detail in Appendix A). An attractive feature of this model is that there is no need to keep track of trapped holes as all the relevant physics is already contained in the single equation for the rate of electron trapping:

$$\frac{\partial n_T}{\partial t} = (R_n - G_n) - (R_p - G_p). \tag{2.38}$$

This process is coupled to the basic equations (2.33)–(2.37) and can be divided into four subprocesses as illustrated in Fig. 2.2.

(a) *Electron capture*: An electron from the conduction band gets trapped at the band-gap of the insulator and the surplus energy of $E_c - E_t$ is transmitted to the phonon emission. The expected rate of this process is

$$R_n = \sigma_n \upsilon_{th} n (N_T - n_T). \tag{2.39}$$

(b) *Hole capture*: A trapped electron moves to the valence band and neutralizes a hole (i.e. the hole is captured by the occupied trap), producing a phonon with the energy $E_t - E_v$. The corresponding rate is

$$R_p = \sigma_p \upsilon_{th} p n_T. \tag{2.40}$$

(c) *Hole emission*: An electron leaves a hole in the valence band and is trapped (i.e. the hole is emitted from the empty trap to the valence band). The energy $E_t - E_v$ is needed for this process, and the corresponding rate is

$$G_p = \sigma_p \upsilon_{th} n_i (N_T - n_T). \tag{2.41}$$

(d) *Electron emission*: A trapped electron moves to the conduction band. The required energy is $E_c - E_t$, and the rate is

$$G_n = \sigma_n \upsilon_{th} n_i n_T. \tag{2.42}$$

In the above equations: $\sigma_n(\mathbf{x})$ and $\sigma_p(\mathbf{x})$ are the electron and hole mean capture cross sections, $N_T(\mathbf{x})$ is the total density of traps, $n_T(\mathbf{x}, t)$ is the density of trapped electrons, $\upsilon_{th}(\mathbf{x})$ is the thermal velocity, and $n_i(\mathbf{x})$ is the intrinsic carrier density. The spatial variable $\mathbf{x}$ indicates the possibility of spatial inhomogeneity, i.e., the presence of different adjacent materials.

The initial conditions on n and p at $t = 0$ are set as the corresponding intrinsic carrier densities of the materials under consideration, whereas the initial condition for n_T has been derived based on the assumption of the initial steady state for the density of trapped electrons prior to the start of irradiation (i.e. $\partial n_T / \partial t = 0$) and is set to

$$n_T(\mathbf{x}, 0) = \frac{N_T(\mathbf{x})}{2}. \tag{2.43}$$

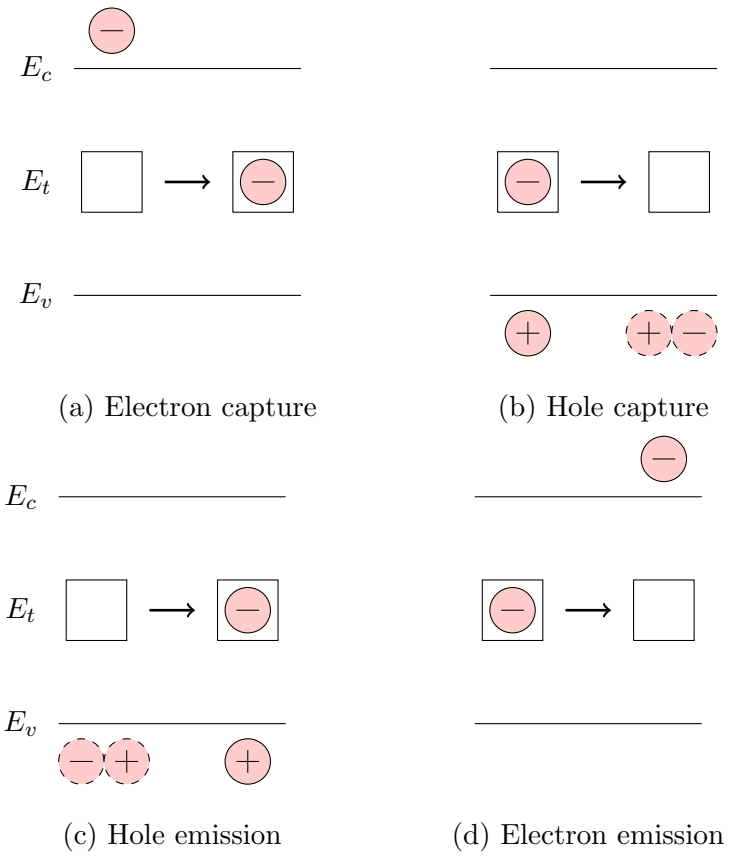

(a) Electron capture (b) Hole capture

(c) Hole emission (d) Electron emission

Figure 2.2: *Trap-assisted generation/recombination model.*

In the steady state, since electrons and holes are generated and recombined in pairs, we have the same rate function for the two species, and so

$$(R_n - G_n) = (R_p - G_p). \tag{2.44}$$

In this case, it is possible to simplify SRH model to the following form

$$R_{n,p} - G_{n,p} = \frac{np - n_i^2}{\tau_n(n + n_i) + \tau_p(p + n_i)}, \tag{2.45}$$

where τ_n and τ_p are the life time parameters for the electrons and holes, respectively. The carrier lifetime can be expressed in terms of the capture cross section and the density of traps

$$\tau_n = \frac{1}{\sigma_n v_{th} N_T}, \qquad \tau_n = \frac{1}{\sigma_n v_{th} N_T}. \tag{2.46}$$

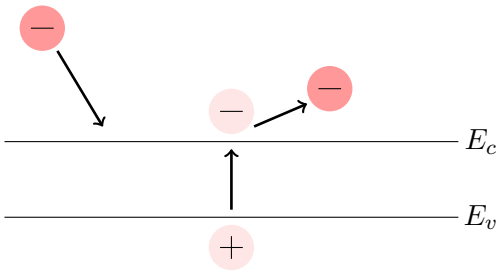

Figure 2.3: *Impact ionization due to high-energy particle.*

2.3 Charge injection and beam model

2.3.1 Impact of an individual primary electron

When an electron beam illuminates the sample some of the primary electrons will reflect as backscattered electrons, while the rest penetrates the sample and produces a number of secondary electrons/holes. The creation of charge carriers either by the impact of a high-energy charge carrier on a material or under the action a high electric field is known as *impact ionization* in semiconductor physics.

Impact ionization is a non-equilibrium three-particle generation process. The mechanism is functionally similar to the generation part of the Auger process. A highly energetic electron (hole) in the conduction band (in the valence band) collides with (transfers its energy to) an electron in the valence band and exciting it to the conduction band, and therefore leaving two electrons in the conduction band and a free hole in the valence ban (Fig. 2.3). The created electron-hole pair can also have a high enough energy in order to continue the process. Continuation of the process leads to an avalanche of carrier generation. At the end particles gradually lose their energies and eventually become thermalized.

Mathematically, the injection of electrons is described by the terms $S_n(\mathbf{x}, t)$ and $S_p(\mathbf{x}, t)$ in the right hand sides of the continuity equations (2.33) and (2.35).

The source function S_n reconciles the drift-diffusion approximation applied in (2.34) with the conservation law (2.33). To do so $S_n(\mathbf{x}, t)$ must correspond to the creation rate of only such electrons that satisfy (2.34), i.e., whose subsequent transport is governed by drift and diffusion. Here it is assumed that a suitable S_n can be represented as the product of two functions – $g_n(\mathbf{x})$ and $s(t)$.

Up to a normalization constant, the function $g_n(\mathbf{x})$ is the probability density function for the location of a secondary electron (created during ionization stage) at the time t_g when its transport can already be described by (2.33) and

(2.34). This function is approximated by an analytical expression based on various first-principals calculations, MC simulations and experimental data.

However, since the emission of SE's through the sample-vacuum interface often occurs in the time between the PE impact and t_g, one can not simply use $g_n(\mathbf{x})$ as the initial condition in the simulations. Therefore, the function $g_n(\mathbf{x})$ is used as a source and is multiplied with the rate function $s(t)$ that is the derivative of a function which equals zero at the time of impact and tends to unity at t_g, mimicking the avalanche-type ionization rate.

Note that the spatial extent of $g_n(\mathbf{x})$ allows for the creation of SE's also at the sample-vacuum interface where they can contribute to the emission current starting from the moment of impact up to t_g and beyond.

Thus, the source function has the form

$$S_{n,p}(\mathbf{x},t) = \begin{cases} g_{n,p}(\mathbf{x},E_0)s(t), & \text{if } 0 \le t \le t_{\mathrm{g}}; \\ 0, & \text{otherwise;} \end{cases} \tag{2.47}$$

where $g_{n,p}(\mathbf{x},E_0)$ is the charge distribution function depending on the effective energy of the primary electron, as will be explained shortly, and

$$s(t) = \frac{1}{L(t_g)-L(0)}\frac{dL}{dt}, \tag{2.48}$$

where L is the following logistic function:

$$L(t) = \frac{1}{1+\left(\frac{1}{w}-1\right)e^{-kt}}, \quad \frac{dL}{dt} = kL(1-L). \tag{2.49}$$

Here k is the Malthusian parameter and w is an initial condition related to the so-called carrying capacity ranging from 0 to 1. We choose L to be the logistic function since pair creation is an avalanche-type process and as such is mathematically similar to the population growth.

In (2.47) t_{g} denotes the generation time, which is taken here to be approximately the time of the ballistic flight of the primary electron. Special relativity provides a simple relation between the velocity of a primary electron and its energy:

$$v = c\sqrt{1-\frac{1}{\left(1+\frac{E_0}{mc^2}\right)^2}}, \tag{2.50}$$

where c is the speed of light in vacuum. The time of flight t_g can be estimated by dividing the penetration depth (will be explained below) by this velocity (or a twice lower 'average' velocity). In either case it appears that for the relevant range of primary energies t_{g} is in the order of femtoseconds, i.e.,

extremely short with respect to the average time between electron impacts in a typical SEM beam. If this estimate is correct, then the DDR model is indeed applicable to the charge dynamics not only on large time scales, but also on the scale of individual impacts.

Both source functions contain the semi-empirical distribution function of the charge pairs at the end of the initial ballistic stage [26]:

$$g_{n,p}(\mathbf{x}, E_0) = \left(A\frac{E_0}{E_\mathrm{i}} + B \right) \frac{1}{\pi R^3} \exp\left(-C|\mathbf{x} - \mathbf{x}_0|^2\right) \tag{2.51}$$

where E_0 is the beam energy and the effective landing energy of PE's, V_s is the surface potential at the point of PE impact, E_i is the pair creation energy, R is the maximum PE penetration depth (will be discussed further, in detail, in Chapter 4), C is a R-dependent factor, $\mathbf{x}_0$ is the center of the Gaussian distribution with the distance of $0.3R$ from the sample-vacuum interface, and A is the constant corresponding to the backscattering rate. In the hole distribution function g_p the constant B is zero, however, it is different from zero in the electron distribution function g_n accounting for the remaining PE's. Of course, the source functions proposed here are only approximations. Nevertheless, they are based on the best experimental evidence and first principles calculations available to date.

The pair creation energy E_i depends on the material of the sample via [15]

$$E_\mathrm{i} \approx 3\, E_\mathrm{g} + 1\,\mathrm{eV}, \tag{2.52}$$

with E_g denoting the energy gap of the material in eV.

For silicon, silicon dioxide, and aluminum oxide, with the backscattered rate of about 0.2, the three-dimensional Gaussian distribution of the secondary electrons and holes are:

$$\begin{aligned} g_n(\mathbf{x}, E_0) &= \left(11.58\frac{E_0}{E_\mathrm{i}} + 13.158 \right) \frac{1}{\pi R^3} \exp\left(-\frac{7.5}{R^2}|\mathbf{x} - \mathbf{x}_0|^2 \right), \\ g_p(\mathbf{x}, E_0) &= 11.58\frac{E_0}{E_\mathrm{i}} \frac{1}{\pi R^3} \exp\left(-\frac{7.5}{R^2}|\mathbf{x} - \mathbf{x}_0|^2 \right). \end{aligned} \tag{2.53}$$

The total numbers $N_{SE,SH}$ of secondary electrons and holes corresponding to the distribution (2.51) can now be estimated as

$$N_{SE} = N_{SH} \approx \iiint\limits_{\mathbb{R}^3, z \geq 0} g(\mathbf{x}, E_0) dV \approx 0.877 \frac{E_0}{E_\mathrm{i}}, \tag{2.54}$$

showing that approximately 88% of the effective energy is spent on the creation of charge pairs, which generally agrees with MC simulations. According to (2.54) the number of secondary electrons generated by one primary electron is somewhere between tens and thousands. Hence, we may expect the DDR approach to be a reasonable approximation at this scale.

2.3.2 Bombardment and temporal smoothing

Depending on the beam current primary electrons may arrive at an average rate as high as tens of millions per second. Previous applications of the drift-diffusion-reaction approach typically describe the SEM beam as a constant flux of electrons. Initially we would like to avoid the latter approximation and directly consider, say, m, primary electrons arriving at times t_i, $i = 0, 1, \ldots, m$. Thus, one obtains a pulsed source where the next PE arrives in a medium with some residual charge left from the impact of the previous PE.

Although, we gain some valuable insights about the subsurface charge dynamics and the effect of beam current, it is obviously too time consuming to consider bombardments of a sample by a large number of electrons in this way. Hence, a different approach is needed to study charging effects at larger time scales.

The main technical challenge preventing direct large-scale simulations with our method is the pulsed nature of the source terms requiring many time steps to be performed by the solver between electron impacts. A way to reduce the computational burden is to derive a smoother function describing the behavior of source terms at larger time scales. In the limit such a smoother source function should approach the constant beam currents of the other DDR models.

To achieve this we employ a temporal average of our source function, which also mimics the way the SEM response is measured (time-averaged yield, rather than the yield due to individual PE's). The average value of $S_n(\mathbf{x}, t)$ over a period of time T between the impacts can be expressed as

$$\bar{S}_n\left(\mathbf{x}, t_i + \frac{T}{2}\right) = \frac{1}{T}\int_{t_i}^{t_i+T} S_n(\mathbf{x}, t')dt', \tag{2.55}$$

and is a time-independent function. In what follows we call this a time-uniform or simply a uniform source.

Unfortunately, smoothing of the source has its price. Due to the presence of nonlinear terms in (2.37)–(2.35), solutions obtained with a time-averaged source term will not be the exact time-averaged values of the unknowns, but only the approximations thereof. Hence, to apply the DDR approach at both time scales successfully one needs to define constitutive relations and material parameters, such as the electron surface recombination velocity, for each scale separately. This is the so-called homogenization problem, typical for spatial multiscale analysis in physics (e.g. effective medium problem in electrodynamics).

Further, although a uniform source switched on at $t = 0$ may be expected to eventually produce a steady-state distribution of charge, it is an open theoretical question whether the actual pulsed source leads to the corresponding

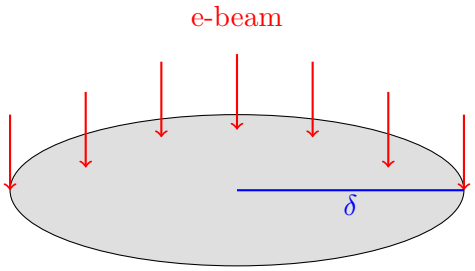

Figure 2.4: *Schematic for a broadened defocused beam.*

periodic charge variations.

The above discussion demonstrates that there are two possibilities within the DDR approach to model charge injection by a low- to moderate-energy electron beam via the source terms S_n and S_p. The first fine-scale model captures the discrete nature of the electron beam. The rate of particle production resolved at the level of pulses produced by individual PE impacts is given by:

$$S_{n,p}(\mathbf{x},t) = \sum_i \frac{g_{n,p}(\mathbf{x}, E_{\rm lan})}{L(t_{\rm g_i}) - L(t_{\rm s_i})} \frac{dL}{dt}(t - t_{\rm s_i}), \tag{2.56}$$

where i is the number of the particular individual PE, $t_{\rm s_i}$ is the i-th PE impact time, and $t_{\rm g_i}$ is the thermalization time of the generated electron-hole pairs.

To account for the action of the surface potential $V_{\rm s}$ on the primary electron, we introduce the landing energy $E_{\rm lan} = E_0 + V_{\rm s}(t_i)$, which should be applied in the distribution function instead of E_0. With single-impact events, due to a relatively small number of produced pairs, the continuous results of the DDR model should be interpreted as probability densities rather than particle densities, especially at lower PE energies.

The second model is designed for studying the sustained bombardment of the sample and is based on the temporal average of the above pulsed source function:

$$S_{n,p}(\mathbf{x},t) = \frac{j_0}{q} g_{n,p}(\mathbf{x}, E_{\rm lan}), \tag{2.57}$$

where j_0 is the average electron beam current.

In the continuous irradiation mode we consider two additional modifications of the source functions. One pertains to a defocused beam such that the computational domain is smaller than the beam radius. In this case we use the following distribution function derived from (2.51) by integrating over horizontal coordinates and enforcing the conservation of the amount of generated charge pairs:

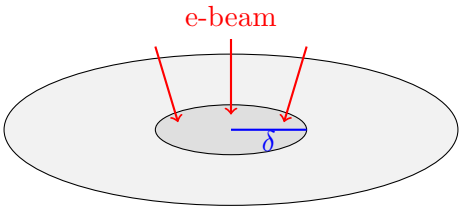

Figure 2.5: *Schematic for a partially focused beam.*

$$g_{n,p}(\mathbf{x}(r,z), E_{\text{lan}}) = A'_{n,p} \exp\left(-\beta|z - z_0|^2\right), \tag{2.58}$$

where

$$A'_{n,p} = \frac{1 - \exp(-\beta\delta^2)}{\beta\delta^2} A_{n,p}, \tag{2.59}$$

$$A_{n,p} = \left(A\frac{E_{\text{lan}}}{E_{\text{i}}} + B\right)\frac{1}{\pi R^3}, \qquad \beta = \frac{7.5}{R^2}, \tag{2.60}$$

and δ is the radius of the irradiated area (computational domain) at the surface (Fig. 2.4). Accordingly, the beam current can be calculated as

$$j_0 = i_0 \pi \delta^2, \tag{2.61}$$

where i_0 is the current density. The formula (2.61) adjusts the beam current to achieve results independent of δ.

If, on the other hand, the radius of a partially focused beam is smaller than the radius of the computational domain we resort to the following distribution:

$$\begin{aligned} g_{n,p}(\mathbf{x}(r,z), E_{\text{lan}}) = & \frac{1}{\beta\delta^2 + \exp(-\beta\delta^2)} A_{n,p} \times \\ & \begin{cases} \exp\left(-\beta|z - z_0|^2\right), & r \le \delta \\ \exp\left(-\beta(r^2 + |z - z_0|^2)\right), & r > \delta. \end{cases} \end{aligned} \tag{2.62}$$

Here δ denotes the beam radius rather than the radius of the computational domain (Fig. 2.5).

2.4 Boundary and initial conditions

The SEM chamber consists of two main parts – the vacuum and the sample. Considering a cross-section, we assume a rectangular outer boundary Fig. 2.6, which can be further adjusted to take the actual geometry into account. The domain is further divided into two parts, where one represents the sample and

the other the vacuum chamber. The Poisson equation (2.37) is considered on the whole domain (Ω_1 and Ω_2), whereas, equations (2.33), (2.35) and (2.38) are solved on the lower domain (Ω_2) only.

The boundary conditions on V, n, p at the interfaces of the sample with its holder and at the walls of the vacuum chamber are standard: Dirichlet at ohmic contacts and Neumann to simulate isolation and prevent any currents from flowing through the corresponding interface.

At ohmic contacts (for instance at Σ_3) the space charge vanishes, i.e.,

$$p - n = 0, \quad \text{on} \quad \Sigma_3 \times [0, t_{\text{end}}]. \tag{2.63}$$

Furthermore, the system is in thermal equilibrium there, which is expressed by the relation

$$np = n_i^2, \quad \text{on} \quad \Sigma_3 \times [0, t_{\text{end}}]. \tag{2.64}$$

From the above relations, we have

$$n(\mathbf{x}, t) = n_i, \quad p(\mathbf{x}, t) = n_i, \quad \text{on} \quad \Sigma_3 \times [0, t_{\text{end}}]. \tag{2.65}$$

We also assume homogeneous Dirichlet condition for the potential at ground or metallic contacts (ohmic contact) . i.e.

$$V(\mathbf{x}, t) = 0, \tag{2.66}$$

which could be easily adjusted to account for any finite value of the electric potential.

For an isolation (for instance at Γ), the condition should be such as to prevent any current through the interface and that means

$$\mathbf{J}_n \cdot \boldsymbol{\nu} = 0, \quad \mathbf{J}_p \cdot \boldsymbol{\nu} = 0, \quad \text{on} \quad \Gamma \times [0, t_{\text{end}}], \tag{2.67}$$

where $\boldsymbol{\nu}$ is the outward normal vector at the surface. These Robin-type boundary conditions set the sum of drift and diffusion currents equal to zero while applying zero Neumann condition for potential at the isolation side, the conditions (2.67) also turn into the following zero Neumann conditions for both free electrons and holes and in that case the drift and diffusion current are set to zero separately.

$$\frac{\partial n}{\partial \boldsymbol{\nu}} = 0, \quad \frac{\partial p}{\partial \boldsymbol{\nu}} = 0, \quad \text{on} \quad \Gamma \times [0, t_{\text{end}}], \tag{2.68}$$

Regarding the initial condition, the intrinsic carrier density has been considered for free charges

$$n(\mathbf{x}, 0) = n_i, \quad p(\mathbf{x}, 0) = n_i, \quad \text{in} \quad \Omega_2. \tag{2.69}$$

The density of trapped electrons in thermal equilibrium can be computed as follows:

$$n(\mathbf{x},0)=n_i,\quad p(\mathbf{x},0)=n_i,\qquad \text{and}\qquad \frac{\partial n_T}{\partial t}(\mathbf{x},0)=0. \tag{2.70}$$

Therefore,

$$\begin{aligned}&(R_n-G_n)=(R_p-G_p)\Rightarrow\\ &\sigma_n\upsilon_{th}n_i(N_T-n_T)-\sigma_n\upsilon_{th}n_in_T=\sigma_n\upsilon_{th}n_in_T-\sigma_p\upsilon_{th}n_i(N_T-n_T)\Rightarrow\\ &n_T(\mathbf{x},0)=\frac{N_T}{2}.\end{aligned} \tag{2.71}$$

Since the sample in equilibrium is electrically neutral the density of trapped holes is also obtained as

$$\begin{aligned}&p_T(\mathbf{x},0)+p(\mathbf{x},0)-n(\mathbf{x},0)-n_T(\mathbf{x},0)=0\Rightarrow\\ &p_T(\mathbf{x},0)+n_i-n_i-\frac{N_T}{2}=0\Rightarrow p_T(\mathbf{x},0)=\frac{N_T}{2},\end{aligned} \tag{2.72}$$

Thus, the local excess of trapped electrons $n_T > N_T/2$ causes negative local charging, whereas, the local lack of trapped electrons $n_T < N_T/2$ causes positive charging.

2.5 Sample-vacuum interface

The sample-vacuum interface, however, is not common in DDR-type simulations. Initially [35] we have used the following Robin-type boundary condition at this interface

$$\mathbf{J}_n\cdot\boldsymbol{\nu}=v_n(n-n_i)\quad\text{for}\quad n>n_i\quad\text{on}\quad\Sigma_2\times[0,t_{\text{end}}], \tag{2.73}$$

$$\mathbf{J}_p\cdot\boldsymbol{\nu}=0\quad\text{on}\quad\Sigma_2\times[0,t_{\text{end}}], \tag{2.74}$$

which sets the SE current density at the level proportional to the charge density at the boundary with the surface recombination velocity v_n controlling the magnitude of the current. This interface model can been obtained as a simplification of the SRH model [39].

2.5.1 Surface recombination velocity at sample-vacuum interface

The concept of surface recombination velocity is commonly used to model the charge recombination at the interface of two solids, especially for insulator-semiconductor interfaces; and so far we have not seen any use of this concept

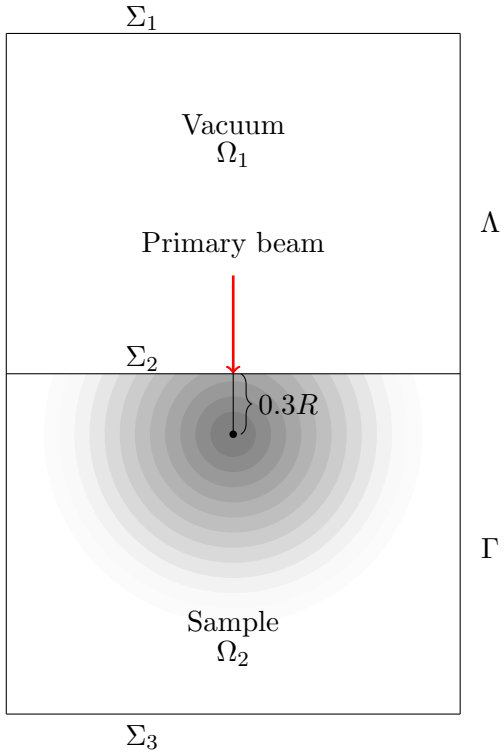

Figure 2.6: *General schematics of the problem.*

for the modeling of electron emission at the solid-vacuum interface. Therefore, the use of this concept in this particular area needs more justification and explanation. To this end, we examine the interpretation of this concept from the perspective of the BTE.

According to the definition of the current density introduced in Section 2.1, the normal component of the current density at the sample-vacuum interface can be expressed as follows

$$\mathbf{J}_n \cdot \boldsymbol{\nu} = \frac{\hbar}{m} \int_{\Omega_a} (\mathbf{k} \cdot \boldsymbol{\nu}) f(\mathbf{x}, \mathbf{k}, t)\, d\mathbf{k}, \tag{2.75}$$

where only electrons in the affinity band contribute to emission, i.e.,

$$\Omega_a = \{\mathbf{k} \in \mathbb{R}^3 \ : \ |\mathbf{k}| \geq k_a\}. \tag{2.76}$$

Employing the basic properties of integrals, the equation (2.75) can be

written as follows

$$\begin{aligned}\mathbf{J}_n \cdot \boldsymbol{\nu} &= \frac{\hbar}{m}\,(\mathbf{k}_c(t)\cdot\boldsymbol{\nu}) \int\limits_{\Omega_a} f(\mathbf{x},\mathbf{k},t)\,d\mathbf{k},\\ &= \frac{\hbar}{m}\,(\mathbf{k}_c(t)\cdot\boldsymbol{\nu})\; n_a(\mathbf{x},t)\\ &= \frac{\hbar}{m}\,(\mathbf{k}_c(t)\cdot\boldsymbol{\nu})\,(n(\mathbf{x},t) - n_{ca}(\mathbf{x},t))\,,\end{aligned} \tag{2.77}$$

where $\mathbf{k}_c(t)$ is a vector function of time.

We assume that

$$\begin{aligned}n_{ca}(\mathbf{x},t) &= n_i + \Delta n_{ca}(\mathbf{x},t)\\ &\approx n_i,\end{aligned} \tag{2.78}$$

which from the physical point of view means that the free electrons with energies below the affinity band will almost immediately be lost to trapping. Therefore, we have

$$\mathbf{J}_n \cdot \boldsymbol{\nu} = \frac{\hbar}{m}\,(\mathbf{k}_c(t)\cdot\boldsymbol{\nu})\,(n(\mathbf{x},t) - n_i)\,. \tag{2.79}$$

Hence, this leads to the introduction of the SRV as follows:

$$v_n = \frac{\hbar}{m}\,(\mathbf{k}_c(t)\cdot\boldsymbol{\nu}). \tag{2.80}$$

As expected, and as the equation (2.80) clearly shows, the SRV is a time-dependent parameter. The time dependent behavior of this parameter is such that it initially takes a positive value and then decreases with time, and eventually it reaches a certain lower bound. Indeed, this behavior is related to the fact that initially the free electrons are energetic and then they lose their energy over time.

In the single-impact study, it is in principle possible to use this parameter in its time-dependent form, and it will definitely lead to better understanding of the problem. While using it in other modes, such as the e-beam irradiation with the pulsed source model, would be troublesome and it is not compatible with the continuous source model.

Although the model may deviate somewhat from the actual physics, the scheme we propose to solve this problem is to use the effective time-average value of v_n. In fact, the SRV is determined by tunning against experimental data as a value independent of time, like other material properties. Thus, in addition to simplicity, the main advantage of the effective v_n is that it allows for long-term simulations.

2.5.2 The interface condition and reverse current

Equations (2.73)–(2.74) describe a semi-insulating contact for the electrons and an insulating contact for the holes (since holes cannot exist in vacuum). It should be noted however, this model does not account for the electrons that are being pulled back to the sample by a positive surface potential – the so-called reverse electrons (RE's). This leads to nonphysical results – very strong positive charging of samples under prolonged irradiation with low-energy beams.

Experiments show [40] that the energy of secondary electrons, although greater than the electron affinity of the material, rarely exceeds 10 eV. Therefore, even a relatively weak positive potential at the surface will pull back some of the secondary electrons. To account for this reverse current we propose the following modified version of the Robin-type boundary condition at the sample-vacuum interface:

$$\mathbf{J}_n \cdot \boldsymbol{\nu} = \begin{cases} v_n(n - n_i) - \alpha(\max(V^+))\dfrac{\partial V^-}{\partial \boldsymbol{\nu}}, & \text{if} \quad n > n_i; \\ 0, & \text{otherwise}, \end{cases} \tag{2.81}$$

$$\mathbf{J}_p \cdot \boldsymbol{\nu} = 0, \quad \text{on} \quad \Sigma_2 \times [0, t_{\text{end}}], \tag{2.82}$$

where

$$\frac{\partial V^-}{\partial \boldsymbol{\nu}}\,|_{\Sigma_2} = \begin{cases} \dfrac{\partial V}{\partial \boldsymbol{\nu}}|_{\Sigma_2}, & \text{if} \quad \dfrac{\partial V}{\partial \boldsymbol{\nu}} < 0; \\ 0, & \text{otherwise}, \end{cases} \tag{2.83}$$

$$\alpha(\max(V^+)) = \tag{2.84}$$

$$\begin{cases} 0, & \text{if} \quad \max(V^+) < V_{min}; \\ \alpha_{max}\frac{\max(V^+) - V_{min}}{V_{max} - V_{min}}, & \text{if} \quad V_{min} \le \max(V^+) < V_{max}; \\ \alpha_{max}, & \text{otherwise}, \end{cases}$$

$$V^+|_{\Sigma_2} = \begin{cases} V|_{\Sigma_2}, & \text{if} \quad V > 0; \\ 0, & \text{otherwise}, \end{cases} \tag{2.85}$$

$$\max(V^+) = \text{Maximum of} \;\; (V^+|_{\Sigma_2} - V_g), \tag{2.86}$$

and

$$\alpha_{max} = \frac{v_n \displaystyle\int_{\Sigma_2} (n - n_i) dA}{\displaystyle\int_{\Sigma_2} \frac{\partial V}{\partial \boldsymbol{\nu}} dA}, \tag{2.87}$$

where V_g is the applied potential at the upper boundary, which in the present study is set to zero ($V_g = V|_{\Sigma_1} = 0$ V). The term $-\alpha\frac{\partial V}{\partial \boldsymbol{\nu}}^-$ in (2.81) represents the reverse electrons current density. The function α controls the total magnitude of this current and the factor $-\frac{\partial V}{\partial \boldsymbol{\nu}}^-$ determines its spatial distribution. We assume that reverse electrons will re-enter the sample only through regions where the normal component of the electric field is negative. The stronger is the local attractive electric field, the higher is the density of reverse current at that location.

The function $\alpha(t)$ is chosen here in such a way, see (2.84)–(2.87), that the magnitude of the total reverse current varies linearly from zero, when the maximum surface potential $V^+(t)$ is below a certain value V_{min}, to the value of the total outward SE current, when $V^+(t)$ reaches V_{max}. This means that the net current through the sample-vacuum interface will be zero if $V^+(t) \geq V_{max}$ as all SE's leaving the sample will re-enter the sample as reverse electrons. Typically this leads to the surface potential never raising above V_{max} (or $V_{max}+V_g$). This choice of $\alpha(t)$ is not unique and could be further refined to take the energy spectrum of the SE's into account. One should also mention that, from the computational point of view, the mesh along the sample-vacuum interface should be fine enough in order to capture the gradient of the potential at the surface.

Since in the present case of zero extraction potential the attractive surface potential does not typically exceed the value of 10 V, the electrons of the reverse current will not have enough energy to cause any further ionization in the studied materials (ionization energy is in the order of 28 eV for both alumina and silica). Thus, no reverse electrons will be generated in the sample. In the situations where it is not the case, i.e., with positive surface potentials larger than the material ionization energy, our method would require further modification in the form of an additional source term – the creation rate of reverse electron-hole pairs.

Modeling issues for interfaces are common not only for the sample-vacuum interface, but also for other types of dissimilar material interfaces such as insulator-semiconductor, insulator-metal and semiconductor-metal interfaces. Although the charge-carrier behavior at interfaces has been studied for a long time and indeed is one of the oldest problems in condensed matter physics, the topic remains one of the fundamentally least understood. What can be both very difficult and absolutely essential in the interface modeling is the understanding of physical features such as the nature of interfacial characteristics, in order to arrive at how an interface behaves in the presence of charge carriers.

Among all types of interfaces, perhaps the insulator-semiconductor interface (like those in Metal-Insulator-Semiconductor (MIS) structure Fig. 2.7) is

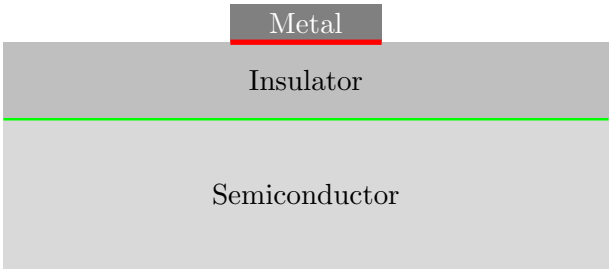

Figure 2.7: *Metal-Insulator-Semiconductor (MIS) structure.*

the easiest one to deal with, since the same physics holds for both of them, i.e., DDR is applicable for both without the need of any additional condition at the interface. The main difference is that the carrier mobility in an insulator is low (sometimes extremely low), while the charge carriers in a semiconductor have significantly higher mobility.

The study of metal-nonmetal interfaces leads to a more complex situation as the charge carriers exhibit substantially different behaviors in these two types of substances. This implies that together with applying DDR in the nonmetal part, an additional physics must be considered at the interface. In the present study the metal is always grounded; therefore, it is sufficient to only model the interface. For this purpose, one is referred to literature on modern semiconductor technology focusing on involving metal-insulator-semiconductor (MIS) [41, 42, 43], metal-oxide-semiconductor (MOS) [44] and metal-semiconductor-metal (MSM) [45] structures that have drawn a lot of attention due to their promising applications for memories, solar cells, transistors, sensors, etc. Admittedly, the topic is too wide to be appropriately covered in the present study, so we do not address the details and we only follow a common path leading to a proper mathematical model.

When a metal is brought into intimate contact with a semiconductor, a potential barrier is created between the two that prevents most charge carriers (electrons or holes) from passing through the interface and, indeed, only a small number of carriers have enough energy to get over the barrier and cross the interface. Depending on the combination of metal and semiconductor, two types of contacts can result. The contact may be rectifying (also called Schottky barrier contact), which only allows current to pass in one direction. Also, it could be ohmic, in which case current can pass in both directions. From the theoretical point of view, the factors that are playing a major role in this scenario are work function, electron affinity, Fermi level, valence band and conduction band. Among them, perhaps the most important one is the work function. In solid-state physics, the work function is the minimum energy required to remove an electron from a solid to escape to the vacuum outside

the solid surface.

3

Numerical solution of DDR equations

Determination of analytical solutions of partial differential equations is usually restricted to one dimensional problems and involves complex mathematical manipulation with many assumptions. To study PDEs, numerical methods are often needed to find approximate solutions.

The first step toward obtaining a numerical solution of an equation or a system of equations is to investigate the existence and uniqueness of the exact solution. With regards to the present model, the consistency analysis relies on previously published results. A detailed investigation of existence and uniqueness questions for stationary drift-diffusion equations can be found in [30]. In a study conducted by Jerome [46] a mathematical analysis of a system solution map for the weak form of the DDR model, which forms a basis for the numerical solution of the model, has been provided. Also, in a follow-up study by Busenberg et al. [47] the wellposedness of a DDR model similar to the present one (with different source/sink terms) has been demonstrated.

Our strategy for solving the DDR equations is described in this chapter. The chapter starts with a section on the importance of numerical scaling. The finite element method is introduced as the chosen numerical solver in Section 3.2. In later sections, we discuss the details of the solver including the strategies for meshing, type and order of basis functions, linear/nonlinear system solver and time integration method substantiating our choices with numerical evidence.

3.1 Numerical scaling

The problem is multiscaled in nature, hence to avoid numerical difficulties and maintain the accuracy of the solution, a simple scaling of variables has been performed. The scaling should not affect the solution, however, a proper

scaling can significantly affect the convergence rate by reducing the condition number of the matrix pertaining to the linear system arising from the discretization of PDEs. In solving nonlinear PDEs, like those in DDR model, a method, such as the Newton-Raphson method, is needed for solving nonlinear equations, where the scaling can also affect the convergence of the nonlinear solver.

To this end we introduce a set of characteristic dimensionless quantities. We denote the characteristic length scale by l^*, the characteristic time scale by t^* and the characteristic density scale by ρ^*. There is a relation between these values ($t^* = (l^*)^2$ and $\rho^* = (l^*)^{-3}$) that doesn't change the form of the equations, so that one only needs to introduce the rescaled versions for some of the constitutive parameters:

$$\begin{aligned} \tilde{n_i} &= \frac{n_i}{\rho^*}, \quad \tilde{\varepsilon} = \frac{\varepsilon}{\rho^*(l^*)^2}, \quad \tilde{\sigma}_{n,p} = t^*\rho^*\sigma_{n,p}, \\ \tilde{N_T} &= \frac{N_T}{\rho^*}, \quad \tilde{S}_{n,p} = \frac{t^*}{\rho^*}S_{n,p}. \end{aligned} \tag{3.1}$$

Also the boundary and initial conditions should be rescaled, since, e.g. the rescaled versions of the emission velocity and the function α are given by:

$$\tilde{v}_n = l^* v_n, \quad \tilde{\alpha} = \frac{\alpha}{\rho^*}. \tag{3.2}$$

In order to demonstrate the necessity of the scaling, simulations are performed with a cylindrical sapphire sample irradiated by a single PE of 2 keV. With the same configuration in terms of the mesh quality, the order of basis functions and etc, the result presented in Fig. 3.1 shows a considerable influence of not only the scaling itself but also of the value of characteristic parameters on the solution time of the simulation. We note that the length and time scales will also change while changing the density scale. All simulations in this thesis have been performed on a Debian Linux PC with an Intel(R) Core(TM) four-core 3.5 GHz CPU and 32 GB RAM.

3.2 FEM formulation

A variety of techniques is used to discretize partial differential equations: finite differences, finite elements, spectral methods etc. In spite of the differences in discretization strategies, fundamental concepts are pertinent to all of them.

Finite element theory has an elegant mathematical structure and numerical features that allows a priori and a posteriori estimates of discretization errors and convergence rates. Unfortunately a significant part of this theory relies on functional analysis which is outside the scope of our discussion here. Instead, we will provide an overview of important aspects based on numerical results.

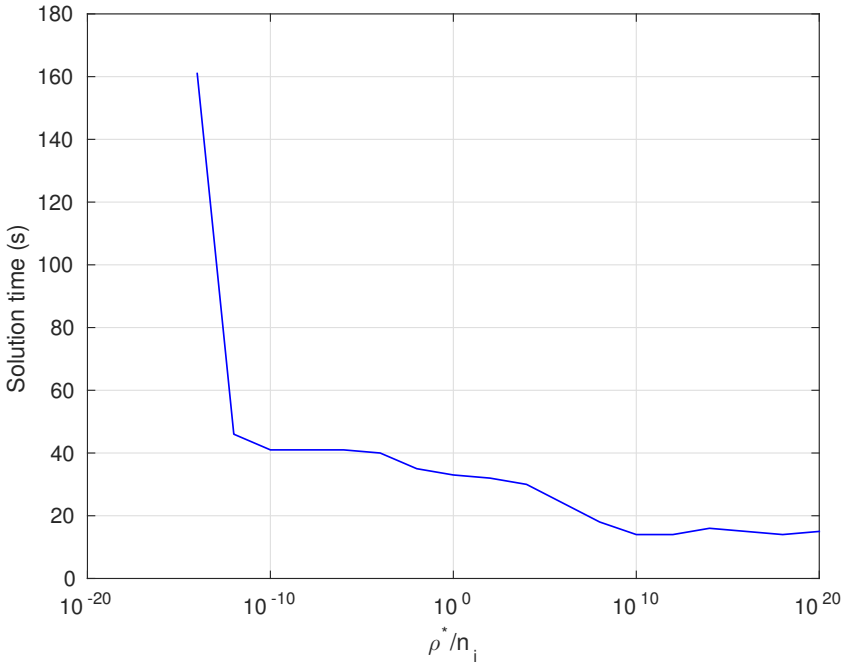

Figure 3.1: *The influence of the scaling on solution time corresponding to the simulation of a single impcat on the sapphire sample for the period of* 1 *ns.*

We employ the finite element method (FEM) for the numerical solution of the coupled system (2.33)–(2.38) and implement it as a solver within the COMSOL Multiphysics package. Although, there are many predefined modules and solvers in COMSOL, none of them can be directly applied with the present problem. The closest match is the semiconductor module. However, it is neither suited for studying the two different domains defined above, i.e., $\Omega_1 \cup \Omega_2$ for equation (2.37) and Ω_2 for the rest, nor does it allow to incorporate the additional equation (2.38). Therefore, we have opted for building a new model using the Weak Form PDE interface.

The concept of weak formulation can be explained from two different perspectives. The first is that the PDEs are derived from conservation laws of physical principles and these laws can be formulated as integral equations. Accordingly, this implies that weak-form equations are actually closer to the underlying physics than strong-form equations. While from the second perspective, the weak formulation allows for weaker assumptions concerning the smoothness of the solution, hence the name. Since, numerical schemes, such as FEM, are based on weak formulation, it is necessary to transform the classic equations into this form. This section deals with the derivation of weak form of the DDR in Cartesian and axisymmetric systems.

First we write down the problem in its strong form with reference to the domain shown in Fig. 2.6.

Find V, n, p and n_T satisfying the equations:

$$-\nabla \cdot (\varepsilon \nabla V) = \frac{q}{\varepsilon_0}\left(\frac{N_T}{2} + p - n - n_T\right) \quad \text{in} \quad (\Omega_1 \cup \Omega_2) \times [0, t_{\text{end}}], \tag{3.3}$$

$$\begin{aligned} &\frac{\partial n}{\partial t} + \nabla \cdot \mathbf{J}_n = S_n - (R_n - G_n) \quad \text{in} \quad \Omega_2 \times [0, t_{\text{end}}], \\ &\mathbf{J}_n = -D_n \nabla n + \mu_n n \nabla V, \end{aligned} \tag{3.4}$$

$$\begin{aligned} &\frac{\partial p}{\partial t} + \nabla \cdot \mathbf{J}_p = S_p - (R_p - G_p) \quad \text{in} \quad \Omega_2 \times [0, t_{\text{end}}], \\ &\mathbf{J}_p = -D_p \nabla p - \mu_p p \nabla V, \end{aligned} \tag{3.5}$$

$$\frac{\partial n_T}{\partial t} = (R_n - G_n) - (R_p - G_p) \quad \text{in} \quad \Omega_2 \times [0, t_{end}], \tag{3.6}$$

with the boundary conditions:

$$\begin{aligned} &V(\mathbf{x}, t) = 0 \quad \text{on} \quad (\Sigma_1 \cup \Sigma_3) \times [0, t_{\text{end}}], \\ &n(\mathbf{x}, t) = n_i \quad \text{on} \quad \Sigma_3 \times [0, t_{\text{end}}], \\ &p(\mathbf{x}, t) = n_i \quad \text{on} \quad \Sigma_3 \times [0, t_{\text{end}}], \end{aligned} \tag{3.7}$$

$$\begin{aligned} &\mathbf{J}_n \cdot \boldsymbol{\nu} = \begin{cases} v_n(n - n_i) - \alpha \dfrac{\partial V^-}{\partial \boldsymbol{\nu}}, & \text{if} \quad n > n_i; \\ 0, & \text{otherwise,} \end{cases} \quad \text{on} \quad \Sigma_2 \times [0, t_{\text{end}}], \\ &\mathbf{J}_p \cdot \boldsymbol{\nu} = 0, \end{aligned} \tag{3.8}$$

and the initial conditions:

$$\begin{aligned} &V(\mathbf{x}, 0) = 0 \quad \text{in} \quad (\Omega_1 \cup \Omega_2), \\ &n(\mathbf{x}, 0) = n_i \quad \text{in} \quad \Omega_2, \\ &p(\mathbf{x}, 0) = n_i \quad \text{in} \quad \Omega_2, \\ &n_T(\mathbf{x}, 0) = \frac{N_T}{2} \quad \text{in} \quad \Omega_2. \end{aligned} \tag{3.9}$$

3.2.1 Cartesian system

The weak formulation of equations (3.3)–(3.6) can be derived by multiplying the equations by so-called test (or weight) functions w_V, w_n, w_p and w_{n_T}, then integrating over the domains, arriving at:

$$\begin{aligned} &\int_{\Omega_1 \cup \Omega_2} w_V((-\nabla \cdot (\varepsilon \nabla V)) - Q)\ d\Omega = 0, \\ &Q = \begin{cases} \dfrac{q}{\varepsilon_0}(N_T/2 + p - n - n_T), & \text{in } \Omega_2 \\ 0, & \text{in } \Omega_1 \end{cases}, \end{aligned} \tag{3.10}$$

$$\int_{\Omega_2} w_n \left(\frac{\partial n}{\partial t} - \nabla \cdot (D_n \nabla n - \mu_n n \nabla V) - S_n + (R_n - G_n) \right) d\Omega = 0, \tag{3.11}$$

$$\int_{\Omega_2} w_p \left(\frac{\partial p}{\partial t} + \nabla \cdot (-D_p \nabla p - \mu_p p \nabla V) - S_p + (R_p - G_p) \right) d\Omega = 0, \tag{3.12}$$

$$\int_{\Omega_2} w_{n_T} \left(\frac{\partial n_T}{\partial t} - (R_n - G_n) + (R_p - G_p) \right)\ d\Omega = 0. \tag{3.13}$$

Applying the Gauss divergence theorem, the equations (3.10), (3.11) and (3.12) and can be written as

$$\int_{\Omega_1 \cup \Omega_2} ((\nabla w_V \cdot (\varepsilon \nabla V) - w_V Q) d\Omega - \int_{\partial\Omega_1 \cup \partial\Omega_2} w_V (\varepsilon \nabla V) \cdot \boldsymbol{\nu}\ d\Gamma = 0, \tag{3.14}$$

$$\begin{aligned} &\int_{\Omega_2} w_n \left(\frac{\partial n}{\partial t} - S_n + (R_n - G_n) \right)\ d\Omega + \int_{\Omega_2} \nabla w_n \cdot (D_n \nabla n - \mu_n n \nabla V)\ d\Omega \\ &- \int_{\partial\Omega_2 \cup \Sigma_2} w_n (D_n \nabla n - \mu_n n \nabla V) \cdot \boldsymbol{\nu}\ d\Gamma = 0, \end{aligned} \tag{3.15}$$

$$\begin{aligned} &\int_{\Omega_2} w_p \left(\frac{\partial p}{\partial t} - S_p + (R_p - G_p) \right)\ d\Omega - \int_{\Omega_2} \nabla w_p \cdot (-D_p \nabla p - \mu_p p \nabla V)\ d\Omega \\ &+ \int_{\partial\Omega_2 \cup \Sigma_2} w_p (-D_p \nabla p - \mu_p p \nabla V) \cdot \boldsymbol{\nu}\ d\Gamma = 0, \end{aligned} \tag{3.16}$$

where $\boldsymbol{\nu}$ is the outward unit normal vector at the boundary, $\partial\Omega_1 = \Lambda \cup \Sigma_1$ and $\partial\Omega_2 = \Gamma \cup \Sigma_3$. The weak form (3.13) remains the same as the spatial derivatives are not present in the trap rate equation.

The ground contact at Σ_1, ohmic at Σ_3 and isolation for the rest of the boundaries are considered. Since the boundary condition for the Poisson equation is homogeneous Dirichlet, the test and trial spaces are equal:

$$W_{te} = W_{tr} = \{w \in H^1(\Omega) : \quad w|_{\Sigma_1 \cup \Sigma_3} = 0\}, \tag{3.17}$$

where $H^1(\Omega)$ is the first-order Sobolev space.

For the transport equations, the trial and test spaces are different due to inhomogeneous boundary condition,

$$W_{te} = \{w \in H^1(\Omega) : \quad w|_{\Sigma_3} = 0\}, \tag{3.18}$$

$$W_{tr} = \{w \in H^1(\Omega) : \quad w|_{\Sigma_3} = n_i\}. \tag{3.19}$$

The test and trial spaces for the trap-rate equation are:

$$W_{te} = W_{tr} = \{w \in H^0(\Omega)\}, \tag{3.20}$$

where $H^0(\Omega)$ is the zero-order Sobolev space.

Accordingly, the weak formulations corresponding to the DDR equations under these assumptions are:

$$\int_{\Omega_1 \cup \Omega_2} ((\nabla w_V \cdot (\varepsilon \nabla V) - w_V Q) d\Omega = 0, \tag{3.21}$$

$$\begin{aligned} &\int_{\Omega_2} w_n \left(\frac{\partial n}{\partial t} - S_n + (R_n - G_n) \right) \, d\Omega + \int_{\Omega_2} \nabla w_n \cdot (D_n \nabla n - \mu_n n \nabla V) \, d\Omega \\ &+ \int_{\Sigma_2} w_n \left(v_n (n - n_i) - \alpha \frac{\partial V^-}{\partial \boldsymbol{\nu}} \right) \, d\Gamma = 0, \end{aligned} \tag{3.22}$$

$$\begin{aligned} &\int_{\Omega_2} w_p \left(\frac{\partial p}{\partial t} - S_p + (R_p - G_p) \right) \, d\Omega \\ &- \int_{\Omega_2} \nabla w_p \cdot (-D_p \nabla p - \mu_p p \nabla V) \, d\Omega = 0. \end{aligned} \tag{3.23}$$

The boundary conditions at ground and ohmic contacts are called essential here, since they should be satisfied explicitly. The boundary conditions at isolation and sample-vacuum interface are called natural, as they are implicitly satisfied by the weak formulations.

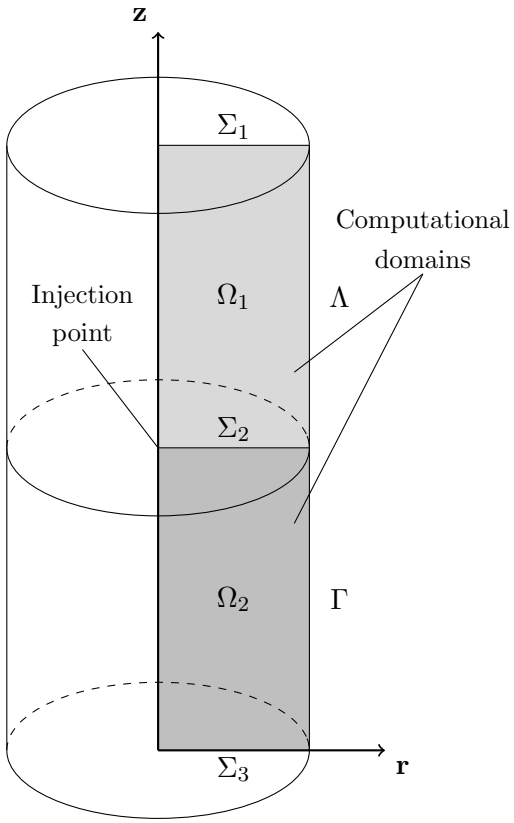

Figure 3.2: *Computational domain in the axisymmetric case.*

3.2.2 Axisymmetric system

In some cases, we reduce the original 3D problem to a 2D problem in the (r, z)-plane of the cylindrical coordinate system as the geometry, boundary conditions, and the source are all axially symmetric. Consider, for example, the cylindrical geometry presented in Figure 3.2. In the cylindrical coordinate system (r, θ, z) the PE beam impinging along the z-axis corresponds to the source term and boundary conditions independent of the angular coordinate θ. The solution will also be independent of θ and the original 3D model is reduced to a 2D model in the (r, z)-coordinates.

Consider the partial differential equations (3.3)–(3.6) in the axisymmetric geometry (see Fig: 3.2):

$$-\frac{1}{r}\frac{\partial}{\partial r}\left(\varepsilon r\frac{\partial V}{\partial r}\right) - \frac{\partial}{\partial z}\left(\varepsilon\frac{\partial V}{\partial z}\right) = Q(r, z), \tag{3.24}$$

$$\begin{aligned}&\frac{\partial n}{\partial t} - D_n\left(\frac{1}{r}\frac{\partial}{\partial r}\left(r\frac{\partial n}{\partial r}\right) + \frac{\partial^2 n}{\partial z^2}\right) + \mu_n\left(\frac{\partial n}{\partial r}\frac{\partial V}{\partial r} + \frac{\partial n}{\partial z}\frac{\partial V}{\partial z}\right)\\&+ \mu_n n\left(\frac{1}{r}\frac{\partial}{\partial r}\left(r\frac{\partial V}{\partial r}\right) + \frac{\partial^2 V}{\partial z^2}\right) = S_n - (R_n - G_n) \quad \text{in } \Omega_2,\end{aligned} \tag{3.25}$$

$$\begin{aligned}&\frac{\partial p}{\partial t} - D_p\left(\frac{1}{r}\frac{\partial}{\partial r}\left(r\frac{\partial p}{\partial r}\right) + \frac{\partial^2 p}{\partial z^2}\right) - \mu_p\left(\frac{\partial p}{\partial r}\frac{\partial V}{\partial r} + \frac{\partial p}{\partial z}\frac{\partial V}{\partial z}\right)\\&- \mu_p p\left(\frac{1}{r}\frac{\partial}{\partial r}\left(r\frac{\partial V}{\partial r}\right) + \frac{\partial^2 V}{\partial z^2}\right) = S_p - (R_p - G_p) \quad \text{in } \Omega_2.\end{aligned} \tag{3.26}$$

To derive the weak formulation we integrate over the cross-sectional area ($rdrdz$) arriving at the following form of the equation (3.24):

$$\int_{\Omega_1\cup\Omega_2} w_V\left(-\frac{1}{r}\frac{\partial}{\partial r}\left(\varepsilon r\frac{\partial V}{\partial r}\right) - \frac{\partial}{\partial z}\left(\varepsilon\frac{\partial V}{\partial z}\right) - Q\right) rdrdz = 0. \tag{3.27}$$

Integrating the highest-order terms by parts we obtain:

$$\begin{aligned}&-\int_{\Omega_1\cup\Omega_2} w_V\frac{\partial}{\partial r}\left(\varepsilon r\frac{\partial V}{\partial r}\right)drdz = \int_{\Omega_1\cup\Omega_2}\varepsilon\frac{\partial w_V}{\partial r}\frac{\partial V}{\partial r}rdrdz\\&-\int_{\partial\Omega_1\cup\partial\Omega_2}\varepsilon w_V\frac{\partial V}{\partial r}r\hat{\boldsymbol{\nu}}_r ds,\end{aligned} \tag{3.28}$$

$$\begin{aligned}&-\int_{\Omega_1\cup\Omega_2} w_V\frac{\partial}{\partial z}\left(\varepsilon\frac{\partial V}{\partial z}\right)rdrdz = \int_{\Omega_1\cup\Omega_2}\varepsilon\frac{\partial w_V}{\partial z}\frac{\partial V}{\partial z}rdrdz\\&-\int_{\partial\Omega_1\cup\partial\Omega_2}\varepsilon w_V\frac{\partial V}{\partial z}r\hat{\boldsymbol{\nu}}_z ds,\end{aligned} \tag{3.29}$$

where $\hat{\boldsymbol{\nu}} = \langle\hat{\boldsymbol{\nu}}_r, \hat{\boldsymbol{\nu}}_z\rangle$ is the outward unit normal vector at the boundary. Therefore, the weak form of the equation (3.24) can be written as:

$$\begin{aligned}&\int_{\Omega_1\cup\Omega_2}\varepsilon\frac{\partial w_V}{\partial r}\frac{\partial V}{\partial r}rdrdz = \int_{\Omega_1\cup\Omega_2}\varepsilon\frac{\partial w_V}{\partial z}\frac{\partial V}{\partial z}rdrdz\\&-\int_{\Omega_1\cup\Omega_2} w_V Qrdrdz = 0,\end{aligned} \tag{3.30}$$

or

$$\int_{\Omega_1\cup\Omega_2}\varepsilon(\nabla w_V\cdot\nabla V)rdrdz - \int_{\Omega_1\cup\Omega_2} w_V Qrdrdz = 0, \tag{3.31}$$

where $w_V\mid_{\Sigma_1\cup\Sigma_3} = 0$ and $\nabla = \langle\partial/\partial r, \partial/\partial z\rangle$.

The weak form of the equation (3.25) is:

$$\int_{\Omega_2} w_n \left(\frac{\partial n}{\partial t} - D_n \left(\frac{1}{r}\frac{\partial}{\partial r}\left(r\frac{\partial n}{\partial r}\right) + \frac{\partial^2 n}{\partial z^2}\right) + \mu_n \left(\frac{\partial n}{\partial r}\frac{\partial V}{\partial r} + \frac{\partial n}{\partial z}\frac{\partial V}{\partial z}\right) \right.$$
$$\left. + \mu_n n \left(\frac{1}{r}\frac{\partial}{\partial r}\left(r\frac{\partial V}{\partial r}\right) + \frac{\partial^2 V}{\partial z^2}\right) - S_n + (R_n - G_n)\right) r dr dz = 0, \tag{3.32}$$

Integrating the highest-order terms by parts we get:

$$\int_{\Omega_2} w_n \left(\frac{1}{r}\frac{\partial}{\partial r}\left(r\frac{\partial n}{\partial r}\right) + \frac{\partial^2 n}{\partial z^2}\right) r dr dz = -\int_{\Omega_2} \left(\frac{\partial w_n}{\partial r}\frac{\partial n}{\partial r} + \frac{\partial w_n}{\partial z}\frac{\partial n}{\partial z}\right) r dr dz$$
$$+ \int_{\Sigma_2 \cup \partial\Omega_2} r w_n \left(\frac{\partial n}{\partial r}\hat{\boldsymbol{\nu}}_r + \frac{\partial n}{\partial z}\hat{\boldsymbol{\nu}}_z\right) ds, \tag{3.33}$$

$$\begin{aligned}
&\int_{\Omega_2} w_n n \left(\frac{1}{r}\frac{\partial}{\partial r}\left(r\frac{\partial V}{\partial r}\right) + \frac{\partial^2 V}{\partial z^2}\right) r dr dz = \\
&-\int_{\Omega_2} \left(\frac{\partial (w_n n)}{\partial r}\frac{\partial V}{\partial r} + \frac{\partial (w_n n)}{\partial z}\frac{\partial V}{\partial z}\right) r dr dz \\
&+\int_{\Sigma \cup \partial\Omega_2} w_n n \left(\frac{\partial V}{\partial r}\hat{\boldsymbol{\nu}}_r + \frac{\partial V}{\partial z}\hat{\boldsymbol{\nu}}_z\right) r ds = \\
&-\int_{\Omega_2} n \left(\frac{\partial (w_n)}{\partial r}\frac{\partial V}{\partial r} + \frac{\partial (w_n)}{\partial z}\frac{\partial V}{\partial z}\right) r dr dz \\
&-\int_{\Omega_2} w_n \left(\frac{\partial (n)}{\partial r}\frac{\partial V}{\partial r} + \frac{\partial (n)}{\partial z}\frac{\partial V}{\partial z}\right) r dr dz \\
&+\int_{\Sigma \cup \partial\Omega_2} w_n n \left(\frac{\partial V}{\partial r}\hat{\boldsymbol{\nu}}_r + \frac{\partial V}{\partial z}\hat{\boldsymbol{\nu}}_z\right) r ds.
\end{aligned} \tag{3.34}$$

Therefore, the weak form of the equation (3.25) can be written as:

$$\begin{aligned}
&\int_{\Omega_2} w_n \left(\frac{\partial n}{\partial t} - S_n + (R_n - G_n)\right) r dr dz \\
&+\int_{\Omega_2} \nabla w_n \cdot (D_n \nabla n - \mu_n n \nabla V) r dr dz \\
&-\int_{\Sigma_2 \cup \partial\Omega_2} w_n (D_n \nabla n - \mu_n n \nabla V) \cdot \hat{\boldsymbol{\nu}}\, r ds = 0.
\end{aligned} \tag{3.35}$$

Substitution of the boundary conditions gives:

$$\begin{aligned}&\int_{\Omega_2} w_n \left(\frac{\partial n}{\partial t} - S_n + (R_n - G_n)\right) r dr dz \\ &+ \int_{\Omega_2} \nabla w_n \cdot (D_n \nabla n - \mu_n n \nabla V) r dr dz \\ &+ \int_{\Sigma_2} w_n \left(v_n(n - n_i) - \alpha \frac{\partial V^-}{\partial \boldsymbol{\nu}}\right) r ds = 0,\end{aligned} \tag{3.36}$$

where $n\,|_{\Sigma_3} = n_i$ and $w_n\,|_{\Sigma_3} = 0$.

Along similar lines the weak form of the equation (3.26) can be derived as:

$$\begin{aligned}&\int_{\Omega_2} w_p \left(\frac{\partial p}{\partial t} - S_p + (R_p - G_p)\right) r dr dz \\ &- \int_{\Omega_2} \nabla w_p \cdot (-D_p \nabla p - \mu_p p \nabla V) r dr dz = 0\end{aligned} \tag{3.37}$$

where $p\,|_{\Sigma_3} = n_i$ and $w_p\,|_{\Sigma_3} = 0$.

The above calculations reveal that despite differences in the strong form of the DDR equations in these two coordinate systems, the weak formulations have the same form and the only difference is in the integral elements, i.e. $rdrdz$ for the axisymmetric system and $dxdydz$ in the Cartesian case.

3.3 Mesh and refinement strategy

Simple uniform meshes are not suitable for the problem at hand, at least with the chosen simple scaling strategy. A coarse mesh may cause an instability resulting in negative values for the concentrations n and p. These negative values emerge around strong gradients in n, p, n_T and V.

The two common strategies of achieving more accurate finite element solutions are to decrease the mesh size (h-refinement) and to employ higher-order basis functions (p-refinement). These strategies can be used separately or in combination (hp-refinement). In fact, both of them are different ways of increasing the degrees of freedoms (Fig. 3.3).

Although p-refinement is known to be a powerful method of finding accurate solutions, h-refinement is more popular [48, 49]. Here, both strategies are evaluated, performing simulation with sapphire sample subjected to sustained bombardment with a focused beam of 2 keV and 1 nA. A simple approach to study the influence of h-refinement is to perform simulations on sequence of gradually refined meshes until the numerical solution is relatively stable.

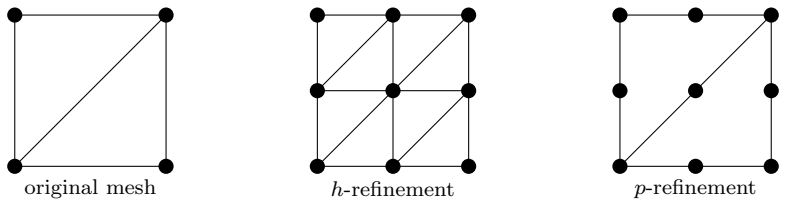

Figure 3.3: *Refinement strategies.*

Figure 3.4 compares solutions at time 10 ns for a sequence of meshes, starting with a uniform triangular mesh with the average element size of $h = 10$ nm followed by three uniform refinements with the element sizes $h/2$, $h/4$ and $h/8$. The images show the spatial distribution of the changes in the numerical values of n, p and n_T. The results indicate that, for sapphire irradiated with a 2 keV 1 nA beam, acceptable accuracy is achieved with the element size of about 2.5 nm for first-order basis functions. Simulations have also been performed with the same mesh size but increasing the order of basis functions. Solutions for different orders of basis functions are compared in Fig. 3.5.

It is obvious from the results that a careful mesh strategy is required for the impact zone and under the sample-vacuum interface, since the charge densities may be extremely concentrated around the impact zone and form very thin layers near the interface.

Automated adaptive mesh refinement is another widely used approach, which adds mesh elements based on an error criterion to resolve those areas where the error is large. We employ adaptive refinement only in the initial simulations to identify the regions where a fine mesh is needed and then fixed local refinement is used in the follow-up simulations. The L^2-norm of the gradient of the variables is chosen as the error indicator: $\|\nabla n\|_2 + \|\nabla p\|_2 + \|\nabla n_T\|_2$.

Conclusion drawn from adaptive mesh simulations confirm those obtained with manually refined meshes, and Figure 3.6 shows the general pattern of the locally refined mesh over the sample part, applying all types of contacts considered in our model. For an isolated contact, the gradient of all the quantities is expected to be very small, in fact, it should be zero in order to satisfy the applied homogeneous Neumann boundary condition for potential and charge concentrations, so further refinement is not needed for this contact. However, at the ohmic contact and at the sample-vacuum interface where the gradients can be steep, the mesh should be fine enough to capture the steepness. Moreover, for these contacts, the structure of the mesh should be getting gradually finer towards the contact.

In addition to the influence of contact type on the local refinement pattern, other factors should be considered namely, the primary energy and the beam

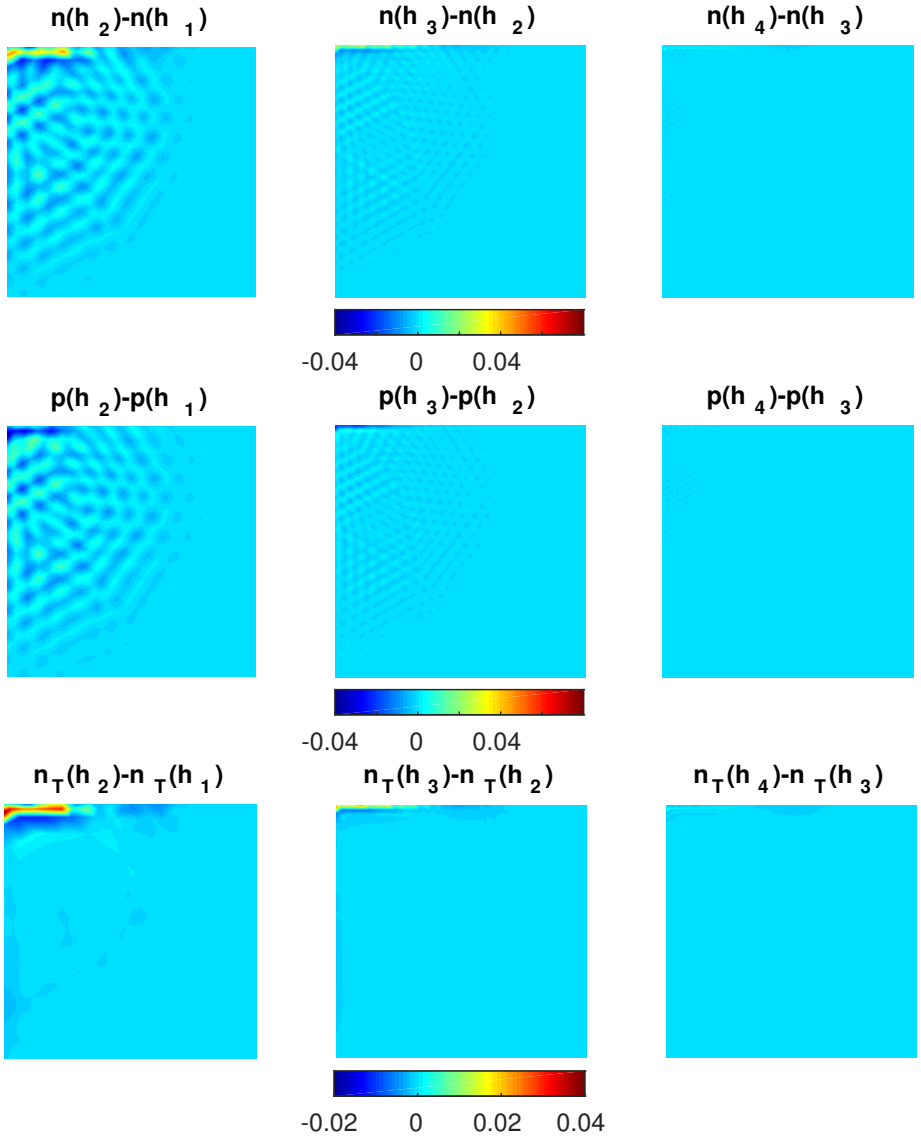

Figure 3.4: *The influence of h-refinement on the solution for a sapphire sample irradiated with a 2 keV 1 nA beam. The element sizes are* $h_1 \approx 10$ *nm and* $h_i = h_1/2^{i-1}$ *for* $i = 2, 3, 4$. *The variables have been normalized as* n/n_i, p/n_i *and* $n_T/(N_T/2)$.

current. The lower is the energy and the higher is the current, the finer should be the mesh especially in the impact zone. The correspondence can be roughly

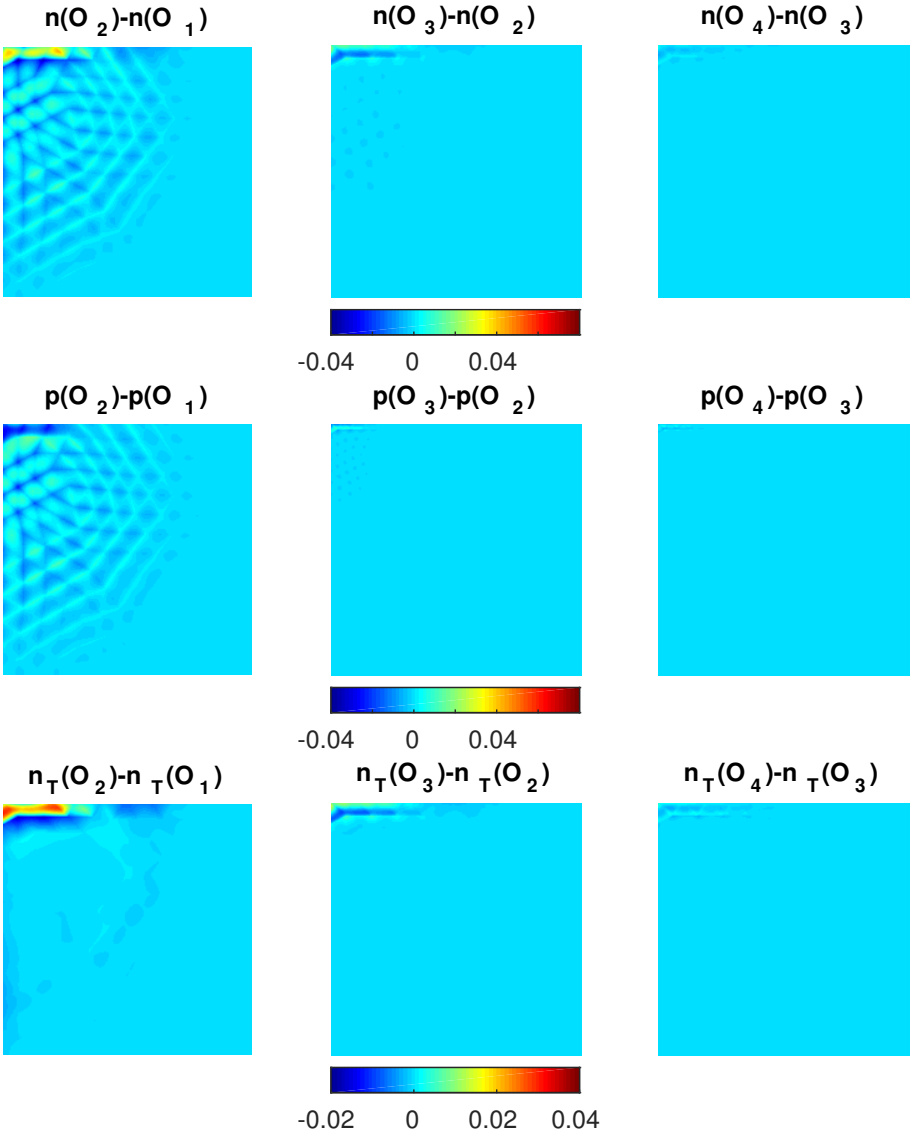

Figure 3.5: *The influence of the p-refinement on the solution for a sapphire sample with the e-beam of* 2 keV *and* 1 nA*. The element size is* $h \approx 10$ nm *and the order of basis functions is from* 1 *to* 4*. The variables have been normalized such that* n/n_i*,* p/n_i *and* $n_T/(N_T/2)$*.*

expressed as follows:

$$h \propto \frac{E_0}{j_0}, \tag{3.38}$$

where h is the average element size. Table 3.1 shows the required element

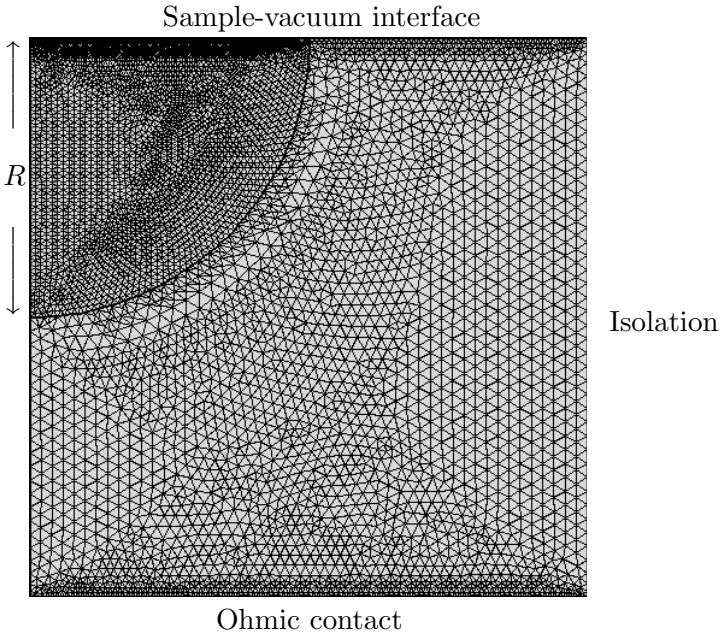

Figure 3.6: *The mesh pattern for the sample part.*

Table 3.1: *The average element size.*

E_0(keV)	0.5	2	5
h(nm)	0.5	2	5

size for the impact zone and under the sample-vacuum interface of a sapphire sample irradiated with different beam energies but the same current of 1 nA.

3.4 Stability

Since DDR equations are of convection-diffusion type one may expect various stability-related issues and should be prepared to introduce additional dissipation via artificial diffusion [50] or up-winding [51, 52].

Instability may emerge if convection dominates diffusion, i.e., in our case, if the drift current $\mu_n n \nabla V$ dominates the diffusion current $-D_n \nabla n$. Although at room temperature $\mu_n \approx 38.5 D_n$, one still needs reasonably high local values of both n and ∇V for the drift current to dominate and cause any significant trouble.

For a convection-diffusion transport equation, it has been proved that numerical instabilities occur when the element Péclet number is greater than

one. The element Péclet number for the equation (2.33) can be defined as

$$Pe = \frac{\mu_n \|\nabla V\| h}{2D_n}, \tag{3.39}$$

which is the ratio of convective to diffusive effect. Therefore, either large convective transport or small diffusive transport or both would cause numerical instabilities.

Probably the easiest (in terms of implementation) and cheapest approach that strengthens the stability of the FEM solver is to define the following artificial diffusion

$$D_{art} = \delta \mu_n \|\nabla V\| h, \quad 0 < \delta \leq 0.5, \tag{3.40}$$

and solve the equation (2.33) with the new diffusion constant of $D_n + D_{art}$. This approach with $\delta = 0.5$ guarantees the stability of the solver, regardless of the mesh quality. However, this approach is not the method of choice here, since it may lead to inconsistent solutions.

Our investigations show that we are not dealing with a highly convective problem, so it is possible to treat numerical instabilities simply with proper meshes. Figure 3.7 shows how the resolution of the mesh is determined for the simulation of a sapphire sample irradiated by a 2 keV 1 nA beam. The figure presents the local Péclet number at certain times of the simulation with different mesh resolutions. The first and second rows of Fig. 3.7 correspond to a uniform mesh with an average element size of 10 and 5 nm, respectively. As expected, the Péclet number decreased with decreasing the mesh size. Yet a uniform mesh with 5 nm resolution is not fine enough to keep the Péclet number below one everywhere. Therefore, the mentioned mesh refinement strategy has been used applying a finer mesh of $h = 1$ nm for the impact zone and under the sample-vacuum interface. The result, shown in the last row of Fig. 3.7, highlights the potential of the applied h-refinement strategy to maintain the Péclet number below unity.

To assess the effect of p-refinement on the Péclet number, simulation was performed with the second-order basis functions. The result, presented in Fig. 3.8, should be compared with those of the second row of Fig. 3.7 since the same mesh resolution has been used in both cases. The comparison indicates the inability of p-refinement approach to tackle the numerical instabilities in the present case.

3.5 Solvers

Unlike the steady state models, the discretization of time-dependent models doest not directly result in a system of algebraic equations and in fact the

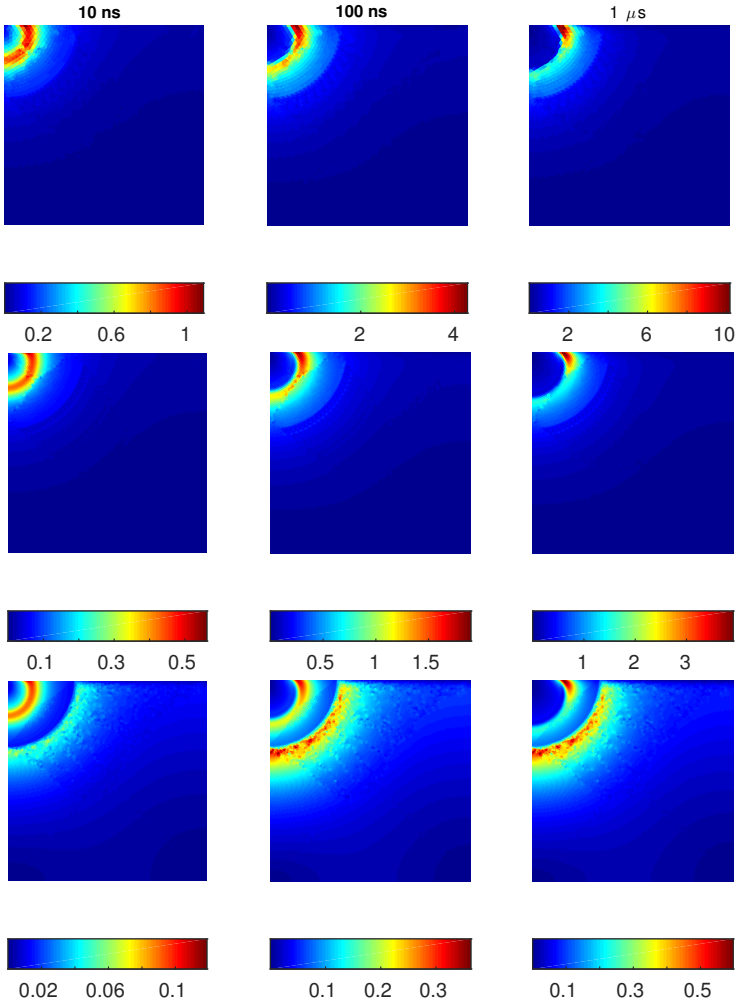

Figure 3.7: *The element Péclet number at certain times from the simulation of a sapphire sample irradiated by a 2 keV 1 nA beam using different mesh resolutions and the same basis functions of the first order.*

result would be a system of ordinary differential equations. In general, two types of methods, known as explicit and implicit methods, are used to solve this system of ordinary differential equations. The choice here is to use an implicit scheme since they are known to be unconditionally stable. The applied method is the generalized version of Backward Euler so called Backward Differentiation Formula (BDF). The BDF is a linear multi-step method for the numerical integration of ordinary differential equations. Indeed, by applying an implicit scheme, a system of ordinary differential equations is converted into a system of algebraic equations. The last strategy concerns the time-stepping

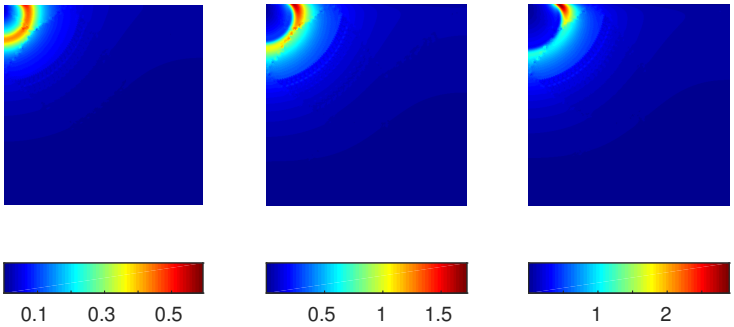

Figure 3.8: *The element Péclet number at certain times from the simulation of a sapphire sample irradiated by a 2 keV 1 nA beam using a uniform mesh of $h = 5$ nm and the second-order basis functions.*

Table 3.2: *Computational cost corresponding to the simulations of Figs. 3.7 and 3.8.*

Mesh	Basis function	Solver	Time (min:sec)	DOFs	Memory (GB)
uniform $h = 10$ nm	first order	fully coupled	00:24	14217	1.68
uniform $h = 5$ nm	first order	fully coupled	02:29	54358	2.02
uniform $h = 5$ nm	second order	fully coupled	16:36	215856	3.94
non-uniform $h = 5\&1$ nm	first order	fully coupled	11:28	184006	3.23
non-uniform $h = 5\&1$ nm	first order	segregated	02:38	184006	2.6

technique. For that, we apply automatic (adaptive) time-stepping technique in the presence of a smooth source model and a mixed of an automatic and strict time-stepping methods in the presence of pulsed source model. One faces a variety of challenges in obtaining the solution to the discretized FEM equations at each step of the BDF solver. The algebraic equations to be solved at each time instant are nonlinear and can be treated as either fully-coupled or segregated. As can be seen from the last two rows of Table 3.2 segregated equations are easier to solve, although the fully-coupled is generally more stable. First of all, the system of algebraic equations arising in the discretized model can be very large with degrees of freedom in the order of several millions. At each iteration of the Newton-Raphson scheme, a linear system should be solved. Since the linear systems in two dimensional case are not as large, the MUMPS (MUltifrontal Massively Parallel sparse direct Solver) solver is

Table 3.3: *Computational time corresponding to the 3D simulation in Section 5.2.*

Solver formulation	Solution time	Memory (GB)
Fully coupled	04:44:38	16.26
Segregated	11:05:24	5.38

applied, which is based on the LU decomposition.

Table 3.3 presents the computational cost of 3D simulations in Section 5.2 with respect to different solving strategies. This table shows that, unlike two-dimensional case, solving with the fully-coupled approach takes less computation time compared to the segregated approach, while the segregated scheme has shown to be cheaper in terms of needed memory in both two- and three-dimensional cases. Since the degrees-of-freedom was not as large, the linear systems were solved by the direct solver. Both methods provide very similar solutions.

4 Model calibration and validation

In this chapter the model is calibrated against published experimental data and validated by means of comparison with other models. In Section 4.1 the so-called standard yield of insulators is discussed and reproduced for a wide range of PE energies. Sensitivity of the model output with respect to material parameters is investigated and the values of parameters that are either unknown or uncertain are established by tuning. Sections 4.3 and 4.4 are devoted to the analysis of the continuous bombardment and defocused irradiation modes. In Section 4.4 we compare the charging dynamics predicted by our model with the predictions of a different one-dimensional model. Most of the material of this chapter has been published in [53].

4.1 Reproducing the standard yield of insulators

There are two main kinds of yield measurements from insulators: dedicated measurements with homogeneous pure samples [54, 55] and SEM scans of insulator-containing targets [56]. In the former case often great care is taken to avoid the charging effects. Typically, a defocused beam, a weak beam current, and a pulse of short duration are used. We define the SE yield free of charging effects as the *standard yield* and calibrate our code to reproduce such data as close as possible.

Parameters of standard-yield experiments [54, 55] (current, pulse duration, irradiation area) imply that the probability for the primary electrons to land anywhere close to each other on the surface is very small. In fact, with defocused beams and low, short-duration currents the expected distance between PE's is large enough to permit neglecting mutual interaction between any two impact zones. This is the main reason why standard-yield measurement are free of charging effects. The single-impact source function (2.56) with $i = 1$

allows to compute directly the expected number of emitted SE's per single (isolated) PE impact and is, therefore, applicable for modeling the standard yield. The cross-section of the axially-symmetric configuration used for calibrating the code is shown in Fig. 3.2. With sufficiently large computational domain the boundary conditions at the sides of the sample have no influence on the SE yield from a single PE impact and were set to homogeneous Neumann (zero current condition).

There are two classes of parameters that may be tuned within their physically admissible ranges: those that determine the shape of the source function approximating the initial pair generation and the short-time high-energy transport stage, and the material (bulk) parameters that determine the transport and trapping/de-trapping at much longer time scales. While these time scales may seem well-separated, in the DDR model, material parameters, especially the SRV v_n, have some influence on the initial transport stage as well.

The pair generation time t_{g}, defined as the time when all pairs have already been generated, determines the time width of the pulsed source functions $S_{n,p}(\mathbf{x}, t)$ and of the resulting SE emission current pulse. According to theoretical and experimental investigations by D.I. Vaisburd et al [57], between 10^{-17} and 10^{-14} s after impact the generated secondary pairs have already lost their ability to ionize the medium and their energy spectrum begins to evolve away from the spectrum of the primary beam as the result of collisions. However, up to 10^{-14} s most of the generated pairs still have energies above 20 eV. Since "true" SE's dominating the emission spectrum have energies below 20 eV, most of them must be emitted after 10^{-14} s. It has also been found that 10^{-11} s after impact all generated pairs are already thermalized with their energy spectra tightly localized around the edges of conduction and valence bands and trapping becomes more pronounced. Hence, the SE emission current pulse following a single PE impact should start after 10^{-17} s and be almost finished by 10^{-11} s. Moreover, if one aims at modeling "true" SE's, then the relative contribution to the total emission between 10^{-17} and 10^{-14} s should be small, compared to the contribution between 10^{-14} and 10^{-11} s. The DDR method produces exactly this type of pulses for t_{g} set between 10^{-16} and 10^{-14} s, see Fig. 4.1.

Notably, some parameters such as the SRV as well as the penetration depth influence only the magnitude, not the duration of the emission current pulse, see Fig. 4.2. In that figure R_{min} and R_{max} are the minimum and maximum values for the penetration depth estimated with published formulas and R_{tuned} is the tuned penetration depth by DDR model (explained below). As can be seen from Fig. 4.3, trap density and capture cross section influence not only the magnitude but also the duration of the emission pulse with the expected tendency for shorter pulses with the increase in the trapping rate.

We emphasize that the curves of Fig. 4.1 should be interpreted in the

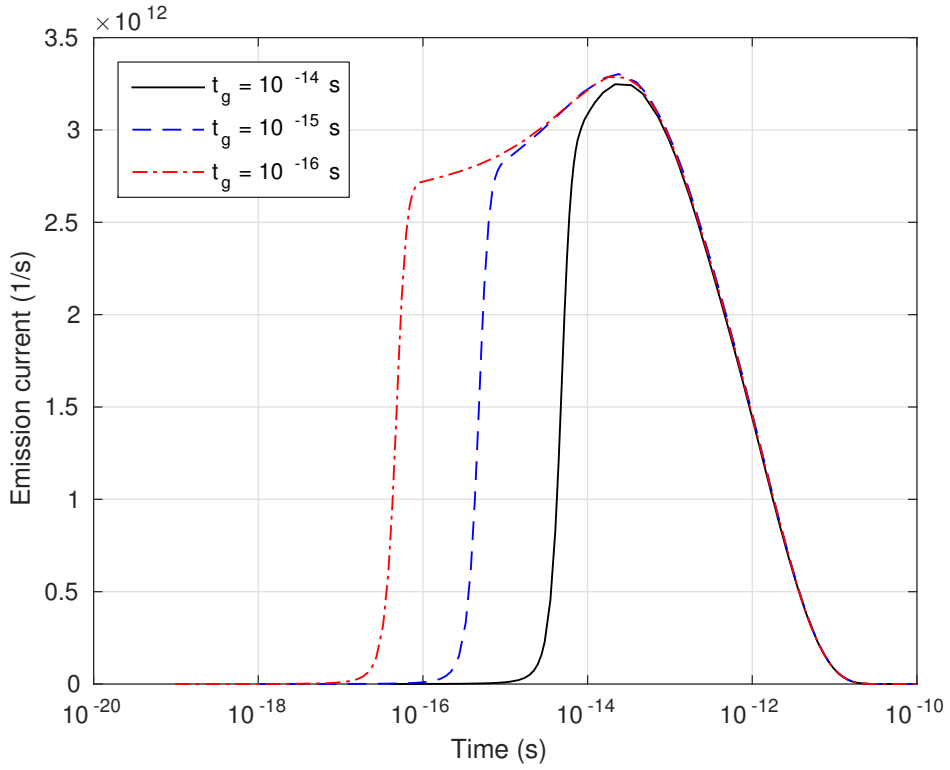

Figure 4.1: *Emission current pulse, calculated using the calibrated DDR model, from sapphire sample after the impact of a single* 500 *eV PE. Corresponding standard yields are:* 6.07 *($t_g = 10^{-14}$ s),* 6.17 *($t_g = 10^{-15}$ s), and* 6.14 *($t_g = 10^{-16}$ s).*

probabilistic sense. Namely, the integral of this curve between any two time instants $t_A \leq t_B$ is the number of particles expected to be emitted from the sample surface during the corresponding time interval. Thus, the expected yield at a given PE energy can be computed by numerically integrating the emission current between $t = 0$ and some sufficiently large $t > 10^{-11}$.

Among the material parameters the carrier mobilities $\mu_{n,p}$ have been determined with the highest precision and are simply assumed here to have the same values as in [35, 58, 59, 60]. Strictly speaking, these are the so-called low-energy mobilities and a more rigorous approach would be to use femtosecond and picosecond mobilities to model the transport of particles during the corresponding time intervals after the impact [57]. However, mainly due to the absence of data about these high-energy mobilities, here we use the same low-energy mobility values at all times. Nevertheless, the extremely short duration $[10^{-17}, 10^{-12}]$ s of the high-energy regime allows us to expect the

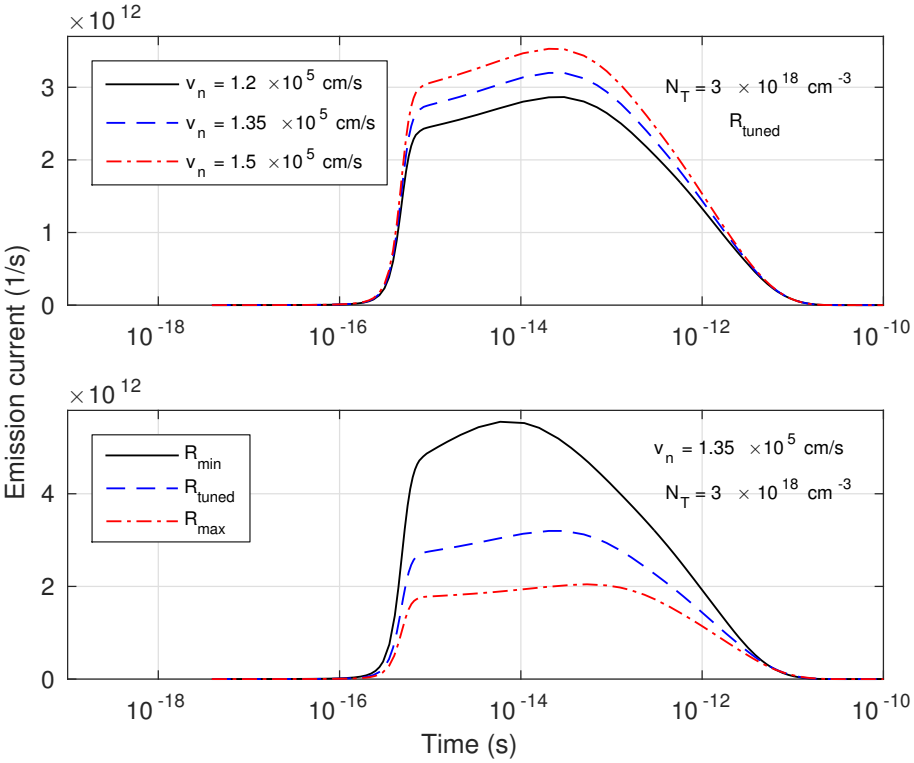

Figure 4.2: *Influence of SRV and penetration depth on the emission current pulse following the impact of a single* 500 *eV PE on a sapphire sample.*

approximations made in the DDR approach concerning the mobility values during this stage to be appropriate at least in the numerical sense. Notice that the changes in the yield do not exceed 0.2 when we vary the generation time t_g between 10^{-16} and 10^{-14} s in Fig. 4.1. Thus, to have any significant impact on the yield the mobility would have to vary dramatically during this interval of time.

Parameters $\sigma_{n,p}$ and N_T related to trapping weakly influence the magnitude of the emission current pulse and have, generally, large uncertainties. For example, in a study set out to investigate electron trapping in alumina [61] a relatively large variation of 10^{-21} to 10^{-15} cm^2 was reported for the electron capture cross section σ_n in polycrystalline alumina. The same study also revealed that polycrystalline metal oxide materials like sapphire (α-alumina) generally have trap site densities N_T in the order of 10^{18} cm^{-3}. Insulating solids are often grouped into three types: crystals, polycrystalline and amorphous [62]. The trap site density has been estimated to be around 10^{16} cm^{-3} for an alumina crystal, from 10^{17} to 10^{20} cm^{-3} for polycrystals, and around

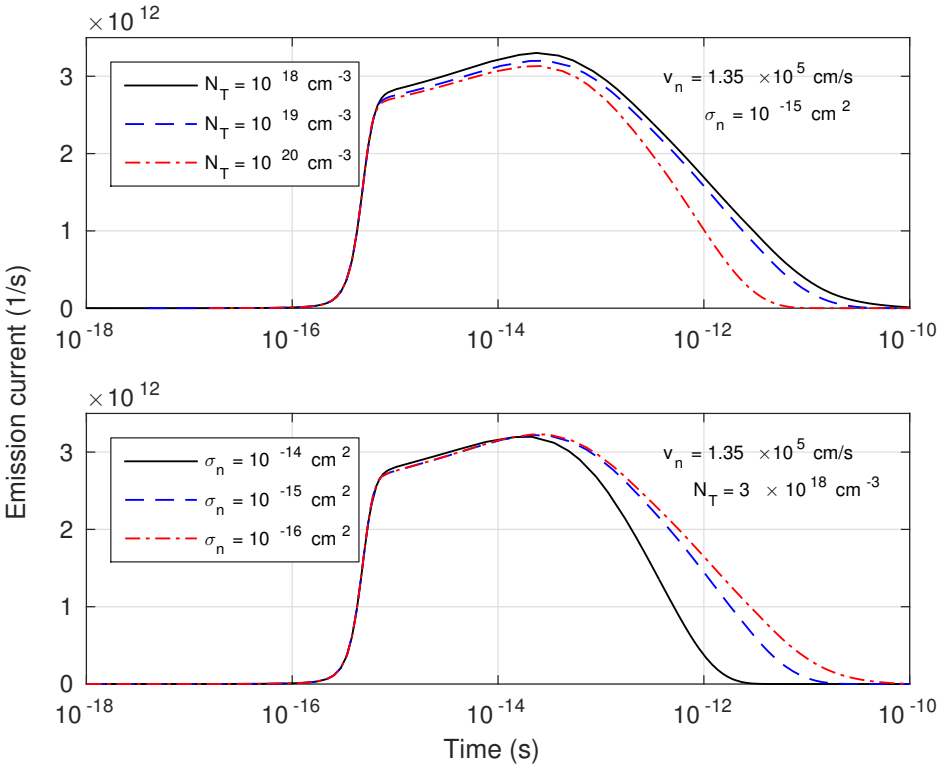

Figure 4.3: *Influence of the total trap density and electron capture cross-section on the emission current pulse following the impact of a single* 500 *eV PE on a sapphire sample.*

10^{21} cm^{-3} for an amorphous sample.

Probably one of the most comprehensive and systematic studies on charge transport and trapping in silica has been done by DiMaria and co-workers [63, 64, 65, 66], where a strong link has been identified between the capture cross sections and the nature of traps. The capture cross sections have been estimated to range from 10^{-18} to 10^{-13} cm^2. Confusingly, the values and ranges for these parameters are not limited to the above mentioned estimates [67, 68, 69].

Another parameter that strongly influences the magnitude of the emission current pulse is the maximum PE penetration depth R. It determines the spatial shape of the source functions $S_{n,p}(\mathbf{x}, t)$ and, therefore, the expected number of particles in the neighborhood of the sample-vacuum interface – the main contributors to the emission current. Many semi-empirical expressions have been proposed for R with the following general form

$$R(\rho, E_0) = CE_0^{\Gamma}, \tag{4.1}$$

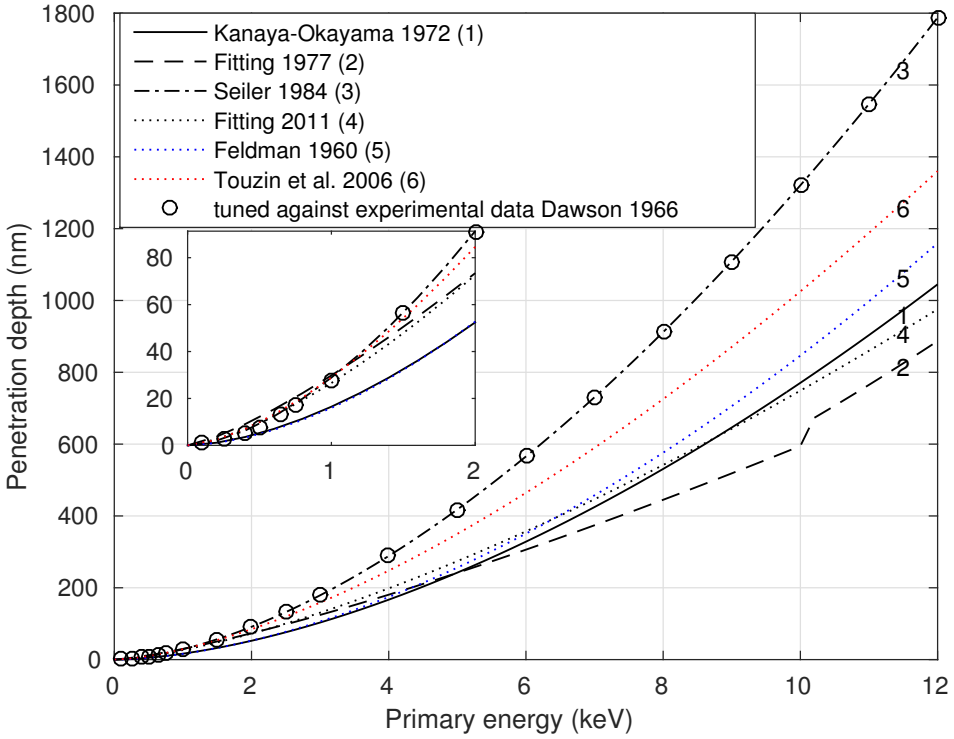

Figure 4.4: *The maximum penetration depth of PE's in sapphire as a function of PE energy.*

where the values for C and Γ vary from study to study [23, 26]. The constant C depends on the material and the exponent Γ has been mostly assumed to have a certain material-independent value, although, in some studies Γ has also been considered material-dependent [70].

The exponential expression for R emanates from Bethe's theory for the stopping power of charged particles in matter. Bethe's formula involves the density, atomic number, and atomic weight of the material. However, with the exception of studies by Kanaya and Okayama [71] and by Feldman [70], the density of the material is considered to be the only parameter influencing the electron penetration depth. As of now the estimation of R is far from being certain as can be seen from large discrepancies in the penetration depth estimates employed by different authors, see Fig. 4.4 and Fig. 4.6. Apparently, similar disagreement concerning the penetration depth exists for metals as well [72].

Having identified v_n, $\sigma_{n,p}$, N_T, and R as the most uncertain of the model parameters influencing the magnitude and duration of the emission current pulse we have performed a series of numerical experiments to determine the

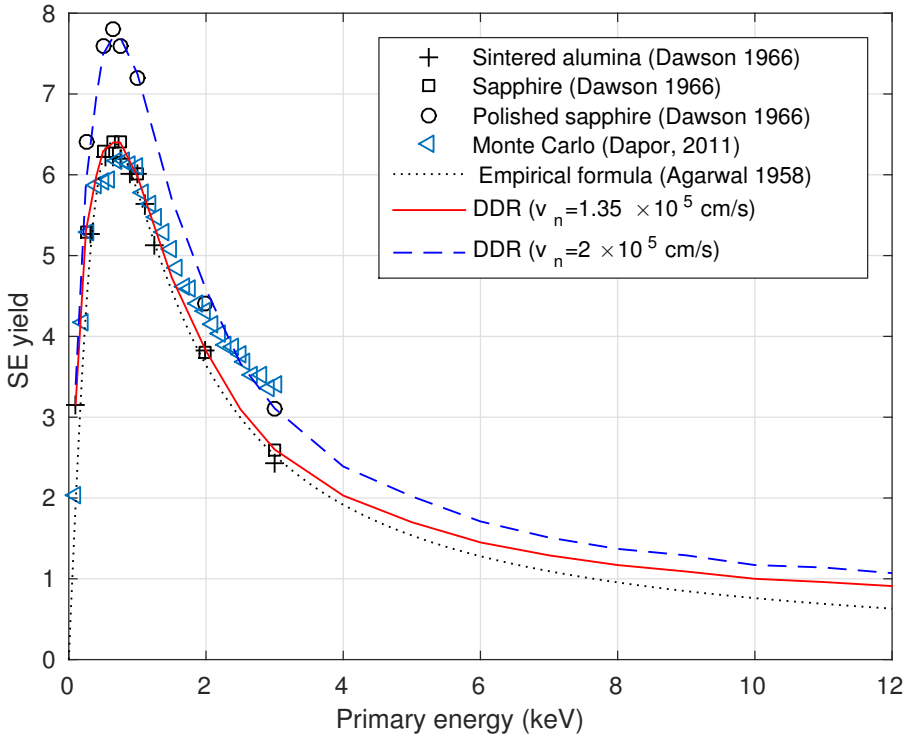

Figure 4.5: *The standard (uncharged) yield of sapphire as a function of PE energy.*

sensitivity of the DDR model output (SE yield) with respect to changes in these parameters. During these simulations some of the factors would be held fixed while other were varied with the goal to achieve the best possible fit between the computed SE yields and the experimental data.

Three key points emerged from this analysis:

- The shape of the yield-energy curve is influenced by the capture cross section and the density of traps. Namely, the larger the trap density and the capture cross section, the lower is the high-energy tail of the curve.
- The SRV affects the height not the shape of the yield-energy curve.
- Following any one of the published penetration depth formulas together with adjusting the values of material parameters within their permitted ranges does not produce yield-energy curves fully compatible with the experimental data over the whole range of PE energies.

In view of these facts and the aforementioned uncertainty about the energy dependence of the penetration depth, fine-tuning R for each PE energy

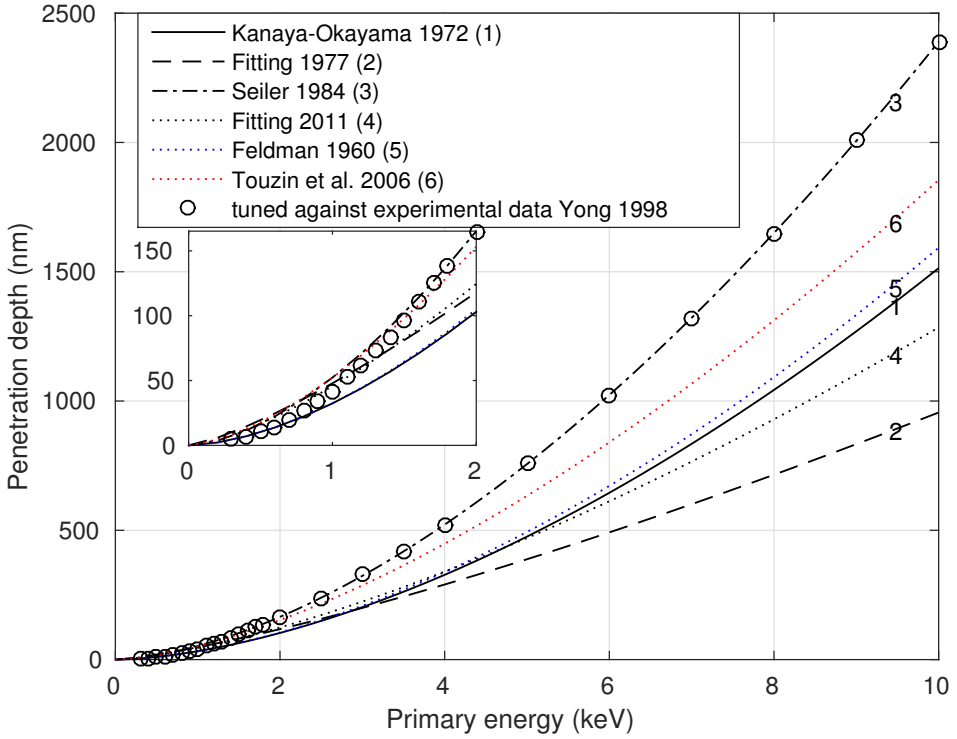

Figure 4.6: *The maximum penetration depth of PE's in silica as a function of PE energy.*

against the available experimental data was deemed by us as not only admissible, but also necessary. While tuning R other parameters have been fixed at the best found fitting values within their reported ranges. In particular, the electron and hole capture cross-sections were set at the frequently used values of 10^{-15} cm^2 and 10^{-17} cm^2, respectively. The trap site density turned out to be slightly higher than the reported upper bound 10^{19} cm^{-3}, namely, 3×10^{19} cm^{-3}, leading to the initial (equilibrium) density of trapped electrons of 1.5×10^{19} cm^{-3}, close to what was used by us previously [35].

For PE energies higher than 2 keV the tuned penetration depths for sapphire and silica presented in Fig. 4.4 and Fig. 4.6, perfectly match those of Lane and Zaffarano [73] and are well-described by the formula of Young [74]:

$$R(\rho, E_0) = 115 \frac{E_0^{1.66}}{\rho} \text{ [nm]}, \qquad E_0 \geq 2 \text{ keV}. \tag{4.2}$$

However, according to Young [74] the exponent of E_0 is 1.35, while the present results agree with the earlier reported [73] value of 1.66. There is some argument about this exponent in the literature. For instance, the study about

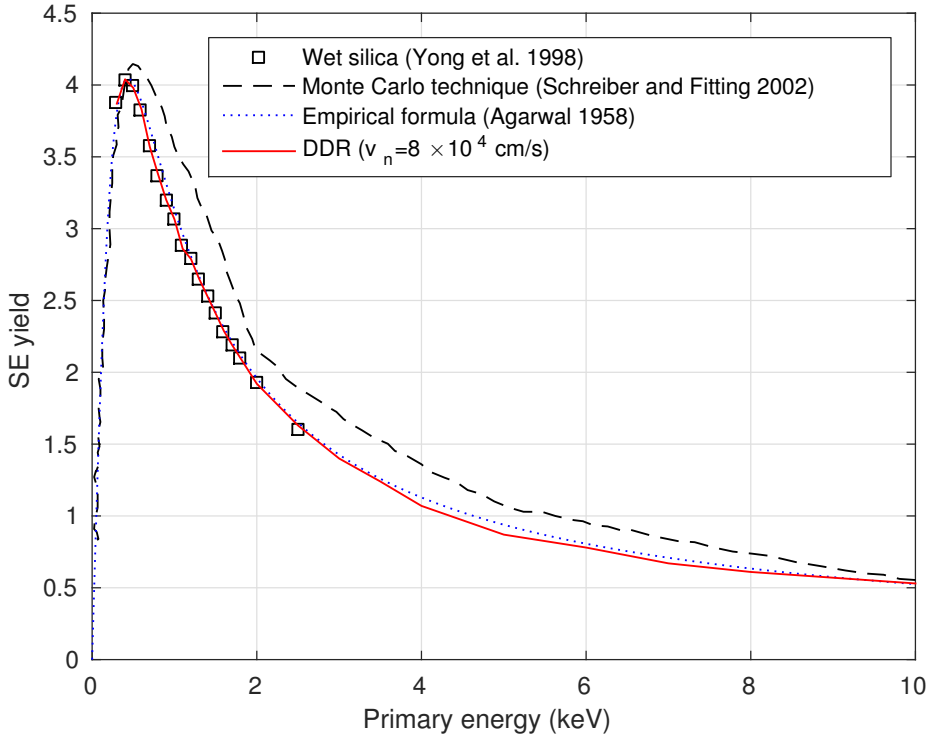

Figure 4.7: *The standard (uncharged) yield of silica as a function of PE energy.*

Kapton and Teflon [75] supports the idea of 1.66. Yet, the investigation of Salehi and Flinn [76] with $V_2O_5 - P_2O_5$ materials shows that, although at low energies the exponent is close to 1.35, neither 1.35 nor 1.66 provide good matches with higher-energy experimental data. The value of 1.66 was assumed for sapphire in several other investigations as well [77, 78].

As can be seen from the insets of Fig. 4.4 and Fig. 4.6 at energies below 2 keV the tuned penetration depths deviated from the formula (4.2) and did not follow any other published formulas, while remaining within their range. Least squares fitting of a separate exponential formula of the type (4.2) to the tuned penetration depths for alumina and silica did not provide a satisfactory fit. This suggests that below 2 keV the energy exponent Γ is indeed material dependent. Hence, for calibration purposes penetration depths below 2 keV must be determined by fitting to the corresponding standard yield data, whereas above this energy the depth may be safely deduced from the formula (4.2).

With the tuned penetration depths the DDR method provides practically exact yield-energy curves for the whole range of PE energies. As was mentioned previously, the height of the yield-energy curve is mainly controlled by

the surface recombination velocity at the sample-vacuum interface. In Fig. 4.5 we compare the output of the calibrated DDR model with the standard-yield data [54] (reported also in the database of Joy [79]), as well as Monte-Carlo simulations [80] and the empirical formula of Agarwal [81] for alumina samples. As far as the DDR model is concerned the only difference between the unpolished and polished alumina samples is the SRV at the sample-vacuum interface (1.35×10^5 cm/s and 2×10^5 cm/s, respectively), which sounds reasonable, since surface polishing should not affect the maximum penetration depth.

Comparison of the results by the calibrated DDR model with the experimental data [55], Monte-Carlo simulations [82], and the formula of Agarwal [81] for a silica sample is shown in Fig. 4.7. The tuned SRV at the silica-vacuum interface (0.8×10^5 cm/s) is lower than the SRV at the alumina-vacuum interface, indicating that v_n depends on both the material and the surface properties.

DDR simulations indicate that the first and the second unit yields for sapphire occur around 50 eV and 10 keV, respectively. For silica, the unit yields are observed below 50 eV and again at 4.35 keV. The values of the calibrated material parameters used in the present study are listed in Table 4.1.

A nearly linear dependence of SE yield on the SRV has been identified in our investigation. Based on this property, the following optimization procedure has been devised for tuning the value of SRV:

- Let Y_{exp} be the SE yield measured for PE's with energy E_0.
- Let $v_n^{(0)}$ be the initial guess for the SRV, and let $Y(v_n^{(0)})$ be the SE yield computed by the DDR solver with the SRV set to $v_n^{(0)}$.
- For $v_n^{(0)}$ sufficiently close to the true (optimal) value we can assume a linear relation:

$$Y_{\text{exp}} - Y(v_n^{(0)}) = \alpha(v_n - v_n^{(0)}). \tag{4.3}$$

  Since, obviously, $Y(0) = 0$, the coefficient α can be obtained as $\alpha = \frac{Y(v_n^{(0)})}{v_n^{(0)}}$, so that $v_n^{(1)} = v_n^{(0)} \frac{Y_{\text{exp}}}{Y(v_n^{(0)})}$.
- Compute $Y(v_n(1))$ with the DDR solver.
- If $Y(v_n^{(1)})$ is sufficiently close to Y_{exp}, then stop and set $v_n = v_n^{(1)}$. Otherwise, continue with $v_n^{(1)}$ as the new initial guess.

Table 4.1: *Parameters of dielectric materials.*

Parameter	SiO_2	Al_2O_3	Unit
ε	3.9 (ref.[83])	10 (ref.[14])	
μ_n	20 (ref.[60])	4 (ref.[58])	$cm^2V^{-1}s^{-1}$
μ_p	0.01 (ref.[60])	0.002*	$cm^2V^{-1}s^{-1}$
σ_n	10^{-15}	10^{-15}	cm^2
σ_p	10^{-15}	10^{-15}	cm^2
v_{th}	10^7 (ref. [84])	10^7	cms^{-1}
ρ	2.2 (ref. [85])	3.98 (ref. [85])	gcm^{-3}
E_g	9 (ref. [86])	9 (ref. [87])	eV
N_t	3×10^{19}	3×10^{19} sapphire 10^{20} amorphous	cm^{-3}
v_n	0.8×10^5	1.35×10^5 unpolished 2.0×10^5 polished 1.4×10^5 amorphous	cms^{-1}

*This value could not be found in literature and has been chosen by analogy with the relation between the electron and hole mobilities in SiO_2.

In principle, this process should be repeated with the SE yield data for a whole range of PE energies E_0. Unless changes in E_0 significantly alter the temperature of the sample, the SRV of a given material is supposed to be independent of E_0. Since the corresponding tuned values of v_n for the studied materials are all close to each other, so we have an additional confirmation that the DDR method is working properly.

4.2 Aftermath of a single impact

In this section we investigate the events following the injection of a single primary electron into a neutral dielectric sample. The goal of these numerical experiments is to estimate the space-time scales of the dynamics separately for all three particle species, i.e., n, p, and n_T as well as the total charge density $q(N_T/2 + p - n - n_T)$.

Figures 4.8 and 4.9 show the snapshots of the charge densities relative to their initial values in the two materials at 1 ps and 1 ns after impact. These images too should be interpreted in the probabilistic sense as the expected charge density. As can be seen, the smaller mass density of SiO_2 means, that with the same E_0 the maximum PE penetration depth R and the center of the initial charge distribution are deeper for SiO_2 than for Al_2O_3. The overall shapes of the initial charge distribution are different as well, see eq's. (2.51)

and (2.53), with the one of SiO_2 being broader. Hence the DDR dynamics starts with different initial states in these materials.

The generation of charge pairs by ionization is considered to take place in the period of 1 femtosecond after injection (t_g=1 fs). At t_g the density of free electrons reaches its maximum of 7.12×10^{18} and 1.89×10^{18} cm^{-3} in the center of impact region for Al_2O_3 and SiO_2, respectively. The density of free holes reaches its maximum at the same time of 1 fs. The maximum density of free holes in this stage for Al_2O_3 is 6.9×10^{18} cm^{-3} and for SiO_2 is 1.83×10^{18} cm^{-3}. Table 4.2 shows that the density of electrons decreases faster than that of holes since electrons are involved in three different processes; i.e. emission, trapping and recombination, while holes are only involved in the latter two. The density of holes remains constant for a short period of time (less than 0.1 ps). What is also apparent from the Figs. 4.8 and 4.9 is the difference in the spatial distributions of the electrons and holes at the end of the studied time period (1 ns). The maximum density for the electrons is in the center of impact zone but for the holes it is at the surface around the injection point. At 1 ns after impact, the densities of both free electrons and holes are already close to the intrinsic carrier concentration of the materials, (the last columns of Table 4.2).

The density of trapped electrons is initially equal to its equilibrium value and this equality remains for a period of 0.1 ps. Afterwards, detrapping process gradually starts from the center of impact zone as well as the sample surface. Simultaneously, a weak trapping occurs around the impact zone. As can be seen form Figs. 4.8 and 4.9 and also Table 4.2, the two processes proceed in their own regions leading to a significant detrapping of electrons mainly at and near the sample surface.

The interplay of the three charge species and the contribution of empty traps lead to the total charge density resembling an expanding spherical wave with initially an apple-shaped accumulation of negative charge at the end of pair generation time (the first columns of Figs. 4.10 and 4.11). This negative charge is seen as a disk on the surface of the sample. A plausible explanation for the presence of only negative charge at very early stages after the injection would be that during this very short period of time, charges are not mobile enough to escape from the impact region. Indeed, the generated electrons and holes are spatially close enough to compensate each other while they are not yet recombined. Therefore it could be concluded that this negative charge originates from only one extra primary electron in the sample. Another evidence that supports this scenario is that the depth of the occupied zone by negative charge is the same as the maximum penetration depth of the primary electron and so there are no charges outside the impact zone.

Afterwards, the pattern is transformed into a different structure, arriving at a positive charge region in the middle surrounded by a shell of negative

Table 4.2: *The maximum and minimum amounts of the free electron density n, the free hole density p and the trapped electron density n_T (cm^{-3}) in sapphire and silica at certain times after the impact of a single primary electron with the energy $E_0 = 1$ keV.*

Material	Charge density (cm^{-3})	1 fs		1 ps		1 ns	
		min	max	min	max	min	max
Al_2O_3	n	1×10^{10}	7.12×10^{18}	1×10^{10}	5.13×10^{18}	8.18×10^{9}	8.69×10^{10}
	p	1×10^{10}	6.9×10^{18}	1×10^{10}	5.95×10^{18}	9.9×10^{9}	1.40×10^{10}
	n_T	1.5×10^{19}	1.5×10^{19}	1.4913×10^{19}	1.5012×10^{19}	1.2917×10^{19}	1.5017×10^{19}
SiO_2	n	1×10^{10}	1.885×10^{18}	1×10^{10}	1.439×10^{18}	7.48×10^{9}	1.91×10^{11}
	p	1×10^{10}	1.829×10^{18}	1×10^{10}	1.578×10^{18}	9.98×10^{9}	1.17×10^{10}
	n_T	1.5×10^{19}	1.5×10^{19}	1.498×10^{19}	1.5007×10^{19}	1.4515×10^{19}	1.502×10^{19}

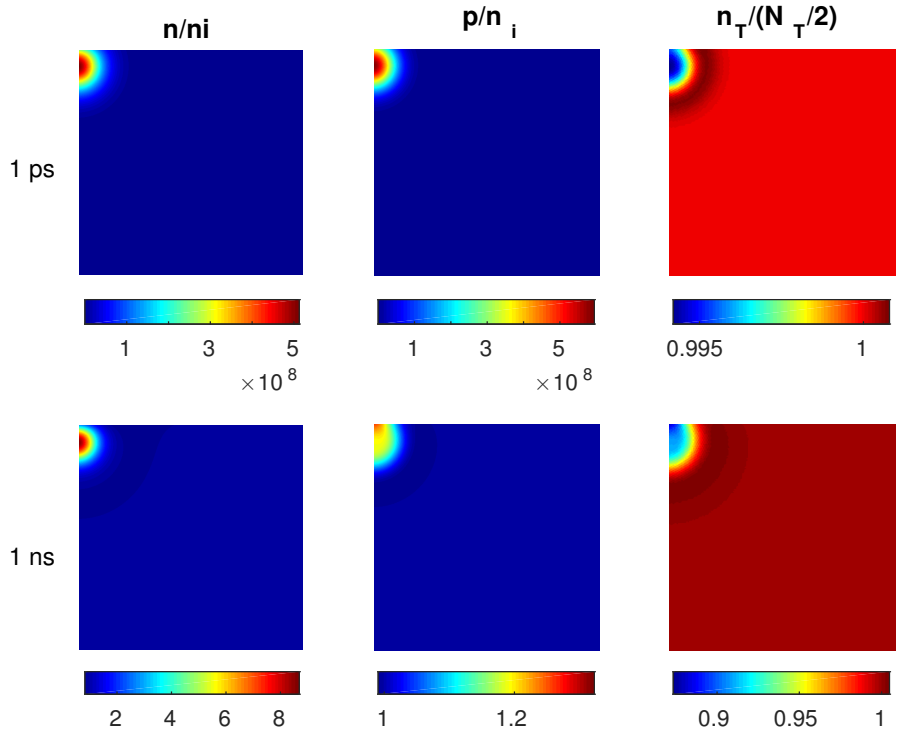

Figure 4.8: *The density of free electrons, free holes and trapped electrons (cm^{-3}) in sapphire (Al_2O_3) at certain times after the impact of a single primary electron with the energy $E_0 = 1$ keV. Vertical cross-section, side length is* 100 *nm.*

charge, see the second and third columns of Figs. 4.10 and 4.11. Due to the emission of electrons the initial predominantly negative charge at the sample-vacuum interface is gradually replaced by a disk of positive charge in the middle and at the injection point surrounded by a ring of the negative charge. Since the electrons are much faster than the holes, they can readily escape form the impact zone, leading to the result shown in the second columns of Figs. 4.10 and 4.11. The observed space-charge behavior is in a close agreement (only in terms of charge pattern) with the earlier studies of Renoud et al [60, 88].

In Al_2O_3, the positive charge reaches its maximum of 0.33 C/cm^3 at the surface at $t = 1$ ns and the negative charge has the maximum of (in the sense of absolute value) -0.033 C/cm^3 at $t = 1$ fs and is situated in the center of impact zone. In SiO_2, the positive charge increases its maximum of 0.08 C/cm^3 at the surface at time $t = 1$ ns and the negative charge has the maximum of -0.009 C/cm^3 in the center of impact zone at $t = 1$ fs. As can be seen from

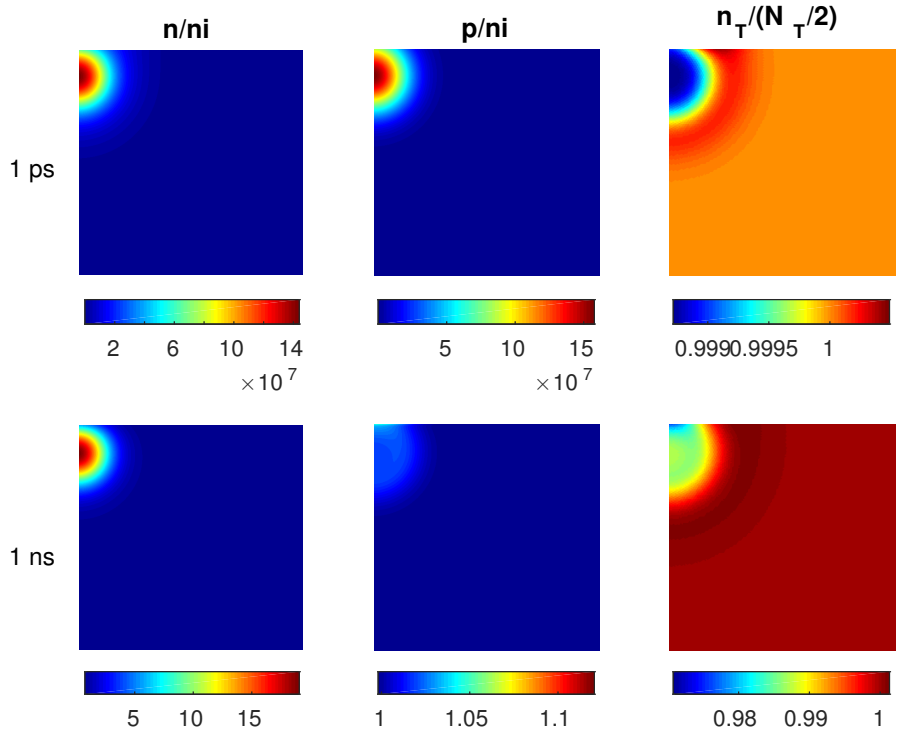

Figure 4.9: *The density of free electrons, free holes and trapped electrons (cm^{-3}) in silica (SiO_2) after the impact of a single primary electron with the energy $E_0 = 1$ keV. Vertical cross-section, side length is* 100 *nm;*

Table 4.3, total charge up to 1 ps is predominantly supplied by free charges. Thereafter the situation gradually changes by involving the free charges in generation/recombination (trapping/detrapping) process, resulting in a total charge that comes mainly from the trapped charges at time 1 ns, (see the last column of Table 4.3).

Obviously, the electric potential closely follows the distribution of the total charge. Initially we observe a negative potential in the middle of the impact zone. For example, in Al_2O_3 at the beginning a negative potential with the maximum of -0.07 V is observed in the impact zone at t_g. After less than 1 ps, a transition occurs which results in the positive potential in the middle.The maximal value achieved by the positive potential is 0.41 V at in the center of impact zone at 1 ns.

Table 4.3: *The maximum and minimum amounts of free charge* $(p-n)q$*, trapped charge* $(N_T/2-n_T)q$ *and total charge* $(N_T/2+p-n-n_T)q$ $(C\,cm^{-3})$ *in sapphire and silica at certain times after the impact of a single primary electron with the energy* $E_0 = 1$ *keV.*

Material	Charge (Ccm^{-3})	1 fs		1 ps		1 ns	
		min	max	min	max	min	max
Al_2O_3	$(p-n)q$	-0.033	0.0	-0.0153	0.166	-1×10^{-8}	3×10^{-10}
	$(N_T/2-n_T)q$	-2.6×10^{-6}	0.0	-0.002	0.014	-0.0114	0.33
	$(N_T/2+p-n-n_T)q$	-0.033	0.0	-0.017	0.178	-0.014	0.33
SiO_2	$(p-n)q$	-0.009	0.0	-0.007	0.04	-3×10^{-8}	4×10^{-10}
	$(N_T/2-n_T)q$	-7×10^{-7}	0.0	-0.001	0.003	-0.0031	0.078
	$(N_T/2+p-n-n_T)q$	-0.009	0.0	-0.008	0.042	-0.0031	0.078

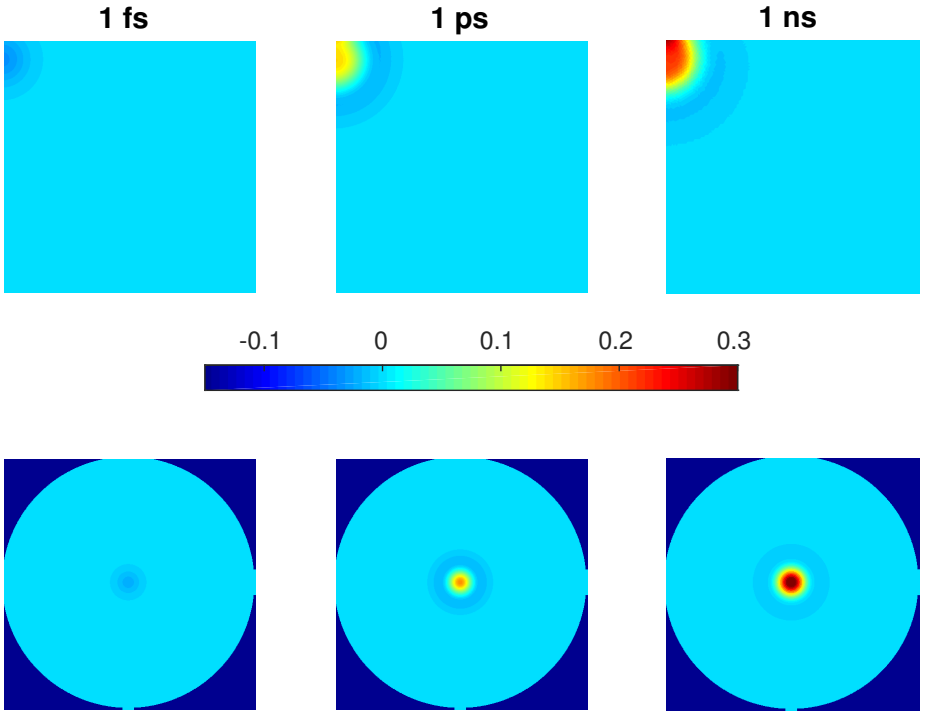

Figure 4.10: *Evolution of the total charge* $(N_T/2 + p - n - n_T)q$ $(C\,cm^{-3})$ *in sapphire* (Al_2O_3) *after the impact of a single primary electron with the energy* $E_0 = 1$ *keV. Top row: vertical cross-section, side length is* 100 *nm; bottom row: top-view of the sample-vacuum interface, diameter is* 200 *nm.*

4.3 Pulsed source versus smooth source

The electron gun of a typical SEM is able to produce PE currents in the range of pico to nano Ampéres (i.e. average interval between PE impacts from nano to picoseconds). The charge dynamics following the impact of a single PE, analyzed in the previous section, clearly shows that the next electron faces variable conditions in the sample depending on the time of its arrival.

Since the main features of the charge dynamics in SiO_2 and Al_2O_3 are essentially similar, we restrict our discussion to the latter material. In this section an Al_2O_3 sample is considered under focused beams with the current of 10 nA (average time between PE impacts is 16 ps) and the primary energy of 5 keV. In the case of bombardment, we opt for energies above 2 keV, so that the penetration depth estimation follows formula (4.2).

We have performed a simulation with 100 PE impacts and compared the idealistic source with periodic impacts, see eq. (2.56), with the time-uniform source model, see eq. (2.57). In fact, in the more realistic source, PE's impact

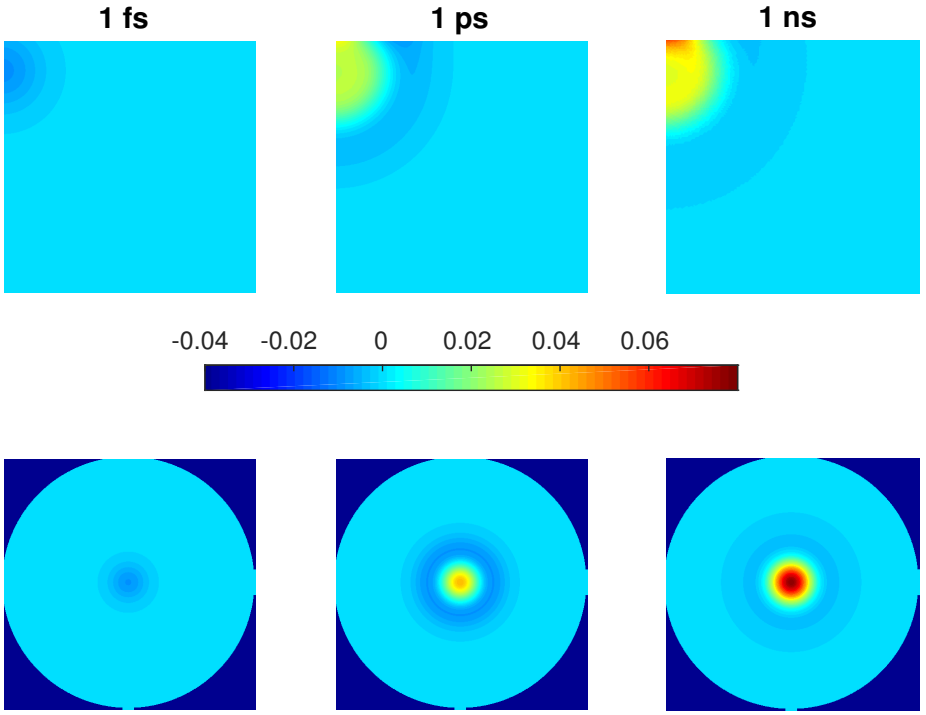

Figure 4.11: *Evolution of the total charge* $(N_T/2 + p - n - n_T)q$ $(C\,cm^{-3})$ *in silica* (SiO_2) *after the impact of a single primary electron with the energy* $E_0 = 1$ *keV. Top row: vertical cross-section, side length is* 100 *nm; bottom row: top-view of the sample-vacuum interface, diameter is* 200 *nm.*

the sample at time instants drawn from the Poisson distribution. The source models considering regular and Poisson assumption impacts can be formulated as follows:

$$S_{n,p}(\mathbf{x},t) = \sum_i \frac{g_{n,p}(\mathbf{x}, E_{\text{lan}})}{L\left(i\left(\frac{q}{j_0}\right) + t_{\text{g}}\right) - L\left(i\left(\frac{q}{j_0}\right)\right)} \frac{dL}{dt}\left(t - i\left(\frac{q}{j_0}\right)\right). \tag{4.4}$$

Whereas impacts following the Poisson distribution can be modelled as:

$$\begin{aligned} S_{n,p}(\mathbf{x},t) &= \sum_i \frac{g_{n,p}(\mathbf{x}, E_{\text{lan}})}{L\left(r_i\left(\frac{q}{j_0}\right) + t_{\text{g}}\right) - L\left(r_i\left(\frac{q}{j_0}\right)\right)} \frac{dL}{dt}\left(t - r_i\left(\frac{q}{j_0}\right)\right), \\ r_0 &= -\ln(1-r)\left(\frac{q}{j_0}\right), \\ r_i &= r_{i-1} - \ln(1-r)\left(\frac{q}{j_0}\right), \text{ for } i > 0, \end{aligned} \tag{4.5}$$

where j_0 is the beam current and r is a random number in the interval $(0, 1)$.

From the mathematical point of view no steady-state solution exists with the pulsed source model (where each PE impact is modelled individually). At most, one can expect a time-periodic solution if PE impacts happen at regular intervals. The continuous source may, on the other hand, result in a solution that converges to a steady state for $t \to \infty$.

Figure 4.12 shows the variation of total (including reverse electrons) and SE yields with time obtained by the regular pulsed model (4.4). The result indicates a sharp increase in the yield at the time of impact. It is also observed that in the presence of charging, the yield peaks move downwards while charging does not significantly affect the pulse duration. From the computational point of view and based on our investigation, performing simulation with regular pulsed model using automatic time-stepping method would result in missing some of the pulsed sources. So, one possibility is to apply strict time-stepping method resulting in a time-consuming and costly simulation. Here, in order to have a reasonable computational time and catch the pulsed sources, we have applied a combination of both strict and automatic time-stepping methods with strict time-stepping active only for a short period after impacts and automatic time-stepping during the relaxation periods between impacts. The same strategy can not be followed with the Poisson model of (4.5) since the impact times are random.

Figure 4.13 shows the variation of the total (including reverse current) and SE yields with time by the time-average (2.55) and continuous (2.57) models. The time-average yields have been calculated based on the results of pulsed model. The irregular behavior of the yield curve by time-average model led us to perform simulation with finer time steps and 50 pulsed impacts. As can be seen from Fig. 4.13, the finer time-stepping delivers a smoother yield curve by the time-average scheme as well as a result closer to the yields of continuous source model. Apparently the time-average source model tends to underestimate the instantaneous SE yield by almost 10%. One can correct for this by increasing the effective beam current value. Otherwise, the time-average model is much easier to handle numerically.

4.4 Continuous irradiation with defocused beams

Sustained bombardment, even with defocused beams, increases the probability for an incoming PE to fall in close proximity to a previous impact zone. This will introduce the interaction between the previously trapped charges and the newly generated pairs, so that the yield will vary with time. At the moment a standard experimental procedure for measuring yield variation during sustained bombardment does not exist. Therefore, here we compare predictions

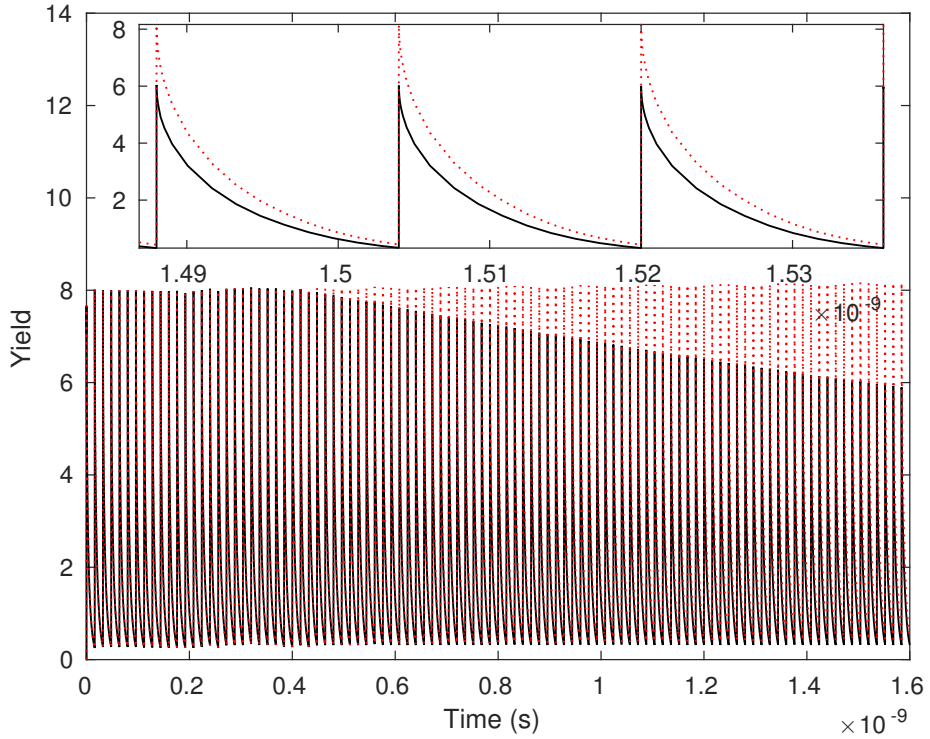

Figure 4.12: *The variation of total and SE yields against time by the regular impacts of* 100 *electrons with the energy and current of* 5 *keV and* 10 *nA, respectively. The solid line shows SE yield and the dotted line shows total yield including reverse current.*

of the DDR model with the earlier one-dimensional simulations by the Flight-Drift (FD) model – a self-consistent approach by Touzin et al[15]. FD model is a current-density based formalism incorporating a detailed recombination and trapping mechanism. For comparison purposes we have considered the same material (amorphous alumina), current density, and the penetration depth formula (energy exponent in (4.2) is set as $\Gamma = 1.55$). We switch now to the continuous (time-integrated) source function (2.57), (2.58)–(2.61) suitable for long-time modeling.

Since the sample is amorphous alumina rather than sapphire, we choose a higher trap density of 10^{20} cm^{-3} pertaining to the so-called shallow traps[15]. We set the SRV to 1.4×10^5 cm/s, close to what we have obtained above for unpolished sapphire. We note that in time-domain investigations the quantity of interest is not the charge yield, but the instantaneous ratio of the net SE emission current to the incident beam current – SE emission rate.

Taking into account that our approach is fundamentally three- not one-

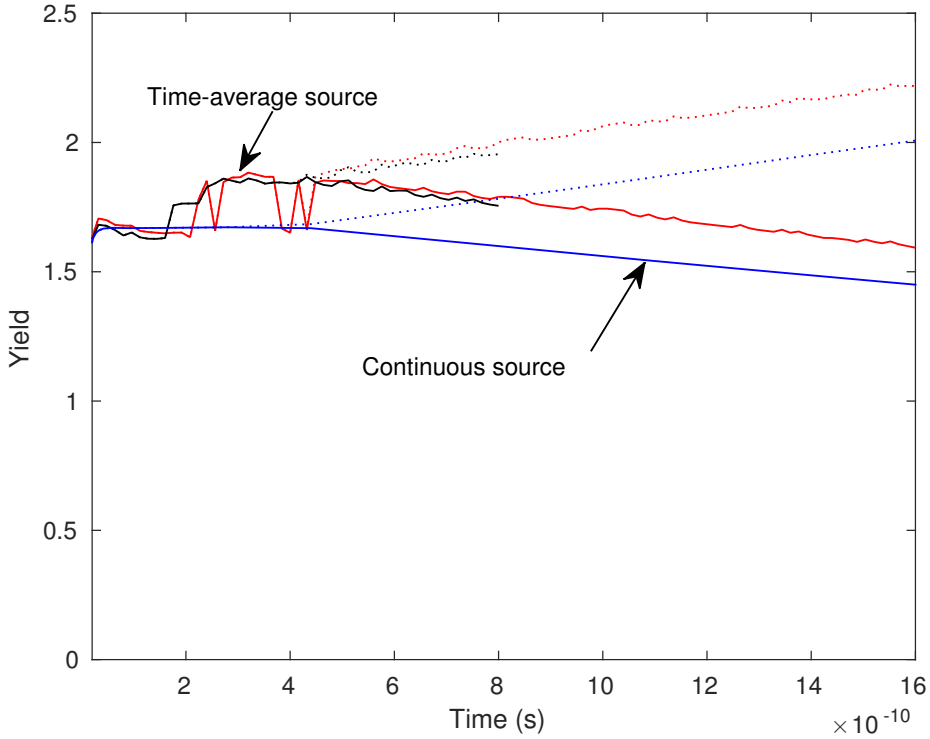

Figure 4.13: *The variation of total and SE yields against time by the the time-average and continuous models with the energy and current of* 5 *keV and* 10 *nA, respectively. The solid line shows SE yield and the dotted line shows total yield including reverse current.*

dimensional, the results presented in Figs. 4.14 and 4.15 show general agreement with the Figures 10 and 11 by Touzin et.al [15], especially for the surface potentials at low PE's and the corresponding SE emission rates. However, at higher PE energies the accumulated negative potential is smaller (lower bounds: -0.9 kV in 3D-DDR against -2.5 kV in 1D-FD) and the yield collapses to unity faster (upper bounds: ~ 1 ms in 3D-DDR against ~ 10 ms in 1D-FD).

It appears that the distance to the closest Dirichlet boundary, where the electric potential is maintained at some fixed value, e.g., zero, strongly affects the value of the surface potential at the sample-vacuum interface. Apparently, the most important parameter controlling the magnitude of the potential is not the total charge density, as one would naively assume, but the proximity to an ohmic contact. Most likely this is due to the image-charge effect, which partially screens the charge accumulated in the sample.

Numerically, the screening effect of the Dirichlet condition can be min-

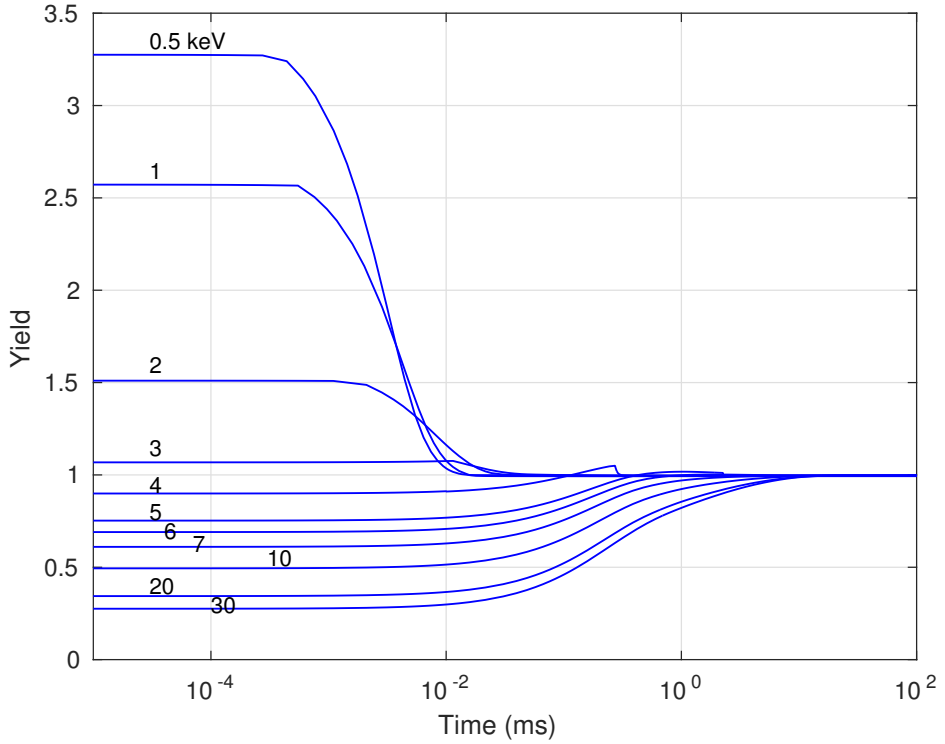

Figure 4.14: *Time evolution of the yield from an amorphous alumina sample versus PE energy for a defocused beam with current density of* 10^{-5} A/cm^2. *The distance between* Σ_1 *and* Σ_2 *is* 1 *mm.*

imized by placing the ohmic contact Σ_1 as far as computationally possible from the sample surface Σ_2. Thus, we have placed Σ_1 at various distances from Σ_2 and, as can be seen in Fig. 4.16, the surface potential does reach significant negative values when the Dirichlet boundary is far enough. However, the time of collapse of yield to unity becomes even shorter in these numerical experiments and remains at odds with the previous one-dimensional FD simulations.

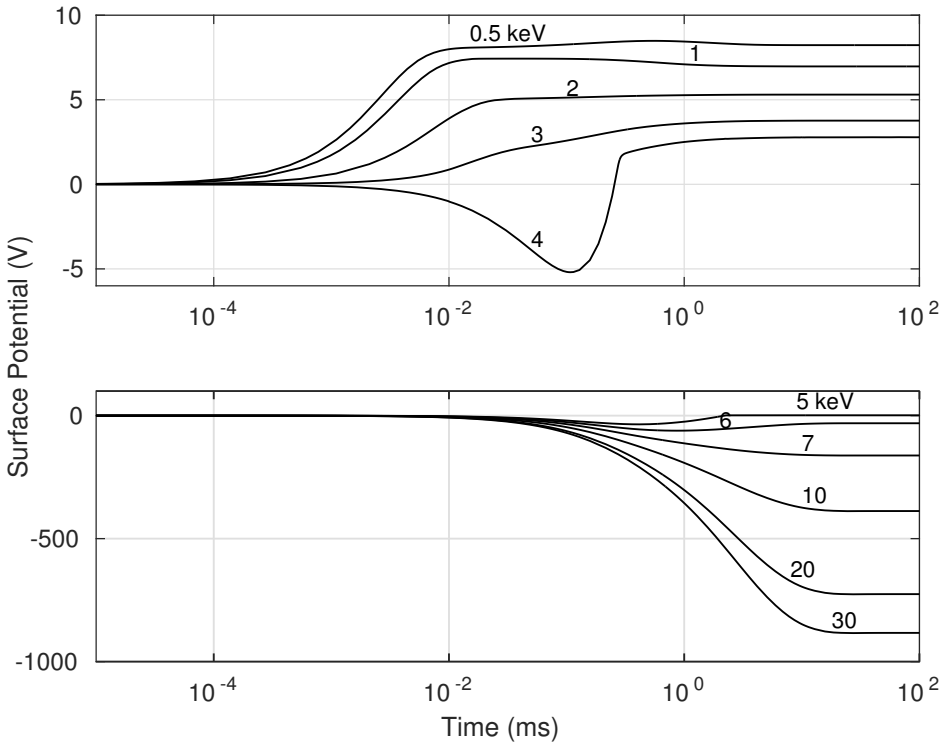

Figure 4.15: *Time evolution of the electric potential at the surface of an amorphous alumina sample versus PE energy for a defocused beam with current density of* 10^{-5} *A/cm*^{2}*. The distance between* Σ_1 *and* Σ_2 *is* 1 *mm.*

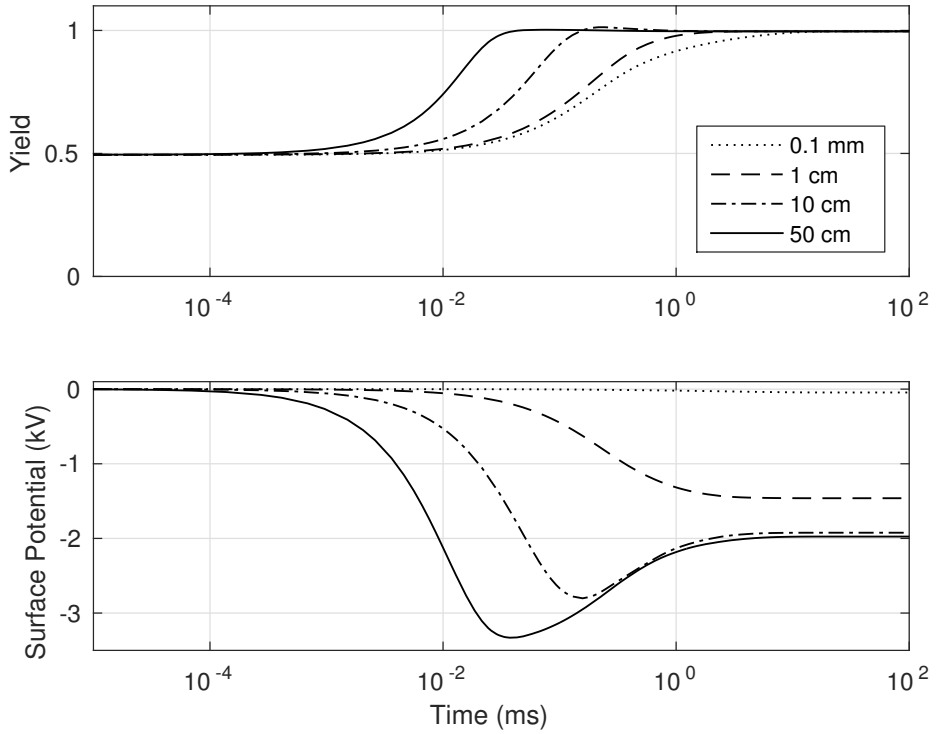

Figure 4.16: *Time evolution of the yield and the surface potential from an amorphous alumina sample at* 10 *keV PE energy versus the proximity to the ground contact for a for a defocused beam with current density of* 10^{-5} A/cm^2.

5 Applications

The aim in this chapter is to study the charging effect in insulators subjected to electron bombardment by focused stationary and moving electron beams. Utilizing the information from Chapter 4, in Section 5.1 we present the results of numerical experiments concerning the SE yield and surface potential variations in e-beam irradiated insulators. Section 5.2 presents further quantitative analysis of a more realistic scenario with a moving beam, including a dynamic line-scan of a laterally inhomogeneous target. The final section of this chapter deals with the simulation of electron emission from a thin membrane pertaining to a transmission electron multiplier called Tynode.

5.1 Focused beam

In the first series of numerical experiments we use the axially symmetric target of Fig. 3.2 illuminated in the middle by a focused stationary beam. The distance between Σ_1 and Σ_2 is set to 0.1 mm. The samples studied in Fig's 5.1–5.4 are isolated in the sense that the only boundary penetrable for particles in the sample-vacuum interface Σ_2. We consider the worst case scenario – perfect focusing – where all PE's hit the same spot on the sample surface. It is easy to deduce that defocusing will affect low-energy PE's with their small impact zones much stronger than higher energy PE's with their extended impact zones. To anticipate the results for more realistic partially focused beams the reader is advised to compare plots of this Section 5.1 with those presented in Section 4.4.

Figure 5.1 pertains to an unpolished sapphire sample irradiated at 5 keV, where the standard yield is around 1.7 as can be deduced from Fig. 4.5. The net SE emission rate – yield for short – starts at the standard yield value, but after a certain interval of time drops to unity for all beam currents. The

stronger the current, the shorter is the standard yield interval preceding the drop. In fact, it is easy to calculate that the drop in the yield happens after a certain amount of charge has been injected into the sample by the beam, which confirms conclusions of many previous investigations. The point of fastest decline in the yield roughly corresponds to 3×10^{-18} C of injected primary charge, i.e., approximately 19 primary electrons.

While the magnitude of the surface potential in the steady sate regime has shown to be independent of the beam current in the presence of positive potential (Fig. 5.1), the result presented in Figure 5.2 shows that the same cannot be claimed for the higher PE of 30 keV with negative potential. In fact, the result introduces the beam current as an influential factor in controlling the magnitude of the surface potential in the steady state.

The DDR model does not substantiate the usual intuitive explanation [60, 15] concerning the reasons behind this seemingly inevitable convergence of yield to unity with time. Commonly it is argued that the charging of the sample leads to the change in the landing energy of PE's, so that the yield no longer corresponds to the standard yield of that energy, but rather to another point on the standard yield curve of Fig. 4.5. If, for example, the standard yield is greater than one, then the sample accumulates positive charge. The landing energy increases and one should look to the right along the standard-yield curve to know what the new yield should be. If, on the other hand, the standard yield is less than one, then the accumulated negative charge reduces the landing energy of the PE's, thus, moving to the left along the standard-yield curve. Thus, it is argued, a yield larger than one would eventually lead to a positive potential high enough to shift the landing energy of primary electrons to the second unity-crossing point on the standard yield curve. This argument, while intuitively appealing, does not take into account the spatial distribution, the dynamics, and the screening of charges. In fact, in our simulations the accumulated potential was never strong enough for the landing energy to reach a unity-crossing point.

The unity-crossing argument for small PE energies and larger than one standard yields has been previously criticized in [89, 90], where the significant role of the reverse current in the yield drop was pointed out. We also believe that the PE landing energy change alone cannot explain the yield collapse, since in all our simulations the accumulated potential was never strong enough for the landing energy to reach a unity-crossing point.

For example, Figure 5.1 (bottom) clearly shows that the value of the positive surface potential is insignificant with respect to the PE energy and cannot possibly change the landing energy by so much that it becomes 10 keV – the second point along the standard-yield curve where it crosses the unity line. What the DDR model shows, though, is that the drop in the yield coincides with the rapid increase in the reverse current, caused by the relatively weak

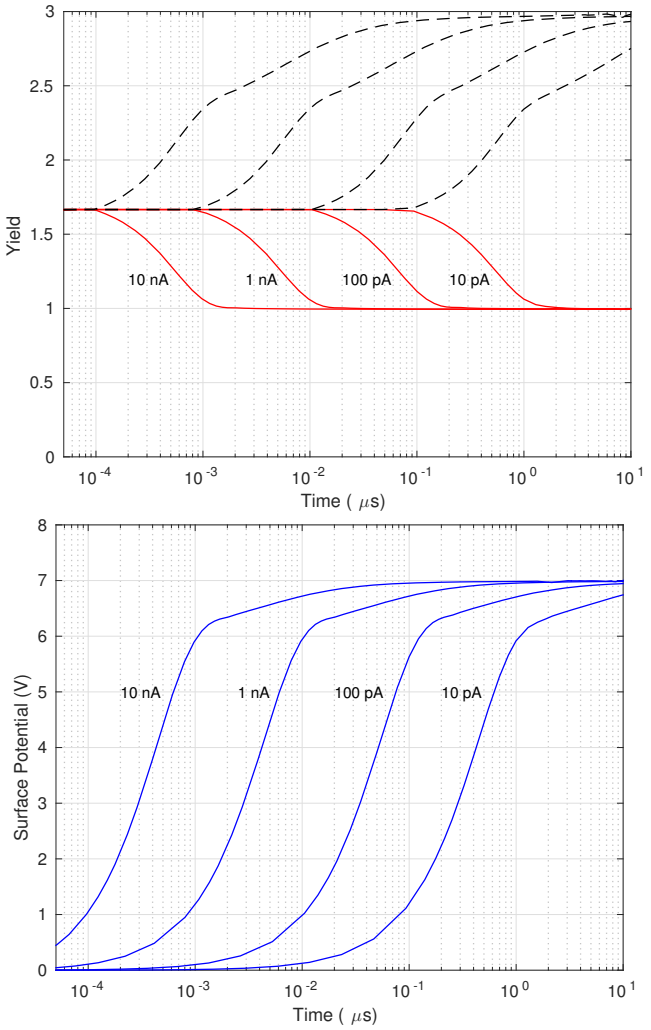

Figure 5.1: *Time evolution of the yield (top) and the surface potential at the beam entry point (bottom) for a sapphire sample continuously irradiated by a focused stationary beam at 5 keV PE energy – effect of beam current. Top: dashed line – positive part of the SE emission rate through the sample-vacuum interface, solid line – net SE emission rate, including the negative reverse-electron current.*

positive surface potential attracting low-energy SE's back to the sample. Figure 5.1 (top) compares the contribution of the positive part $v_n(n - n_i)$ of the emission current density (dashed lines) to the net SE emission rate (solid lines). The onset of the reverse current can be deduced from the emergent discrepancy between the solid and dashed curves, which coincides with the

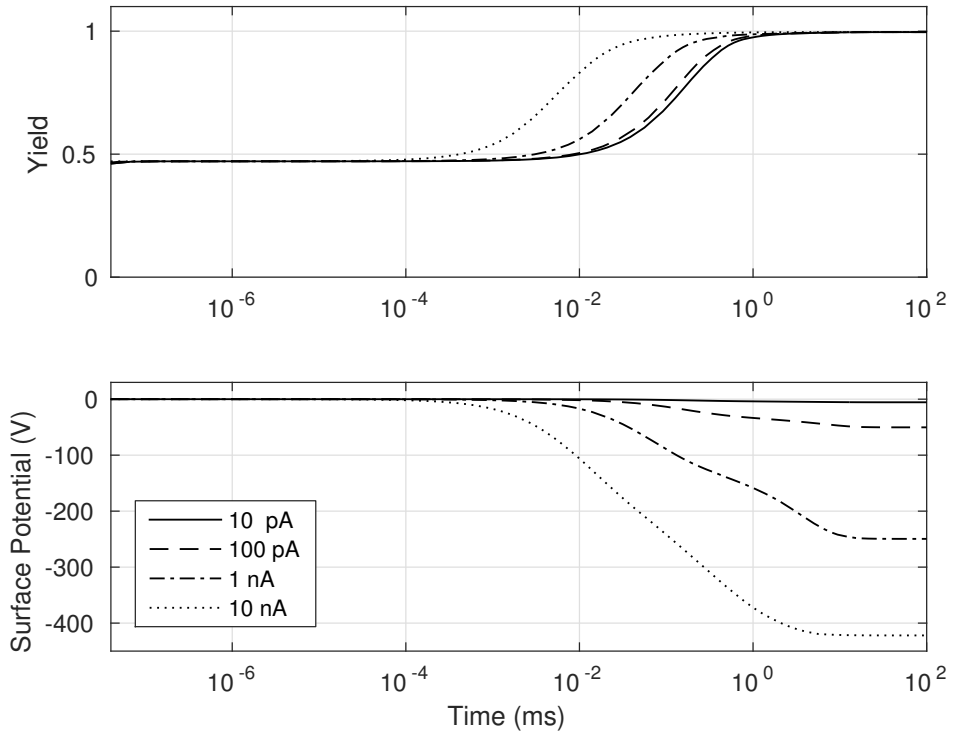

Figure 5.2: *Time evolution of the yield (top) and the surface potential at the beam entry point (bottom) for a sapphire sample continuously irradiated by a focused stationary beam at* 30 *keV PE energy – effect of beam current.*

positive surface potential reaching the value $V_{min} = 1$ V in the bottom plot of Fig. 5.1. Moreover, reverse current remains significant even after the net yield reaches unity. Thus, the unity yield is the product of a neat dynamic balance between the PE injection, positive outward SE emission, and the reverse reverse current. The result is a steady-state process and the conservation of total charge (on average): one PE in, one SE out, and a conserved 'circular' current at the sample-vacuum interface.

Figure 5.3 (sapphire) and Figure 5.4 (silica) correspond to the beam current of 100 pA and show the time evolution of the yield and potential for various PE energies. Comparison with the defocused beam irradiation of Fig's. 4.14–4.15 reveals a larger discrepancy in convergence times of the yield to unity for different energies in the focused beam case. The yield drops much sooner at lower PE energies than it increases at higher PE energies.

Similarly, from the surface potential plots of Fig's 5.3–5.4 we conclude that the rise of sub-unit yields (above 10 keV for sapphire and above 4 keV for silica) to unity cannot be explained by the change in the landing energy,

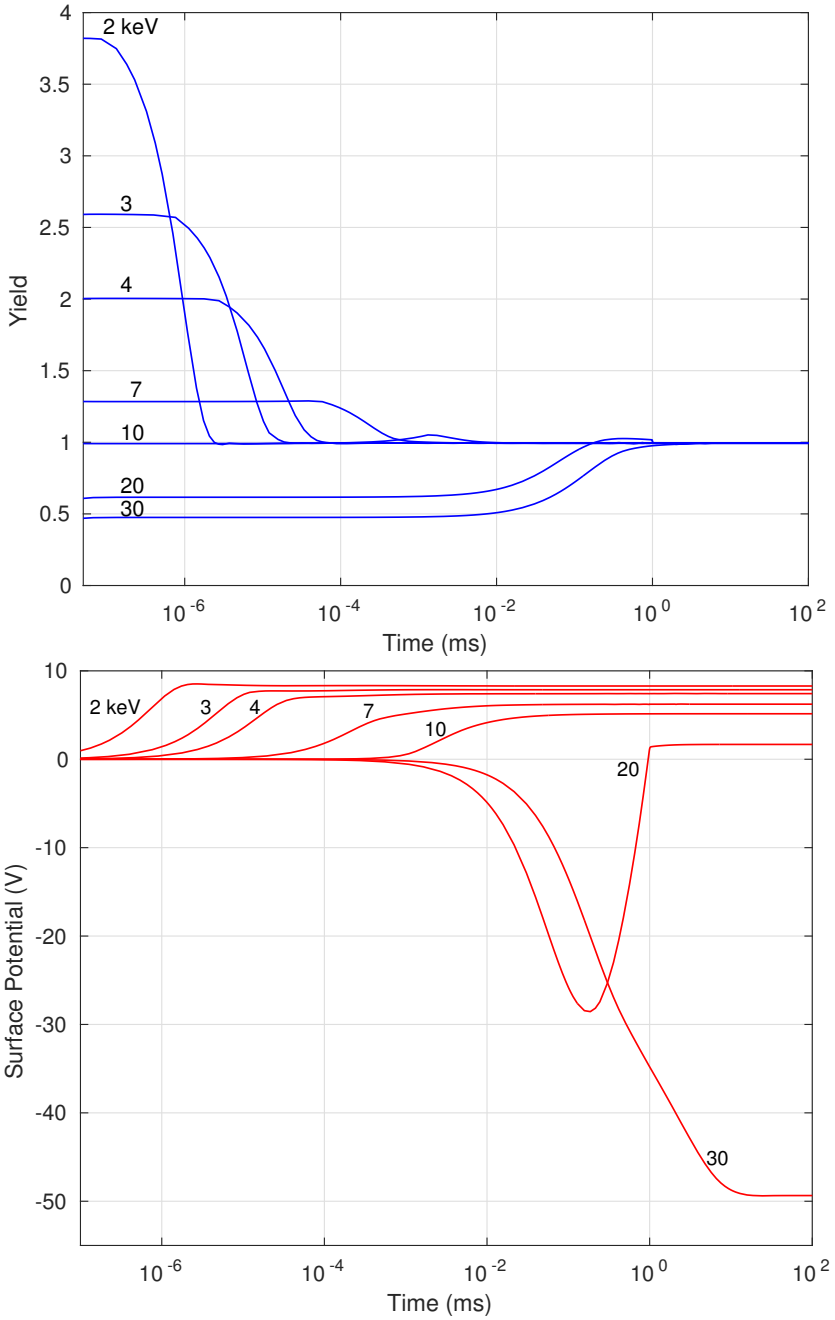

Figure 5.3: *Time evolution of the yield (top) and the surface potential at the beam entry point (bottom) for a sapphire sample continuously irradiated by a focused stationary beam of* 100 *pA – effect of PE energy.*

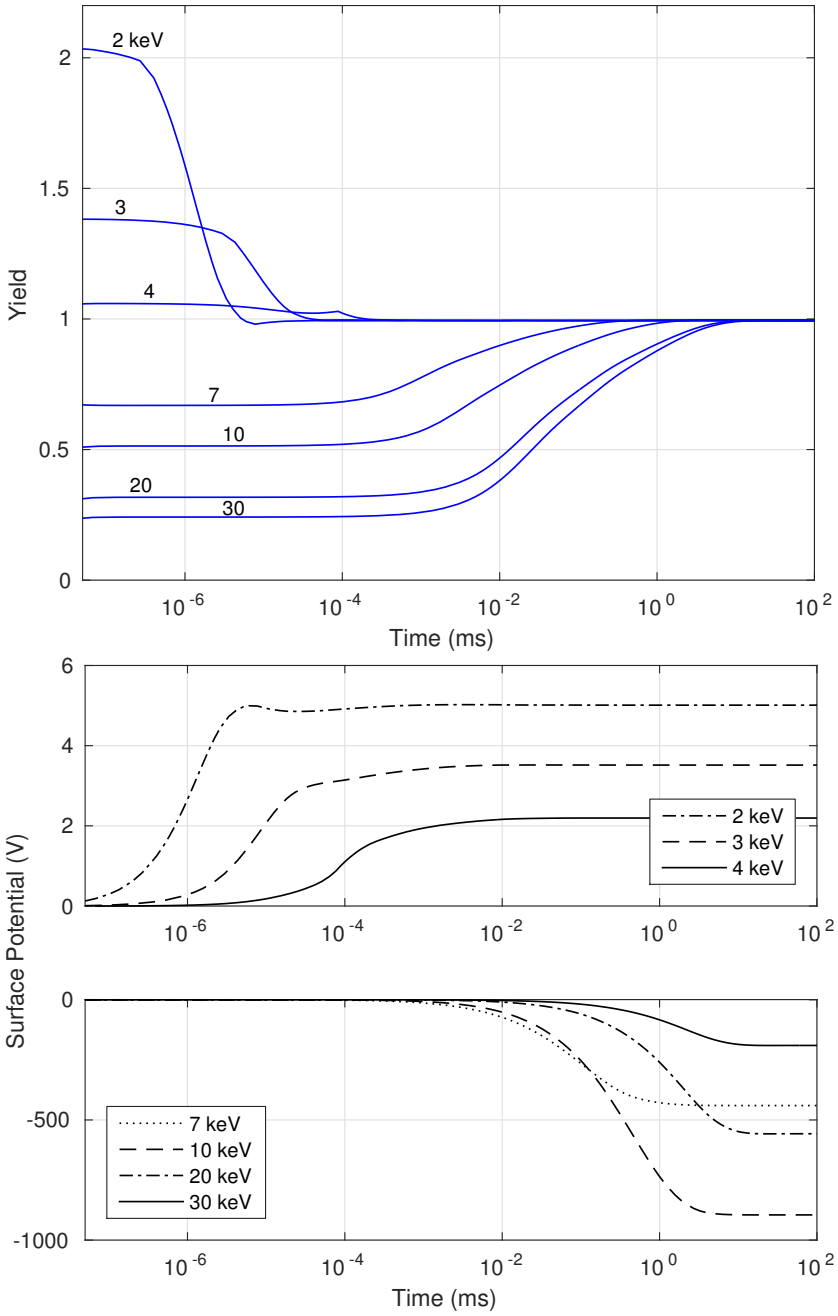

Figure 5.4: *Time evolution of the yield (top) and the surface potential at the beam entry point (middle and bottom) for a silica sample continuously irradiated by a focused stationary beam of* 100 *pA – effect of PE energy.*

as the associated potential is never negative enough for that. Minimizing the screening by removing the Dirichlet boundary Σ_1 farther away from the sample-vacuum interface Σ_2 we could bring the surface potential in silica down to -15 kV, which, however, was still not enough to decrease the landing energy of PE's from 30 keV down to the required 4.35 keV, where the standard yield of silica is equal to one. We propose a much simpler alternative explanation: sub-unit yields increase the number of free electrons near the sample-vacuum interface, which, in its turn, increases the SE emission rate up until the steady-state condition of unit yield is reached. Sometimes, as at 20 keV in sapphire and at 4 keV in amorphous alumina, the yield grows so fast that there is an overshoot, and it temporarily becomes larger than one, causing a positive surface potential, which creates the reverse current pulling the yield back to unity.

Still, while the maximal magnitude of the positive potential is indeed controlled by the reverse current, it is wrong to assume that the Σ_1 surface has no influence in this case. For instance, Fig. 5.5 corresponds to an isolated sapphire sample irradiated with a 1 nA focused beam of 5 keV PE's. It shows that a close ground contact suppresses the surface potential with positively charged samples just as well as it does with negatively charged ones. In particular, the distance of 0.1 μm to Σ_1 does not allow the potential to raise above 3 V, while, in principle, our boundary condition term $\alpha \frac{\partial V}{\partial \nu}^-$ would allow the potential to reach 10 V.

We have also performed simulations with and without the reverse current term $\alpha \frac{\partial V}{\partial \nu}^-$ in the boundary condition, see Fig. 5.6. As one can see from the plots in the first column of Figure 5.6, the effect of reverse current is not significant when the ground contact is very close to the sample surface. Plots shown in the second column of Fig. 5.6 demonstrate the increasingly important role the reverse current plays in our model when we put the ground contact further away from the sample surface.

Since the coupled DDR equations is a very difficult system to analyze, it is perhaps easier to illustrate the Σ_1 proximity effect directly with the following simple Poisson equation on a 1D domain shown in Fig. 5.7:

$$-u'' = \begin{cases} \dfrac{1}{\varepsilon_1}, & 0 \le x \le a; \\ 0, & a \le x \le b, \end{cases} \qquad u'(0) = 0, \quad u(b) = 0, \tag{5.1}$$

which structurally mimics the Poisson part of the DDR model.

Assuming u to be a continuously differentiable function ($u \in C^1$), the exact

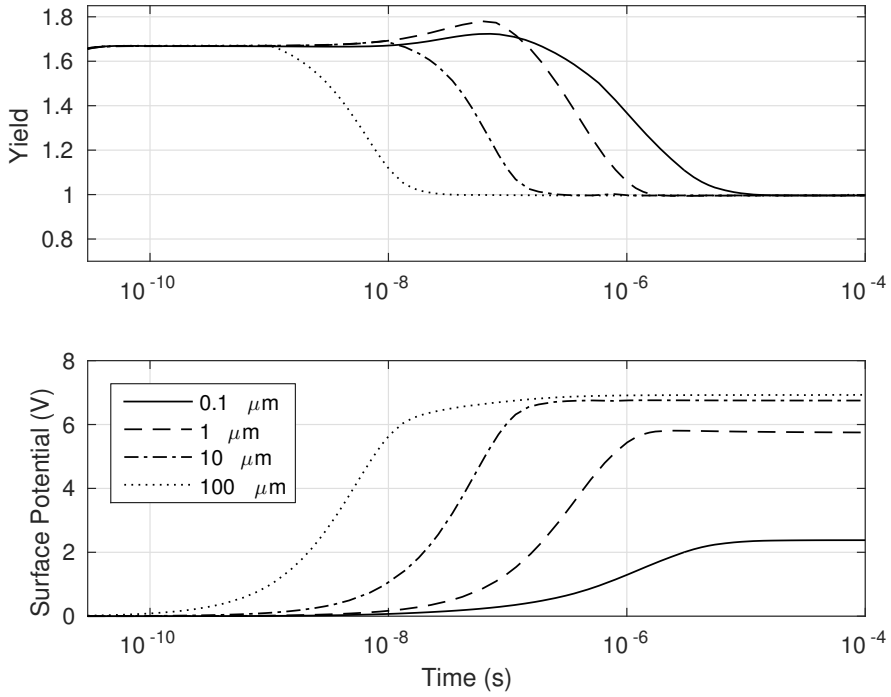

Figure 5.5: *Suppression of surface potential by the Σ_1 proximity for a positively charged sample.*

solution of equation (5.1) is

$$u = \begin{cases} -\dfrac{1}{2\varepsilon_1}(x^2 + a^2) + \dfrac{1}{\varepsilon_1}ab, & 0 \le x \le a; \\ \dfrac{1}{\varepsilon_1}(-ax + ab), & a \le x \le b, \end{cases} \tag{5.2}$$

where the linear dependency of u on the distance to the condition $u(b) = 0$ is clear, i.e. the presence of b in the solutions.

The unity yield appears to be a stable equilibrium state for isolated samples. The precise mathematical nature of this state requires further theoretical analysis, beyond the scope of this paper. At the moment we can conclude that there are two processes – reverse current and trapping – that play significant role in the approach to equilibrium. Starting from the initial state corresponding to the standard yield above unity (low PE energies), the sample gradually acquires positive charge, which turns on the reverse current and reduces the yield towards unity. The sample ends up positively charged in equilibrium with the surface potential bounded above by V_{max}.

Starting from the standard yield below unity (higher PE energies), the sample accumulates electrons, which are being transported by electrostatic

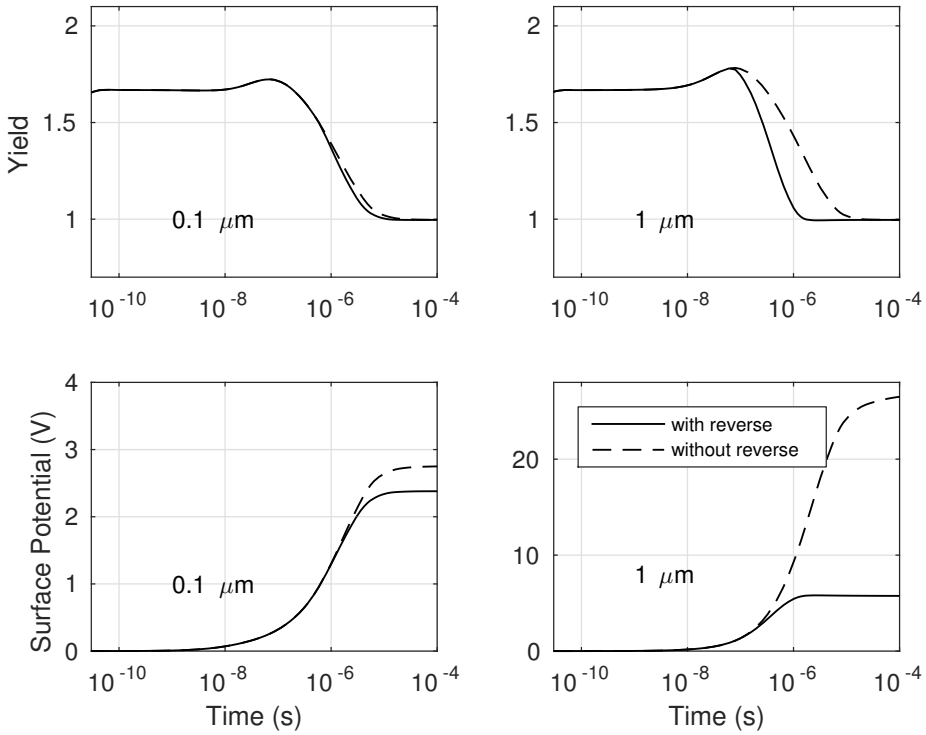

Figure 5.6: *Yield and surface potential with and without the reverse current term* $\alpha \frac{\partial V}{\partial \nu}^-$ *for close (left) and remote (right)* Σ_1.

Figure 5.7: *The considered 1D domain*

drift and collision-induced statistical diffusion towards the sample boundary. While energetic electrons coming from higher depths will initially be completely lost to trapping (which account for both the energy loss and actual trapping in our model), as traps get filled more energetic electrons will survive the transport to the sample surface. This leads to the gradual increase in the emission through the sample-vacuum interface, thereby increasing the yield.

In addition, trapping plays the role of a damping factor in the swing of the yield towards the unity. If the trapping is strong enough, then we have the so-called overdamped oscillation, where the unity yield is approached from below and remains at the unit value as soon this value is reached (30 keV in sapphire). The sample ends up negatively charged in equilibrium with the

values of the surface potential reaching a few negative kV, depending on the proximity of the Dirichlet contact.

If the trapping is relatively weak, then we have a simple damped oscillation, where the yield overshoots the unity. The resulting positive charging switches on the reverse current and the yield returns to unity. The sample ends up weakly positively charged at equilibrium in this case.

We note that the relative strength of trapping (trapping rate) depends on the local balance between the free-electron density and the number of available trapping sites.

The yield does not always have to drop/increase to unity, though. If it was the case, all insulators would look exactly the same under SEM. One possible scenario, where the yield may not converge to unity, is a (partially) grounded sample. The condition on charge conservation that requires a unit yield in an isolated sample may be relaxed if the sample is grounded. It is, of course, an open question whether a contact between an insulator and, say, a metallic grounded holder can ever be made efficient enough to allow for an easy passage of charges. Assuming for simplicity a perfect ohmic contact, the charge conservation no longer requires the exact unit yield for the sample-vacuum interface as additional electrons may enter the sample via the ground channel. This situation is illustrated in Fig. 5.8, where we have imposed an ohmic boundary condition on the side of sapphire sample. Although the yield in such a grounded sample does not stay at the level of the standard yield at that energy, after a few oscillations it stabilizes at a slightly lower value, well above unity. This effect is also observed in samples with a relatively poor ground contact described by a Robin-type boundary condition with a low surface recombination velocity.

Although, the surface potential does take longer to build up in a sample with contact, Fig. 5.8 (bottom), the behavior of the surface potential at the injection point is not very revealing. It is, perhaps, more instructive to look at the distribution of the total charge at the surfaces of isolated and grounded samples under identical irradiation conditions. While the surface potential is weaker in the grounded case, Fig. 5.8 (bottom), the images of Fig. 5.9 explicitly show that the amount of accumulated positive charge at the surface of a grounded sample is higher. Also the spatial distributions of the surface charge are different. A large disk of positive charge surrounded by a ring of negative charge is seen in the grounded sample, whereas, in the isolated sample most of the positive surface charge is concentrated around the injection point followed by a weaker positive ring some distance away.

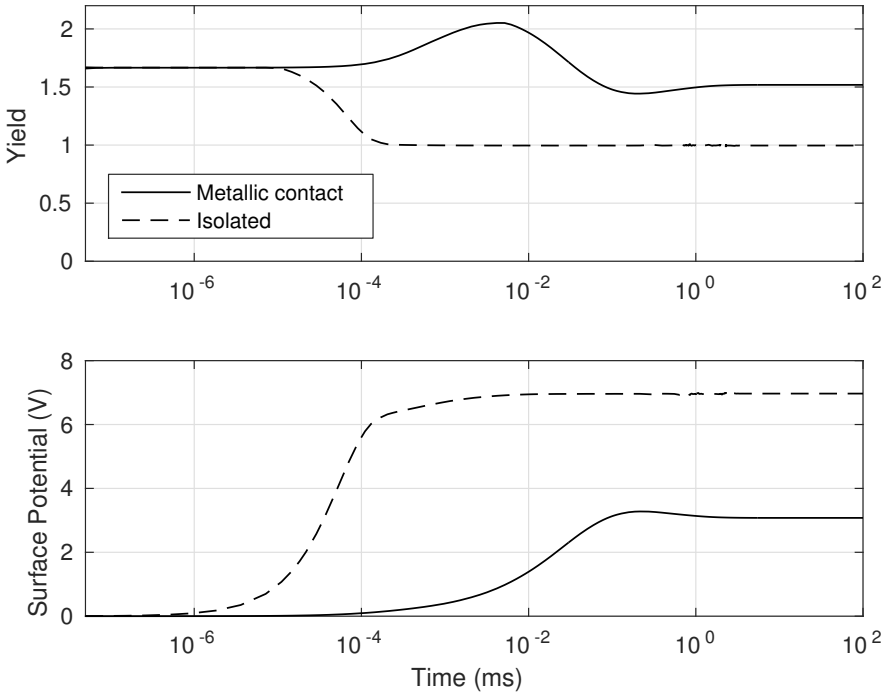

Figure 5.8: *Time evolution of the yield and the surface potential from isolated and grounded sapphire samples for* 5 *keV PE energy and* 100 *pA beam current. The distance between* Σ_1 *and* Σ_2 *is* 0.1 *mm.*

5.2 Moving beam

Another situation well-known to SEM practitioners where the yield does not drop/increase to unity is the rapid scanning of the sample by a moving focused beam. To simulate the scanning process the source function (2.51) has to be modified to account for the motion of the beam. This is achieved by setting $\mathbf{x}_0(t) = \mathbf{x}_0 + \mathbf{v}t$, where $\mathbf{v}$ is the velocity of beam displacement in the horizontal plane. Consider a 1×4 μm^2 sample surface imaged with a 1000×4000 pixels resolution at the rate of 30 frames per second. Then, the beam moves across the sample with the horizontal speed $|\mathbf{v}| \approx 33$ μm/s.

We consider an inhomogeneous sample consisting of adjacent blocks of sapphire and silica, see Fig. 5.10. Samples consisting of one insulator on top of another have been previously studied with a one-dimensional approach [24], while vertical stacks of insulators, similar to the one considered here, have been recently investigated experimentally [56].

We simulate a single scan line through the middle of the sample perpendicular to the interface between the adjacent insulators. Across the vertical in-

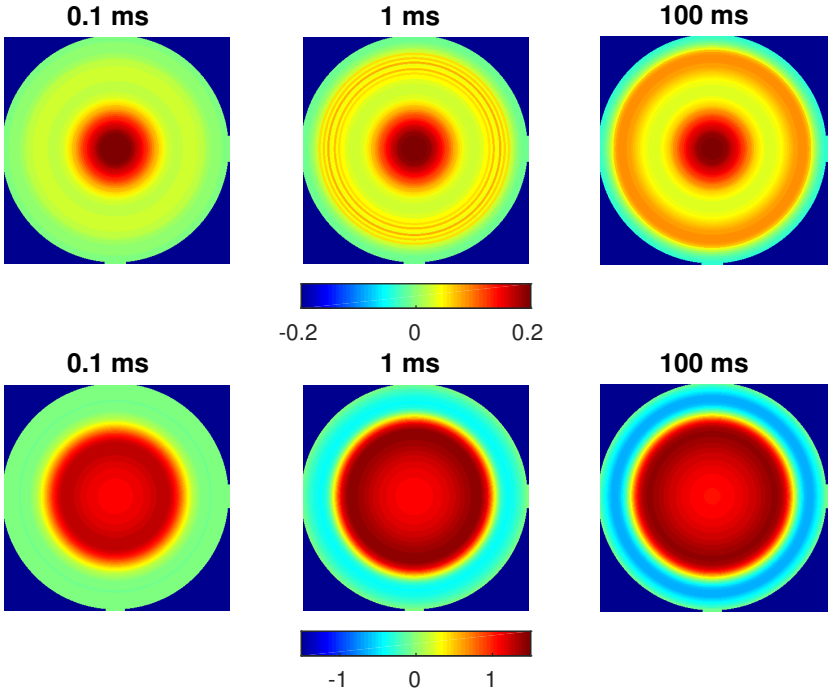

Figure 5.9: *Build up of the surface charge* $(N_T/2 + p - n - n_T)q$ (C/cm^3) *in isolated (top row) and grounded (bottom row) sapphire samples irradiated by a focused stationary* 100 *pA beam of* 5 *keV PE's. The distance between* Σ_1 *and* Σ_2 *is* 0.1 *mm.*

terface between the two different insulators the source function (2.51) exhibits a discontinuity due to the change in material density and the corresponding maximum PE penetration depth.

Since cylindrical symmetry is lost, the following DDR computations had been performed in the full three-dimensional mode. Figure 5.11 shows the yield as a function of the beam position along its trajectory for an isolated sample. These curves correspond to the intensity of pixels in a single-line SEM image. The standard yields of both insulators at the considered PE energy are also shown as dotted lines.

First of all we notice the difference between the left-to-right (from sapphire to silica) and the right-to-left (from silica to sapphire) scanning modes. This difference is easy to understand by looking at Figs. 5.12, 5.13, 5.14 and 5.15 where the images show the surface charge and potential during these two scans. Since the charging of sapphire is stronger than that of silica, the resulting residual charge strongly depends on the scan history.

Otherwise, the scans of Fig. 5.11 have several common features. One can

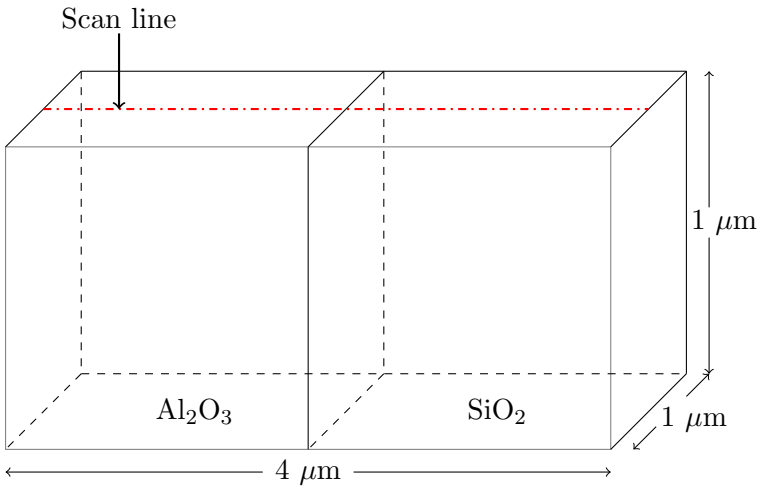

Figure 5.10: *An inhomogeneous sample consisting of vertically stacked sapphire and silica blocks.*

notice higher yields in the neighborhood of the sample edges due to increased emission via the vertical interfaces. This is a well-known effect – the sample edges look brighter in SEM images compared to the rest of the sample surface. One can also see the drop of the yield towards unity during left-to-right scanning due to continuous charging of the sapphire part. This charging also causes the yield at the beginning of the silica part to drop below its standard value. The relatively smaller charging during the right-to-left scanning does not allow the yield in silica to reach its standard below-unity value after the initial edge-related surge, and pushes the yield below the standard value when the beam crosses into the sapphire part. Additional simulations show that reducing the beam current (down to a few pA) while maintaining a high beam displacement velocity gives scans that truthfully reflect the standard yields of each part of the sample. Unfortunately, in practice this would, probably, result in a bad signal to noise ratio.

5.3 Modelling of charge transport in detector membranes

We devote the final section of this study to a more applied subject, which concerns electron multipliers. An electron multiplier is a vacuum-tube structure that multiplies incident electrons. In a process called secondary emission, a single electron can induce emission of more than one electron. The use of an electron multiplier is most prominent in the area of detectors. Although

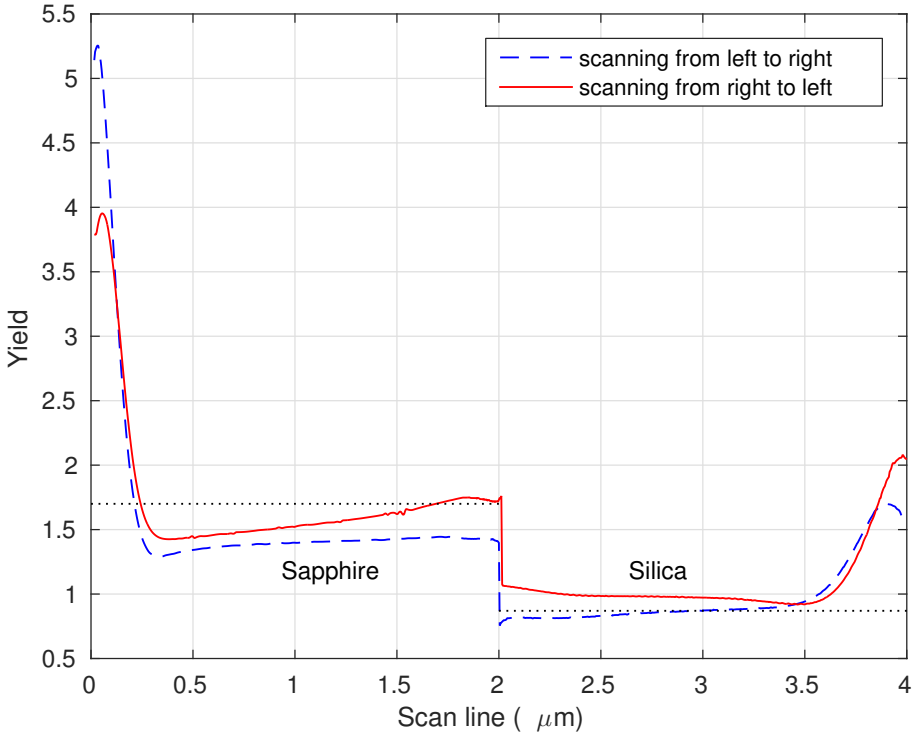

Figure 5.11: *Yield as a function of beam position while scanning an inhomogeneous sapphire-silica sample with a focused* 10 *pA beam of* 5 *keV PE's. Dotted – standard yield.*

detectors usually rely on the refection secondary emission, in some detectors, the transmission secondary emission is used.

The recently proposed detector so called Tynode [2] is among those that use transmission secondary electrons. This detector takes advantage of a stack of transmission dynodes on top of a pixel chip, as shown in the schematic representation in Fig. 5.16. A special feature of its structure is that the detector is made of ultra thin membranes. The mechanism is such that an energetic electron collides with one side of the membrane, which results in the emission of multiple electrons from the other side. The continuation of this process over a stack of membranes leads to the production of a significant amount of electrons, that can be detected. In order to achieve a high rate of secondary emission, the membranes are usually made of insulators.

The main objective of the present study is to investigate the effects of the PE energy and the membrane thickness on the electron yields of dynodes. While other simulations were carried out with the Monte Carlo technique, the DDR method was used for a better understanding of the underlying mecha-

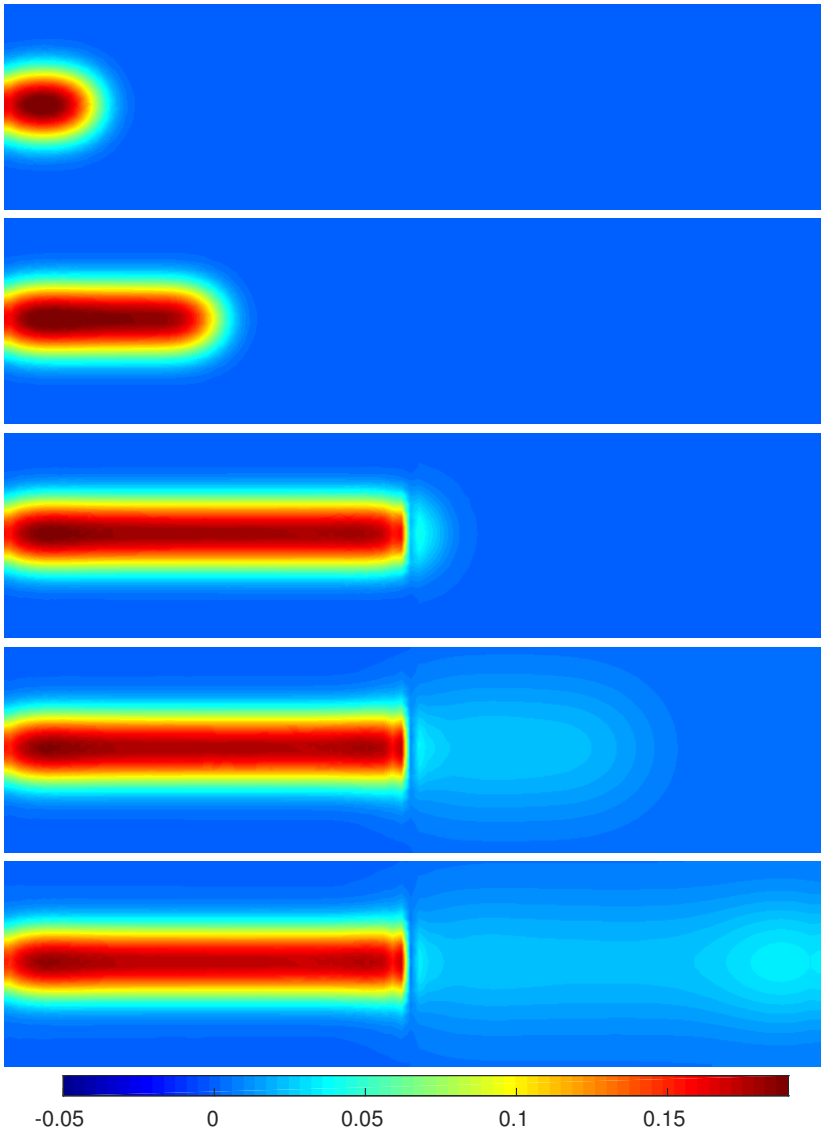

Figure 5.12: *The surface charge* $(N_T/2 + p - n - n_T)q$ (C/cm^3) *at the initial, middle and last stages of scanning with a focused e-beam of* 5 keV *and* 10 pA. *Scanning from sapphire to silica.*

nisms as well as for further validation of the obtained results. Our aim here is to see if there is a consistency between the results obtained from the DDR model and the experimental results shown in the figure 5.17.

For several reasons, the results of the present model are expected to be compatible with experimental data mostly in terms of quality, and not neces-

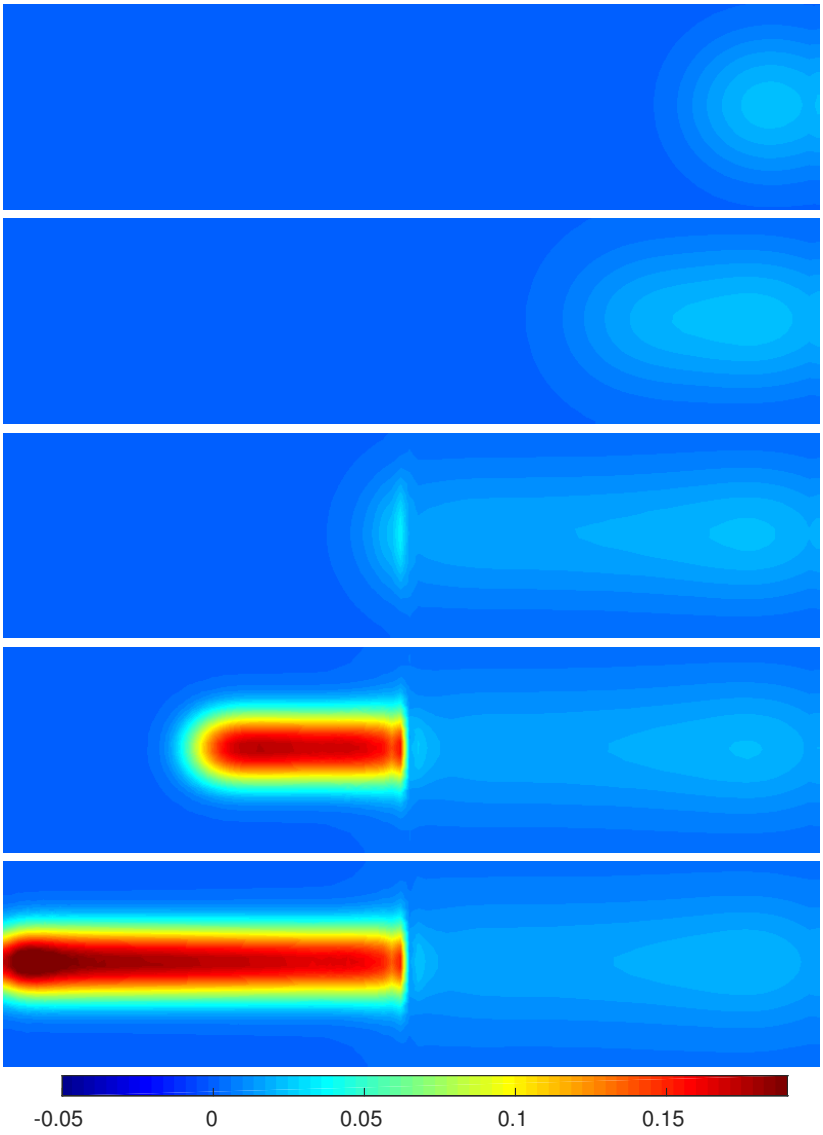

Figure 5.13: *The surface charge* $(N_T/2 + p - n - n_T)q$ (C/cm^3) *at the initial, middle and last stages of scanning with a focused e-beam of* 5 keV *and* 10 pA. *Scanning from silica to sapphire.*

sarily quantitatively. The first reason is that the yields shown in Fig. 5.17 are the result of the rapid scanning electron mode, while in our simulations we shall be relying on the single PE impact model , i.e., the standard SE yield. In fact, these experimental data are also presented to be free of charging effects, which has been achieved through an extremely thin coating of titanium

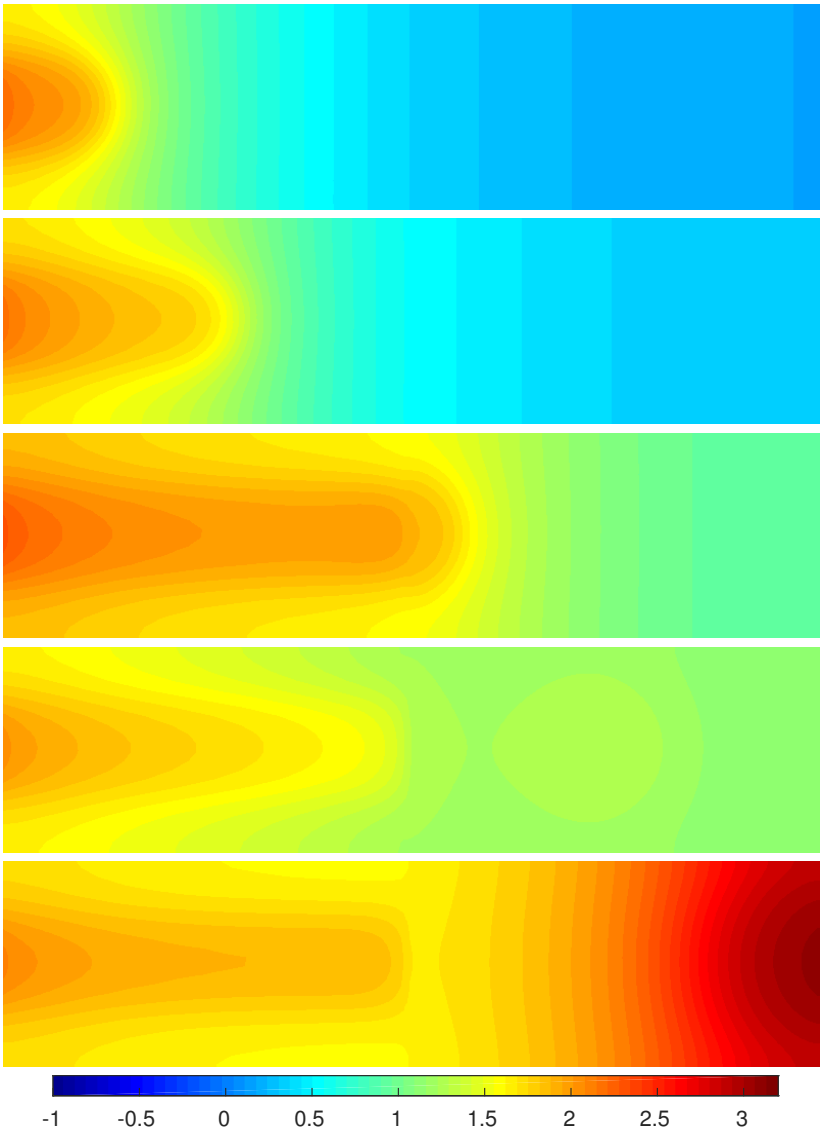

Figure 5.14: *The surface potential at the initial, middle and last stages of scanning with a focused e-beam of* 5 *keV and* 10 *pA. Scanning from sapphire to silica.*

nitride (TiN) on the ALD alumina membrane. The second reason is related to this coating, which due to the current uncertainty about the bulk properties of TiN was not included in the model. Given that the bulk properties of sapphire are fully known, in the first simulation, it is also assumed that the membrane is made of sapphire. The membrane is modelled as a disk with the

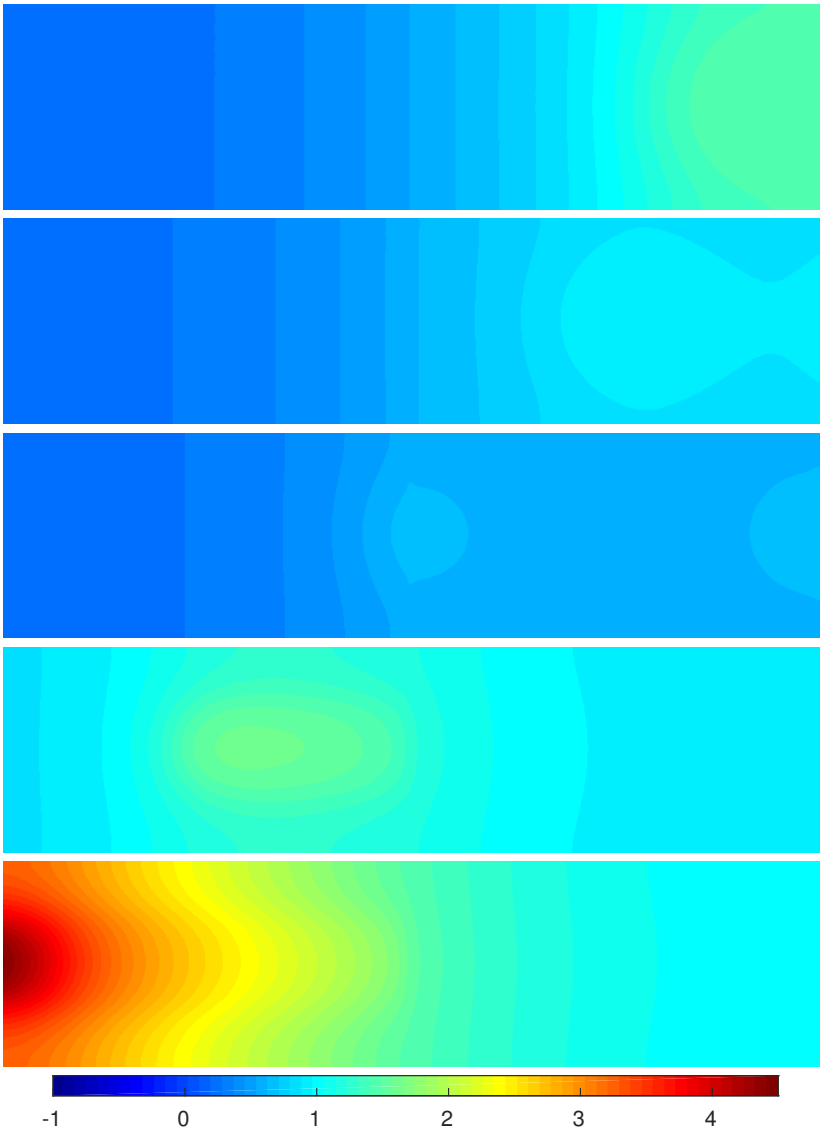

Figure 5.15: *The surface potential at the initial, middle and last stages of scanning with a focused e-beam of* 5 keV *and* 10 pA*. Scanning from silica to sapphire.*

radius of 1 μm for three thickness values (15, 30 and 55 nm). The schematics of the model is shown in Fig. 5.18 and the imposed boundary conditions are as follows

$$V = 0, \quad \text{on} \quad \overline{OD} \ \& \ \overline{CG}; \tag{5.3}$$

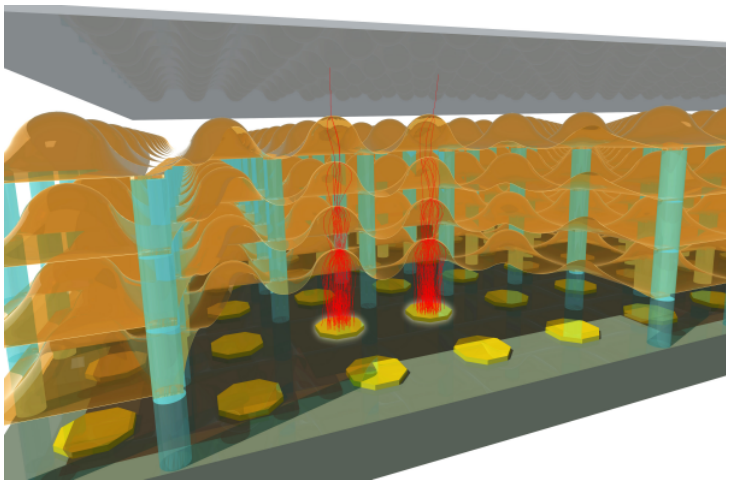

Figure 5.16: *The core of the newly proposed detectors: a stack of transmission dynodes in vacuum. The figure has been taken from Ref. [2].*

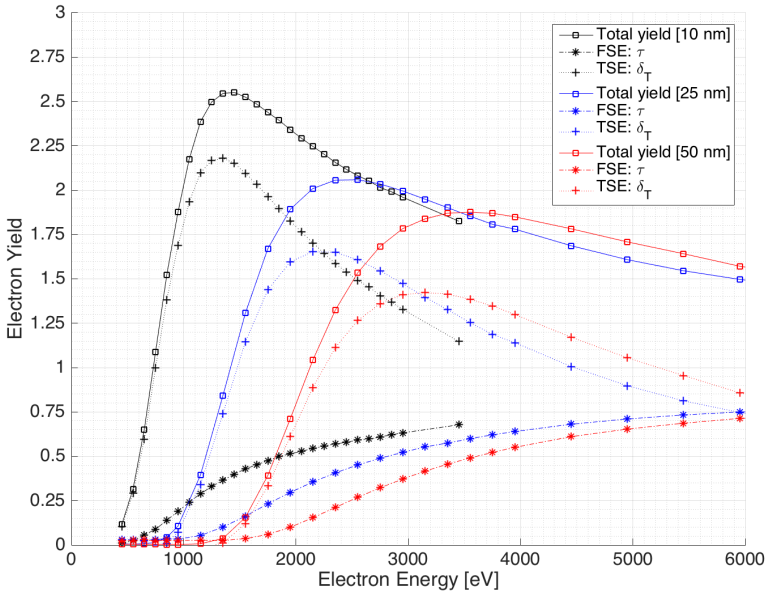

Figure 5.17: *Transmission electron emission yields of a Tynode consisting of a conductive titanium nitride layer (5 nm) and a layer of ALD alumina (of* 10, 25 *and* 50 *nm). The figure has been taken from Ref. [2].*

$$\frac{\partial n}{\partial \boldsymbol{\nu}} = 0, \quad \frac{\partial p}{\partial \boldsymbol{\nu}} = 0, \quad \frac{\partial V}{\partial \boldsymbol{\nu}} = 0, \quad \text{on} \quad \overline{EF}; \tag{5.4}$$

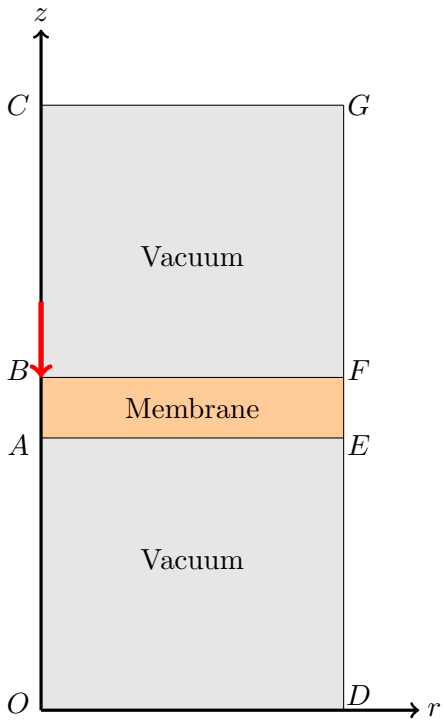

Figure 5.18: *General schematics of the problem.*

$$\mathbf{J}_n \cdot \boldsymbol{\nu} = v_n(n - n_i) - \alpha \frac{\partial V^-}{\partial \nu} \quad \text{if } n > n_i \quad \text{on} \quad \overline{AE} \ \& \ \overline{BF}; \tag{5.5}$$

$$\mathbf{J}_p \cdot \boldsymbol{\nu} = 0 \quad \text{on} \quad \overline{AE} \ \& \ \overline{BF}. \tag{5.6}$$

Except for the source term, most parts of the model are similar to those in Chapter 2. Since the PE penetration depth may happen to be greater than the thickness of the membrane, a particular attention should be paid to the modeling of the source term by accounting for the primary electrons emerging from the other side of the membrane. Here, we consider a part of the charge distribution, which is spatially located in the membrane, as the source term. Accordingly, the probability for the PE to pass through is calculated based on the other part of the charge distribution. Therefore, the model can be stated

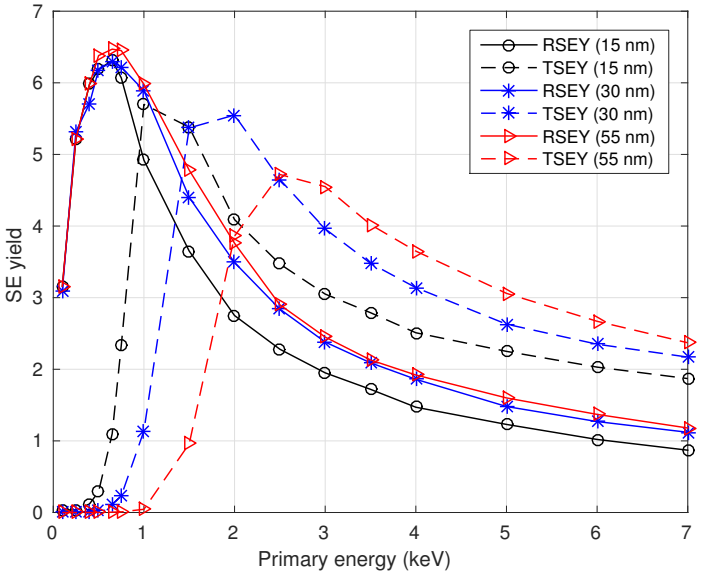

Figure 5.19: *Self-consistent simulation of reflection and transmission (including forward scattered) secondary electron yield from sapphire membranes for three thickness values (15 nm, 30 nm and 55 nm) under the impact of single primary electron of different energies.*

as follows:

$$
\begin{aligned}
g_{n,p}(\mathbf{x}, E_0) &= \left(A\frac{E_0}{E_\mathrm{i}} + B(1 - N_{FSE}) \right) \frac{1}{\pi R^3} \exp\left(-C|\mathbf{x} - \mathbf{x}_0|^2\right), \\
N_{FSE} &= \frac{B}{CR^3} \int_{(b-R)}^{a} \exp\left(-C|z - z_0|^2\right) dz, \\
a &= \overline{OA}, \quad b = \overline{OB},
\end{aligned}
\tag{5.7}
$$

where A, B and C are the same as in the formula (2.51). The N_{FSE} determines the rate of forward scattered electrons.

As we already mentioned, we have considered sapphire membranes for the first experiment. The results shown in Fig. 5.19 indicate that both the reflected SE yield (RSEY) and the transmitted SE yield (TSEY) of sapphire are larger than the experimental results for ALD alumina. This shows the significant difference between these two types of alumina in terms of secondary emission capability. Perhaps the important point about the results, shown in Fig. 5.19, is the apparent effect of the membrane thickness on the SE yields. This effect on the reflective SE yield for low PE energies is negligible, because the penetration depth is very small, so even a very thin membrane can cover it.

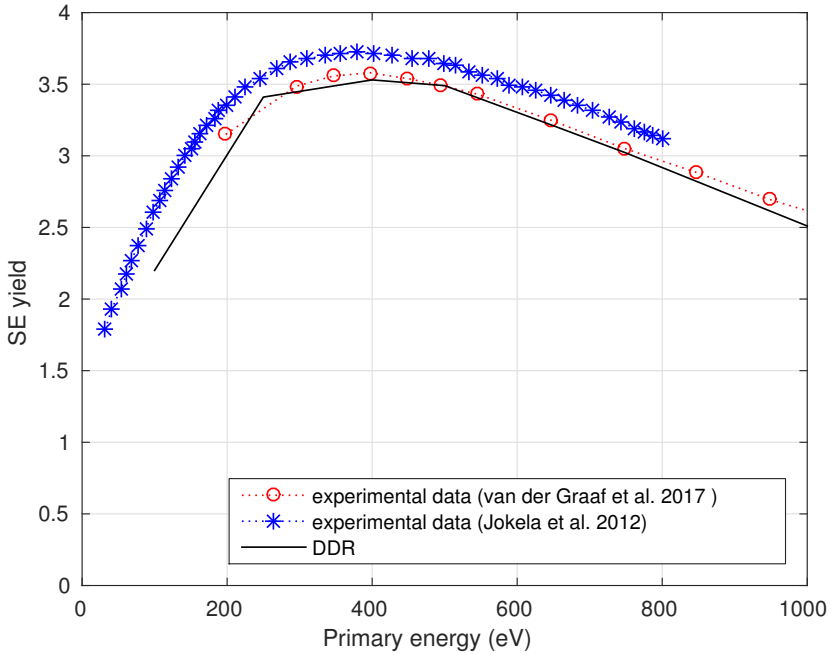

Figure 5.20: *Reflection SEY obtained by the experimental investigations of van der Graaf et al. [2] and Jokela et al. [95] and DDR model for ALD alumina with thicknesses of* 12.5*,* 20 *and* 15 *nm, respectively.*

Our investigation showed that the main difference between the sapphire and ALD alumina is that the sapphire is crystalline [91, 92], while ALD alumina is amorphous [93, 94]. Therefore, it is reasonable to assume that the trap density of ALD alumina is higher than that of sapphire. With this in mind, we conducted a series of numerical experiments to obtain an estimate for the trap density of ALD alumina. In these experiments, except for the trap density, the other parameters were exactly the same as those for sapphire. Our analysis indicates that the use of three times the trap density of the sapphire for ALD alumina leads to the results shown in Fig. 5.20, that are in close with the experimental data.

Based on this finding, we were able to carry out the same analysis for the ALD alumina membrane as for the sapphire membrane. The results, presented in Fig. 5.21, show that although the agreement with the experimental data is still not close, it is more satisfactory. The clear difference with the sapphire membrane, the clear difference is that the effect of the membrane thickness on the SE yield, especially for the reflective SE yield, is less significant for the ALD alumina membrane. Since the only difference is in their trap density, it can be said that the lower the trap density, the greater the effect of the

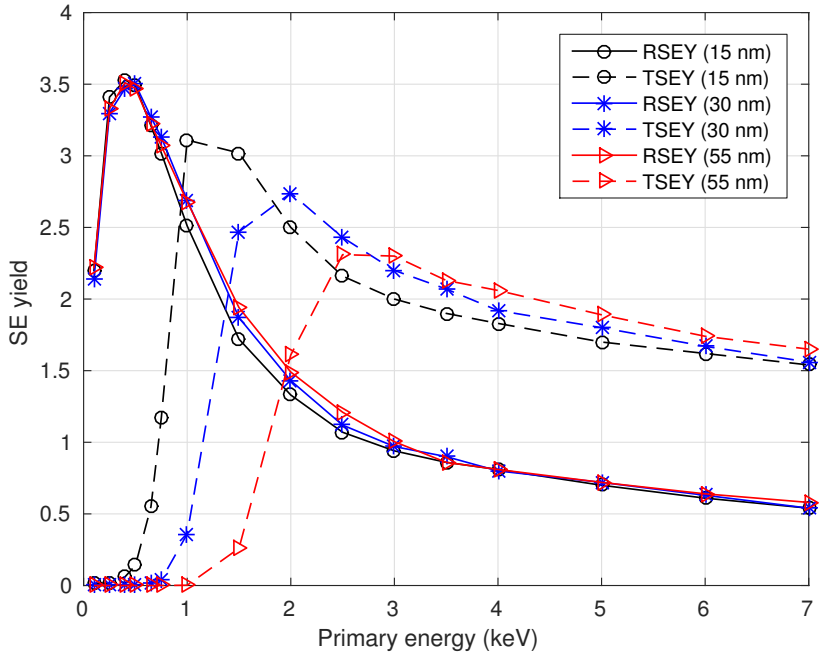

Figure 5.21: *Self-consistent simulation of reflection and transmission (including forward scattered) secondary electron yield from ALD alumina membranes for three thickness values (15 nm, 30 nm and 55 nm) under the impact of single primary electron of different energies.*

thickness on the SE yield. Perhaps another conclusion that can be drawn is that the thickness plays a more important role in semiconductors in terms of SE yield capability.

All of the above analysis was based on the impact of a single electron, and the effect of the TiN coating was not included. For the reasons given above, at present, modeling of the coating is not possible. However, one can assume that the coating achieves a better electrical contact with the ground, providing a sink for the accumulated charge and/or a source of additional charges. Thus, in the next simulations the focus is on the effect of the ohmic contact at the edge of the ALD membrane. Namely, we assume that without the TiN layer the poor contact of the ALD membrane with its support does not allow for a free charge transport/recombination and the particles can escape the membrane exclusively via its upper and lower interfaces at a rate governed by the surface recombination velocity.

Since the effect of the ohmic contact can only be evaluated in the presence of electron bombardment, we have conducted experiments with the ALD alumina membrane under electron bombardment, with and without providing

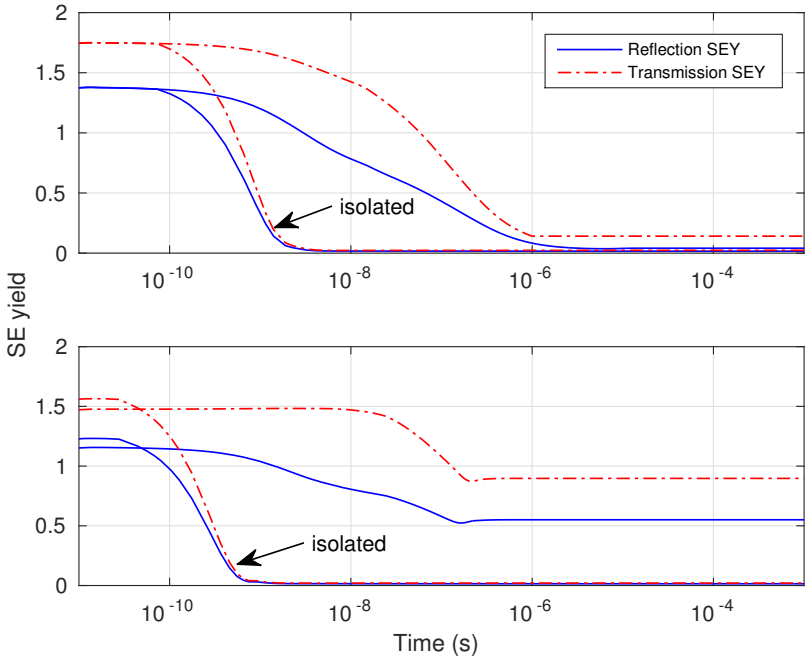

Figure 5.22: *Time evolution of the SE yield for the ALD alumina membranes continuously irradiated by a focused stationary beam at* 2 *keV PE energy and* 1 *nA beam current. The upper and lower figures correspond to the membrane with the radius of* 100 *and* 50 *nm, respectively. The thickness of the membrane is* 15 *nm.*

the electrical contact. If the ohmic contact is applied, the boundary conditions at $\overline{EF}$ will be changed as follows:

$$n = n_i, \quad p = n_i, \quad V = 0, \quad \text{on} \quad \overline{EF}; \tag{5.8}$$

otherwise, the conditions are kept the same as in (5.3), (5.4), (5.5) and (5.6). The PE energy and the beam current are considered 2 keV and 1 nA, respectively. With the PE energy of 2 keV, the primary electrons can reach a maximum depth of approximately 90 nm. Considering this, we choose the membrane radius of 100 and 50 nm, with the aim that the first membrane with one of the two horizontally covers the source charge distribution, while the second doest not.

Figure 5.22 presents the time-domain evolution of the reflection and transmission SE yields obtained from isolated and grounded membranes. What is evident from Fig. 5.22 is the rapid and severe drop in the SE yield for the isolated membrane. Another noteworthy point concerns the steady state of the SE yields, which is higher in the case of the smaller radius. A possible

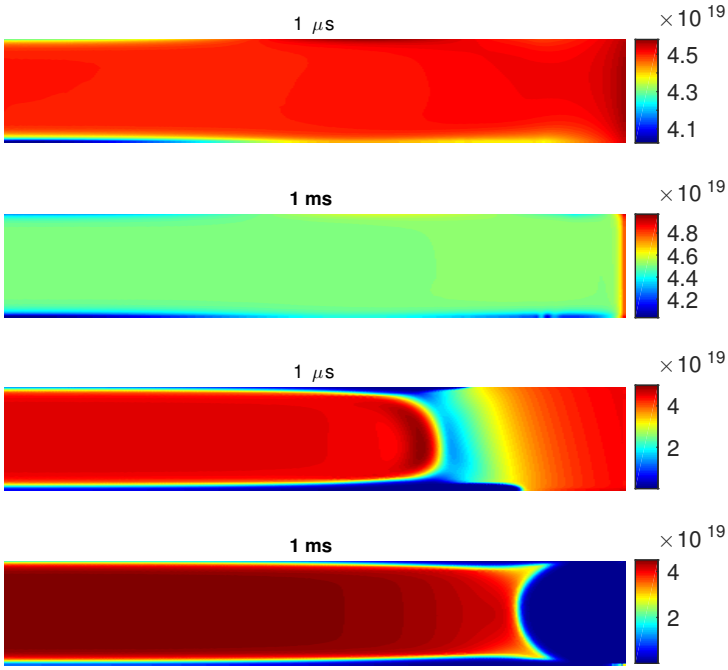

Figure 5.23: *The evolution of the density of trapped electrons in isolated (the two upper figures) and grounded (the two lower figures) ALD alumina membranes irradiated by a focused stationary* 1 *nA beam of* 2 *keV PE's. The thickness and radius of the membrane are* 15 *and* 100 *nm, respectively.*

explanation for this might be that with the smaller radius, the charge pairs are generated in the adjacent area to the ground contact. Therefore, in this case, it is expected that the process of interactions between charges, and in particular the transfer of charges through the ground contact, are different.

The last figure in this dissertation corresponds to the evolution of the trapped charge. Figure 5.23 shows the density of trapped electrons at certain times for both isolated and grounded membranes. The results show a significant difference between the distribution of trapped electrons in these two cases. Similarly, but not to the same extent, the electron detrapping is a dominant process at interfaces with vacuum for both isolated and grounded membranes. Also, as can be seen from Fig. 5.23, the process that occurs at the isolated interface is the electron trapping, while at the ground contact, a strong electron detrapping is observed.

6

Conclusions and recommendations

In this Thesis a self-consistent drift-diffusion-reaction model for the time-domain analysis of charging phenomena in electron-beam irradiated insulators has been presented. The DDR model is a simplified formulation of the Boltzmann transport equation with minimal modifications to account for the pulsed and non-equilibrium nature of the charge injection mechanism and the back reaction of the accumulated charge on the incoming primary electrons. We have presented and compared two approaches to the charge injection problem. The first one is a pulsed source model reflecting the actual discrete nature of the electron beam. The second approach reduces the computational burden by applying a temporal average of the actual pulsed source function, which allows simulation at much longer time scales. Our results show an acceptable agreement between these two approaches. We have further devised several source models with regard to different modes of electron bombardment including focused and defocused beams, either stationary or moving. The proposed model features a novel semi-permeable boundary condition at the sample-vacuum interface reflecting the fact that the electrons are allowed to go through the boundary, while holes are not, and also taking into account the reverse electron current.

The finite element method was selected as the method of choice for the numerical solution of the model equations. Our investigations show that the balance between the accuracy and the computational cost can be achieved by using local mesh refinement, Lagrange shape functions (of first and second order), the fully coupled approach with the Newton-Raphson solver, and an adaptive time-stepping algorithm. Regarding the meshing strategy, a fine mesh is required for the impact zone and wherever there is a passage for the electric current, e.g. the sample-vacuum interface and interfaces with metal. In many cases it was possible to take advantage of the spatial cylindrical (axial)

symmetry and extract 3D results from 2D computations.

In reviewing the literature on semiconductor device modelling with the drift diffusion equation, one would realize that the instability of numerical solvers has always been the main concern and, therefore, many approaches have been developed to tackle the issue. Here, we have seen that, owing to the presence of low mobilities, homogeneous Neumann conditions and considering either homogeneous materials or materials with the same intrinsic carrier concentration, the present solver does not face this difficulty, i.e. neither drift-dominated regime nor steep gradients in the diffusion term occur.

The method has been calibrated against experimental data do deliver exact standard yields for alumina and silica samples over a wide range of PE energies. For alumina and silica all calibrated parameters remain within or close to their reported uncertainty bounds, thereby further confirming the acceptability of model approximations. The consistent and realistic results were possible through a detailed analysis of sensitivity to the parameters involved in the model. The findings of the sensitivity analysis can be summarized as follows. The shape of the yield-energy curve is influenced by the capture cross section and the density of traps. Namely, the larger the trap density and the capture cross section, the lower is the high-energy tail of the curve. Following any one of the published penetration depth formulas together with adjusting the values of material parameters within their permitted ranges does not produce yield-energy curves fully compatible with the experimental data over the whole range of PE energies. The surface recombination velocity (SRV) affects mainly the height and not the shape of the yield-energy curve. Eventually we restored to tuning the penetration depth for low beam energies while for higher energies, the depth follows one of the empirical formulas from the literature.

Tuning also appeared to be the only way to estimate the SRV at the sample-vacuum interface. In this regard, we have devised an optimization procedure to deduce the SRV of insulators in the vacuum from the experimental SE yield data. Moreover, to get a further insight into the concept of the SRV, we have shown how the concept is rooted in the Boltzmann theory. This investigation revealed that the SRV is a time-dependent factor. However, for the sake of simplicity and to be consistent with the purpose of simulation at long time scales, the SRV is assumed to be a time-independent material property which it interpreted as the time-averaged value of the realistic SRV.

Single PE impact studies gave valuable insight into the aftermath following the injection of a single primary electron revealing the dynamics of all particle species and the electric potential. The contribution of both free and trapped charges to the total charge has been evaluated, indicating the primary role of trapping/detrapping processes in the charging effect. Further simulations have been conducted with more PE impacts in which we have compared the idealistic pulsed source model with the alternative continuous source model.

The results indicate a reasonable agreement between both models.

Time-domain simulations with defocused beams have been compared to the previously published results from a one-dimensional Flight-Drift model demonstrating similar long-time behavior. Our investigations so far show that the initial high-energy transport stage can, indeed, be approximated by a semi-empirical source function and low-energy material parameters, whereas, subsequent transport stages fall within the original domain of validity of the low-energy DDR method.

Simulations with stationary focused beams allowed us to have a better understanding of the role of each of the factors separately. The investigations have shown that the time-behavior of the SE yield and the surface potential is affected by many factors, including the PE energy, the beam current and the quality and proximity to the ground contact. As expected, the results also confirm that in electrically isolated samples the yield collapses to unity after a certain number of primary electrons, which depends on the PE energy, has been injected roughly at the same location on the sample surface. However, our simulations do not support the widespread intuitive explanation of this phenomenon in terms of the changing landing energy of PE's. The effect appears to have dynamic origins and is related to transient changes in the distribution of charges close to the sample surface.

The reason for the unity yield cannot be solely attributed to the effects of the reverse current and trapping/detrapping processes, although we have found that these two effects have a significant impact on SE yield. To substantiate this point, we have conducted several simulations while either one of these effects or both of them were turned off. In fact, the results indicate their impact on "how" not "why" the yield arrives at unity. Therefore, a conclusion can be drawn from our study that the unity yield is an equilibrium state of isolated samples, regardless of their conductivity, i.e. no matter the sample is an insulator, semiconductor or metal.

The surface potential, and especially it's magnitude, is strongly affected by the proximity of metallic grounded surfaces due to the associated charge screening. This fact was analytically confirmed on a much simpler electrostatic model. In addition, numerical evidence showed that the beam current is also a factor affecting the surface potential which is in accord with some earlier studies. Moreover, we have seen that in the presence of reverse current (i.e. positive surface potential), the beam current affects only the time-domain behavior of the surface potential; while, when the surface potential is negative, it affects also the magnitude of the potential. Therefore, the second major finding of our study is that the surface potential is not unique with respect to the PE energy, which in fact would be contrary to the assumption of the above mentioned widespread model. This assumptions may thus lead to misinterpretation of charging effects, if one relies solely on the surface potential

measurements, but also may present an opportunity to alleviate SEM image distortions. Our simulations show that a good ground contact could also prevent the collapse of the yield to unity.

We have presented, probably, the first 3D simulations of a laterally inhomogeneous sample irradiated by a moving beam taking into account both the dynamic charge trapping/detrapping and the reverse electrons. While to a certain extent the yield obtained during this realistic simulations could be interpreted on the basis of time-domain results with stationary beams, some effects are unique to dynamic scanning. For example, the scan profile appears to depend on the direction of scanning.

Simulation of the SE yield and charge transport in the recently proposed electron multiplier was also presented. In this study, we were able to investigate the effect of the thickness on the emission yields of sapphire and ALD alumina. It is interesting to note that by simply increasing the corresponding trap density and retaining the other assumptions we used for sapphire, we obtained the yields for ALD alumina consistent with experimental data. Our study also examined the importance and impact of the quality of the contact for enhancing the SE yield in dynode membranes.

A recent review by Walker et al [18] mentions the lack of reliable simulations related to low-energy SEM studies. We partly fill this gap with the present modified and calibrated version of the DDR method. Our method, as well as other simulation software, would greatly benefit from publicly available high-quality time-domain data in addition to the already available standard yields. While we realize that direct time-domain sampling of detector currents may be difficult, it should be possible to collect and publish single line scans of ~ 1 μm insulator targets for a range of dwell times (scan speeds).

While the present minimal extension of the standard DDR method from semiconductor physics gave some valuable insights into the charging phenomenon of e-beam irradiated insulators, we believe that several improvements are possible. Without resorting to the full-blown Boltzmann transport equation one can still consider the transport of free electrons belonging to different energy bands separately. In the present context it may be interesting to split the free electrons into two species - those that have enough energy to exit the sample and those that do not and introduce additional transport and reaction equations into the model.

On the computational side, the practically important cases of highly heterogeneous materials with strongly varying intrinsic carrier concentrations may require a more sophisticated discretization strategy and error control.

A

Generation-recombination model

The differential of the electron capture rate R_n at energy E can be stated as follows [36, 29],

$$dR_n = k_{nc}(E)(N_T - n_T)f_n(E)g_c(E)dE, \tag{A.1}$$

where $f_n(E)$ is the energy dependent distribution function of free electrons, $g_c(E)$ is the density of states for electrons and k_{nc} is a proportionality constant. The density of states (DOS) is the number of different states at a certain energy level that carriers are allowed to occupy.

The amount of electrons in the conduction band can be found by the following integration

$$n = \int_{E_c}^{\infty} n(E)dE = \int_{E_c}^{\infty} f_n(E)g_c(E)dE. \tag{A.2}$$

The differential of the hole capture rate v_{pc} at energy E can be stated as follows,

$$dR_p = k_{pc}(E)n_T f_p(E)g_v(E)dE, \tag{A.3}$$

where $f_p(E)$ is the energy dependent distribution function of free holes, $g_v(E)$ is the density of states for holes and k_{pc} is a proportionality constant.

The amount of holes in the valence band is obtained by the following integration

$$p = \int_{-\infty}^{E_v} p(E)dE = \int_{-\infty}^{E_v} f_p(E)g_v(E)dE. \tag{A.4}$$

The differential of the hole emission rate v_{he} at energy E can be stated as follows,

$$dG_p = k_{pe}(E)(N_T - n_T)(1 - f_p(E))g_v(E)dE, \tag{A.5}$$

where k_{pe} is a proportionality constant.

For the electron emission rate, we have

$$dG_n = k_{ne}(E)n_T(1 - f_n(E))g_c(E)dE, \tag{A.6}$$

where k_{ne} is a proportionality constant.

The net generation/recombination rates for electrons and holes are

$$\begin{aligned} &dR_n - dG_n = \\ &(k_{nc}(E)(N_T - n_T)f_n(E) - k_{ne}(E)n_T(1 - f_n(E)))\, g_v(E)dE, \end{aligned} \tag{A.7}$$

$$\begin{aligned} &dR_p - dG_p = \\ &(k_{pc}(E)n_T f_p(E) - k_{pe}(E)(N_T - n_T)(1 - f_p(E)))\, g_v(E)dE. \end{aligned} \tag{A.8}$$

In thermal equilibrium, the emission and capture rates for electrons and holes should be equal, which means

$$dR_n - dG_n = dR_p - dG_p = 0. \tag{A.9}$$

Therefore

$$\frac{k_{ne}(E)}{k_{nc}(E)} = \frac{1 - f_T}{f_T}\frac{f_n(E)}{1 - f_n(E)}, \tag{A.10}$$

$$\frac{k_{pe}(E)}{k_{pc}(E)} = \frac{f_T}{1 - f_T}\frac{f_p(E)}{1 - f_p(E)}, \tag{A.11}$$

where

$$f_T = \frac{n_T}{N_T}. \tag{A.12}$$

According to Fermi-Dirac probability density function

$$f(E) = \frac{1}{1 + \exp\left(\dfrac{E - E_F}{k_B T}\right)}. \tag{A.13}$$

So for the electrons we have

$$\frac{k_{ne}(E)}{k_{nc}(E)} = \exp\left(\frac{E_T - E_F}{k_B T}\right)\exp\left(-\frac{E - E_F}{k_B T}\right) = \exp\left(\frac{E_T - E}{k_B T}\right), \tag{A.14}$$

and for the holes

$$\frac{k_{pe}(E)}{k_{pc}(E)} = \exp\left(-\frac{E_T - E_F}{k_B T}\right)\exp\left(\frac{E - E_F}{k_B T}\right) = \exp\left(-\frac{E_T - E}{k_B T}\right), \tag{A.15}$$

since

$$f_p(E) = 1 - f_n(E). \tag{A.16}$$

Applying formulas (A.14) and (A.15) in (A.7) and (A.8), and performing simple mathematical operations and also involving the concept of trap's quasi Fermi energy E_{FT} would results in the following formulas for the net generation/recombination rates for electrons and holes

$$dR_n - dG_n = \left(1 - \exp\left(\frac{E_{FT} - E_F}{k_B T}\right)\right)(1 - f_T) f_n(E) k_{ne}(E) g_c(E) N_T dE, \tag{A.17}$$

$$dR_p - dG_p = \left(1 - \exp\left(\frac{E_F - E_{FT}}{k_B T}\right)\right) f_T f_p(E) k_{pe}(E) g_v(E) N_T dE. \tag{A.18}$$

Integration over energies will result in the following formulas for net generation/recombination for electrons and holes

$$R_n - G_n = \left(1 - \exp\left(\frac{E_{FT} - E_F}{k_B T}\right)\right)(1 - f_T) N_T v_{th}^n \int_{E_c}^{\infty} f_n(E) \sigma_n(E) g_c(E) dE, \tag{A.19}$$

$$R_p - G_p = \left(1 - \exp\left(\frac{E_F - E_{FT}}{k_B T}\right)\right) f_T N_T v_{th}^p \int_{-\infty}^{E_v} f_p(E) \sigma_p(E) g_v(E) dE, \tag{A.20}$$

where v_{th}^n and v_{th}^p are the thermal velocities for electrons and holes, respectively, and $\sigma_n(E)$ and $\sigma_p(E)$ are the capture cross sections of electrons and holes such that

$$k_{ne} = v_{th}^n \sigma_n(E), \qquad k_{pe} = v_{th}^p \sigma_p(E). \tag{A.21}$$

By applying the concept of Maxwell-Boltzmann distribution from classical physics for near equilibrium

$$f(E) = \exp(-\frac{E - E_F}{k_B T}), \tag{A.22}$$

and assuming constant values for capture cross sections (which means $\sigma_n(E)$ and $\sigma_p(E)$ are independent of energy so $\sigma_n(E) = \sigma_n$ and $\sigma_p(E) = \sigma_p$) and also

the same thermal velocities for electrons and holes $v_{th}^n = v_{th}^p = v_{th}$, we have

$$R_n - G_n = \left(n - N_c \exp\left(-\frac{E_c - E_F}{k_B T}\right) \exp\left(\frac{E_{FT} - E_F}{k_B T}\right)\right)(1 - f_T) N_T v_{th} \sigma_n, \tag{A.23}$$

$$R_p - G_p = \left(p - N_v \exp\left(-\frac{E_F - E_v}{k_B T}\right) \exp\left(\frac{E_F - E_{FT}}{k_B T}\right)\right) f_T N_T v_{th} \sigma_p, \tag{A.24}$$

where

$$n = N_c \exp\left(-\frac{E_c - E_F}{k_B T}\right), \qquad p = N_v \exp\left(-\frac{E_F - E_v}{k_B T}\right), \tag{A.25}$$

Also N_c and N_v are the effective density-of-states for electrons and holes, respectively.

Allowing $\frac{f_T}{1 - f_T} = \exp(-\frac{E_T - E_{FT}}{k_B T})$ to play a role, the equations (A.23) and (A.24) can be written as follows

$$R_n - G_n = \sigma_n v_{th} N_T \left(n(1 - f_T) - n_1 f_T\right), \tag{A.26}$$

$$R_p - G_p = \sigma_p v_{th} N_T \left(p f_T - p_1 (1 - f_T)\right), \tag{A.27}$$

where

$$n_1 = N_c \exp\left(-\frac{E_c - E_T}{k_B T}\right), \qquad p_1 = N_v \exp\left(-\frac{E_T - E_v}{k_B T}\right). \tag{A.28}$$

The equations can be further simplified by considering the approximations of $n_1 \approx n_i$ and $p_1 \approx n_i$,

$$R_n - G_n = \sigma_n v_{th} \left(n(N_T - n_T) - n_i n_T\right), \tag{A.29}$$

$$R_p - G_p = \sigma_p v_{th} \left(p n_T - n_i (N_T - n_T)\right), \tag{A.30}$$

where n_i is the intrinsic carrier concentration such that $n_1 p_1 = n_i^2$, so

$$n_i = \sqrt{N_c N_v} \exp\left(-\frac{E_c - E_v}{k_B T}\right). \tag{A.31}$$

Publications resulting from this thesis work

Journal papers

- B. Raftari, N.V. Budko and C. Vuik. A modified and calibrated drift-diffusion-reaction model for time-domain analysis of charging phenomena in electron-beam irradiated insulators. *AIP Advances*, 8:015307, 2018.

- H. van der Graaf, H. Akhtar, N.V. Budko, H.W. Chan, C.W. Hagen, C.C Hansson, G. Nützel, S.D. Pinto, V. Prodanović, B. Raftari, P.M. Sarro, J. Sinsheimer, J. Smedley, S. Taoe, A.M.M.G. Theulings and C. Vuik. The tynode: A new vacuum electron multiplier. *Nuclear Instruments and Methods in Physics Research Section A: Accelerators, Spectrometers, Detectors and Associated Equipment*, 847:148–161, 2017. Cited by 4.

- B. Raftari, N.V. Budko and C. Vuik. Self-consistent drift-diffusion-reaction model for the electron beam interaction with dielectric samples. *Journal of Applied Physics*, 118(20):204101, 2015. Cited by 11.

The citations are based on Google Scholar Citations as of September 17, 2018.

Presentation

- Mini-symposium speaker at the 6th International Conference on Advanced COmputational Methods in ENgineering (ACOMEN), Ghent, Belgium, June 23-28, 2014.

- Mini-symposium speaker at the 12th Multinational Conference on Microscopy (MCM2015), Eger, Hungary, August 23-28, 2015.

- Speaker at SEM simulation meeting, Delft, The Netherlands, November 24, 2016.
- Poster Presented at 38th and 40th Woudschoten Conference, Ziest, The Netherlands, 2013 and 2015.

Bibliography

[1] J.S. Lee, J. Cho, C. Lee, I. Kim, J. Park, Y.M. Kim, H. Shin, J. Lee, and F. Caruso. Layer-by-layer assembled charge-trap memory devices with adjustable electronic properties. *Nature Nanotechnology*, 2(12):790–795, 2007.

[2] H. van der Graaf, H. Akhtar, N.V. Budko, H.W. Chan, C.W. Hagen, C.C.T. Hansson, G. Nützel, S.D. Pinto, V. Prodanović, B. Raftari, P.M. Sarro, J. Sinsheimer, J. Smedley, S. Taoe, A.M.M.G. Theulings, and C. Vuik. The tynode: A new vacuum electron multiplier. *Nuclear Instruments and Methods in Physics Research Section A: Accelerators, Spectrometers, Detectors and Associated Equipment*, 847:148–161, 2017.

[3] BM Kulwicki and AJ Purdes. Diffusion potentials in BaTiO3 and the theory of PTC materials. *Ferroelectrics*, 1(1):253–263, 1970.

[4] A.D. Bass, P. Cloutier, and L. Sanche. Measurements of charge accumulation induced by monochromatic low-energy electrons at the surface of insulating samples. *Journal of Applied Physics*, 84(5):2740–2748, 1998.

[5] A.L. Vampola, P.F. Mizera, H.C. Koons, J.F. Fennell, and D.F. Hall. The aerospace spacecraft charging document. Technical report, AEROSPACE CORP EL SEGUNDO CA LAB OPERATIONS, 1985.

[6] B. Gross. Irradiation effects in borosilicate glass. *Physical Review*, 107(2):368, 1957.

[7] B. Gross. Irradiation effects in plexiglas. *Journal of Polymer Science Part A: Polymer Chemistry*, 27(115):135–143, 1958.

[8] B. Gross and S.V. Nablo. High potentials in electron-irradiated dielectrics. *Journal of Applied Physics*, 38(5):2272–2275, 1967.

[9] B. Gross, J. Dow, and S.V. Nablo. Charge buildup in electron-irradiated dielectrics. *Journal of Applied Physics*, 44(6):2459–2463, 1973.

[10] B. Gross, G.M. Sessler, and J.E. West. Charge dynamics for electron-irradiated polymer-foil electrets. *Journal of Applied Physics*, 45(7):2841–2851, 1974.

[11] B. Gross and L.N. de Oliveira. Transport of excess charge in electron-irradiated dielectrics. *Journal of Applied Physics*, 45(11):4724–4729, 1974.

[12] H. Liebl. Sims instrumentation and imaging techniques. *Scanning*, 3(2):79–89, 1980.

[13] R. Le Bihan. Study of ferroelectric and ferroelastic domain structures by scanning electron microscopy. *Ferroelectrics*, 97(1):19–46, 1989.

[14] X. Meyza, D. Goeuriot, C. Guerret-Piécourt, D. Tréheux, and H.J. Fitting. Secondary electron emission and self-consistent charge transport and storage in bulk insulators: Application to alumina. *Journal of applied physics*, 94(8):5384–5392, 2003.

[15] M. Touzin, D. Goeuriot, C. Guerret-Piécourt, D. Juvé, D. Tréheux, and H.J. Fitting. Electron beam charging of insulators: A self-consistent flight-drift model. *Journal of applied physics*, 99(11):114110, 2006.

[16] W.Q. Li, K. Mu, and R.H. Xia. Self-consistent charging in dielectric films under defocused electron beam irradiation. *Micron*, 42(5):443–448, 2011.

[17] W.Q. Li and H.B. Zhang. The surface potential of insulating thin films negatively charged by a low-energy focused electron beam. *Micron*, 41(5):416–422, 2010.

[18] C.G.H. Walker, L. Frank, and I. Müllerová. Simulations and measurements in scanning electron microscopes at low electron energy. *Scanning*, 38(6):802–818, 2016.

[19] G.F. Dionne. Origin of secondary-electron-emission yield-curve parameters. *Journal of Applied Physics*, 46(8):3347–3351, 1975.

[20] A.O. Barut. The mechanism of secondary electron emission. *Physical Review*, 93(5):981, 1954.

[21] B.L. Henke, J. Liesegang, and S.D. Smith. Soft-x-ray-induced secondary-electron emission from semiconductors and insulators: Models and measurements. *Physical Review B*, 19(6):3004, 1979.

[22] E. Kieft and E. Bosch. Refinement of monte carlo simulations of electron–specimen interaction in low-voltage sem. *Journal of Physics D: Applied Physics*, 41(21):215310, 2008.

[23] H.J. Fitting and M. Touzin. Secondary electron emission and self-consistent charge transport in semi-insulating samples. *Journal of Applied Physics*, 110(4):044111, 2011.

[24] N. Cornet, D. Gœuriot, C. Guerret-Piecourt, D. Juvé, D. Tréheux, M. Touzin, and H.J. Fitting. Electron beam charging of insulators with surface layer and leakage currents. *Journal of Applied Physics*, 103(6):064110, 2008.

[25] H.J. Fitting and M. Touzin. Time-dependent start-up and decay of secondary electron emission in dielectrics. *Journal of Applied Physics*, 108(3):033711, 2010.

[26] H.J. Fitting, H. Glaefeke, and W. Wild. Electron penetration and energy transfer in solid targets. *physica status solidi (a)*, 43(1):185–190, 1977.

[27] H.J. Fitting. Transmission, energy distribution, and se excitation of fast electrons in thin solid films. *physica status solidi (a)*, 26(2):525–535, 1974.

[28] H.J. Fitting, H. Glaefeke, W. Wild, and G. Neumann. Multiple scattering of fast electrons and their secondary electron generation within semi-infinite targets. *Journal of Physics D: Applied Physics*, 9(17):2499, 1976.

[29] R. Entner. *Modeling and simulation of negative bias temperature instability*. PhD dissertation, Technische Universität Wien, 2007.

[30] P.A. Markowich, C. Ringhofer, and C. Schmeiser. *Semiconductor equations*. Springer-Verlag New York, Inc., 1990.

[31] W.Q. Li and H.B. Zhang. The positive charging effect of dielectric films irradiated by a focused electron beam. *Applied Surface Science*, 256(11):3482–3492, 2010.

[32] H.B Zhang, W.Q. Li, and M. Cao. Leakage current simulation of insulating thin film irradiated by a nonpenetrating electron beam. *Chinese Physics Letters*, 29(4):047901, 2012.

[33] H.B. Zhang, W.Q. Li, and M. Cao. Space charge characteristics of an insulating thin film negatively charged by a low-energy electron beam. *Journal of Electron Microscopy*, 61(2):85–97, 2012.

[34] H.B. Zhang, W.Q. Li, and D.W. Wu. Contrast mechanism due to interface trapped charges for a buried sio2 microstructure in scanning electron microscopy. *Journal of Electron Microscopy*, 58(1):15–19, 2008.

[35] B. Raftari, N.V. Budko, and C. Vuik. Self-consistent drift-diffusion-reaction model for the electron beam interaction with dielectric samples. *Journal of Applied Physics*, 118(20):204101, 2015.

[36] M. Gritsch. *Numerical modeling of silicon-on-insulator MOSFETs*. na, 2002.

[37] E.R. Kieft. Monte carlo simulation for sem imaging of charging samples: a status overview. Technical report, Philips Research Europe, 2007.

[38] A.L. Shluger, K.P. Mckenna, P.V. Sushko, D.M. Ramo, and A.V. Kimmel. Modelling of electron and hole trapping in oxides. *Modelling and Simulation in Materials Science and Engineering*, 17(8):084004, 2009.

[39] B. Van Zeghbroeck. Principles of electronic devices. *University of Colorado*, 2011.

[40] H. Seiler. Secondary electron emission in the scanning electron microscope. *Journal of Applied Physics*, 54(11):R1–R18, 1983.

[41] M.Y. Doghish and F.D. Ho. A comprehensive analytical model for metal-insulator-semiconductor (mis) devices. *IEEE Transactions on Electron Devices*, 39(12):2771–2780, 1992.

[42] M.Y. Doghish and F.D. Ho. A comprehensive analytical model for metal-insulator-semiconductor (mis) devices: A solar cell application. *IEEE Transactions on Electron Devices*, 40(8):1446–1454, 1993.

[43] E.H. Nicollian and A. Goetzberger. The si-sio$_2$ interfaceelectrical properties as determined by the metal-insulator-silicon conductance technique. *Bell System Technical Journal*, 46(6):1055–1133, 1967.

[44] E.H. Nicollian, J.R. Brews, and E.H Nicollian. *MOS (metal oxide semiconductor) physics and technology*, volume 1987. Wiley New York et al., 1982.

[45] S.M. Sze, D.J. Coleman, and A. Loya. Current transport in metal-semiconductor-metal (msm) structures. *Solid-State Electronics*, 14(12):1209–1218, 1971.

[46] J.W. Jerome. Consistency of semiconductor modeling: an existence/stability analysis for the stationary van roosbroeck system. *SIAM journal on applied mathematics*, 45(4):565–590, 1985.

[47] S. Busenberg, W. Fang, and K. Ito. Modeling and analysis of laser-beam-induced current images in semiconductors. *SIAM Journal on Applied Mathematics*, 53(1):187–204, 1993.

[48] I. Babuska, J.E. Flaherty, W.D. Henshaw, J.E. Hopcroft, J.E. Oliger, and T. Tezduyar. *Modeling, mesh generation, and adaptive numerical methods for partial differential equations*, volume 75. Springer Science & Business Media, 2012.

[49] R. Verfürth. *A review of a posteriori error estimation and adaptive mesh-refinement techniques*. John Wiley & Sons Inc, 1996.

[50] R. Codina. A discontinuity-capturing crosswind-dissipation for the finite element solution of the convection-diffusion equation. *Computer Methods in Applied Mechanics and Engineering*, 110(3-4):325–342, 1993.

[51] A.N. Brooks and T.J.R. Hughes. Streamline upwind/petrov-galerkin formulations for convection dominated flows with particular emphasis on the incompressible navier-stokes equations. *Computer Methods in Applied Mechanics and Engineering*, 32(1-3):199–259, 1982.

[52] T.E. Tezduyar and Y.J. Park. Discontinuity-capturing finite element formulations for nonlinear convection-diffusion-reaction equations. *Computer Methods in Applied Mechanics and Engineering*, 59(3):307–325, 1986.

[53] B. Raftari, N.V Budko, and C. Vuik. A modified and calibrated drift-diffusion-reaction model for time-domain analysis of charging phenomena in electron-beam irradiated insulators. *AIP Advances*, 8(1):015307, 2018.

[54] P.H. Dawson. Secondary electron emission yields of some ceramics. *Journal of Applied Physics*, 37(9):3644–3645, 1966.

[55] Y.C. Yong, J.T.L. Thong, and J.C.H. Phang. Determination of secondary electron yield from insulators due to a low-kv electron beam. *Journal of applied physics*, 84(8):4543–4548, 1998.

[56] K.H. Kim, Z. Akase, T. Suzuki, and D. Shindo. Charging effects on sem/sim contrast of metal/insulator system in various metallic coating conditions. *Materials Transactions*, 51(6):1080–1083, 2010.

[57] D.I. Vaisburd and K.E. Evdokimov. The poole–frenkel effect in a dielectric under nanosecond irradiation by an electron beam with moderate or high current density. *Russian Physics Journal*, 51(12):1255–1261, 2008.

[58] R.C. Hughes. Generation, transport, and trapping of excess charge carriers in czochralski-grown sapphire. *Physical Review B*, 19(10):5318, 1979.

[59] R.C. Hughes. Hot electrons in SiO_2. *Physical Review Letters*, 35(7):449, 1975.

[60] R. Renoud, F. Mady, C. Attard, J. Bigarre, and J.P. Ganachaud. Secondary electron emission of an insulating target induced by a well-focused electron beam–monte carlo simulation study. *physica status solidi (a)*, 201(9):2119–2133, 2004.

[61] P.S. Pickard and M.V. Davis. Analysis of electron trapping in alumina using thermally stimulated electrical currents. *Journal of Applied Physics*, 41(6):2636–2643, 1970.

[62] J. Cazaux. Electron probe microanalysis of insulating materials: quantification problems and some possible solutions. *X-Ray Spectrometry*, 25(6):265–280, 1996.

[63] D.J. DiMaria, L.M. Ephrath, and D.R. Young. Radiation damage in silicon dioxide films exposed to reactive ion etching. *Journal of Applied Physics*, 50(6):4015–4021, 1979.

[64] D.J. DiMaria and J.W. Stasiak. Trap creation in silicon dioxide produced by hot electrons. *Journal of Applied Physics*, 65(6):2342–2356, 1989.

[65] D.J. DiMaria and J.H. Stathis. Trapping and trap creation studies on nitrided and reoxidized-nitrided silicon dioxide films on silicon. *Journal of applied physics*, 70(3):1500–1509, 1991.

[66] D.A. Buchanan, M.V. Fischetti, and D.J. DiMaria. Coulombic and neutral trapping centers in silicon dioxide. *Physical Review B*, 43(2):1471, 1991.

[67] T.H. Ning. Capture cross section and trap concentration of holes in silicon dioxide. *Journal of Applied Physics*, 47(3):1079–1081, 1976.

[68] T.H. Ning. High-field capture of electrons by coulomb-attractive centers in silicon dioxide. *Journal of Applied physics*, 47(7):3203–3208, 1976.

[69] R. Williams. Photoemission of electrons from silicon into silicon dioxide. *Physical Review*, 140(2A):A569, 1965.

[70] C. Feldman. Range of $1 - 10$ kev electrons in solids. *Physical Review*, 117(2):455, 1960.

[71] K. Kanaya and S. Okayama. Penetration and energy-loss theory of electrons in solid targets. *Journal of Physics D: Applied Physics*, 5(1):43, 1972.

[72] V.E. Cosslett and R.N. Thomas. Multiple scattering of 5-30 kev electrons in evaporated metal films ii: Range-energy relations. *British Journal of Applied Physics*, 15(11):1283, 1964.

[73] R.O. Lane and D.J. Zaffarano. Transmission of 0-40 kev electrons by thin films with application to beta-ray spectroscopy. *Physical Review*, 94(4):960, 1954.

[74] J.R. Young. Penetration of electrons in aluminum oxide films. *Physical Review*, 103(2):292, 1956.

[75] K.Y. Yang and R.W. Hoffman. Electron yields and escape depths from kapton and teflon. *Surface and Interface Analysis*, 10(2-3):121–125, 1987.

[76] M. Salehi and E.A. Flinn. An experimental assessment of proposed universal yield curves for secondary electron emission. *Journal of Physics D: Applied Physics*, 13(2):281, 1980.

[77] A. Melchinger and S. Hofmann. Dynamic double layer model: Description of time dependent charging phenomena in insulators under electron beam irradiation. *Journal of Applied Physics*, 78(10):6224–6232, 1995.

[78] M. Belhaj, S. Odof, K. Msellak, and O. Jbara. Time-dependent measurement of the trapped charge in electron irradiated insulators: application to Al_2O_3–sapphire. *Journal of Applied Physics*, 88(5):2289–2294, 2000.

[79] D.C. Joy. A database of electron-solid interactions, revision 08-1, 2008.

[80] M. Dapor. Secondary electron emission yield calculation performed using two different monte carlo strategies. *Nuclear Instruments and Methods in Physics Research Section B: Beam Interactions with Materials and Atoms*, 269(14):1668–1671, 2011.

[81] B.K. Agarwal. Variation of secondary emission with primary electron energy. *Proceedings of the Physical Society*, 71(5):851, 1958.

[82] E. Schreiber and H.J. Fitting. Monte carlo simulation of secondary electron emission from the insulator SiO_2. *Journal of Electron Spectroscopy and Related Phenomena*, 124(1):25–37, 2002.

[83] J. Kwo, M. Hong, A.R. Kortan, K.L. Queeney, Y.J. Chabal, R.L. Opila, D.A. Muller, S.N.G. Chu, B.J. Sapjeta, T.S. Lay, J.P. Mannaerts, T. Boone, H.W. Krautter, J.J. Krajewski, A.M. Sergnt, and J.M. Rosamilia. Properties of high k gate dielectrics Gd_2O_3 and Y_2O_3 for si. *Journal of Applied Physics*, 89(7):3920–3927, 2001.

[84] M. Silver and R. Sharma. Carrier generation and recombination in anthracene. *The Journal of Chemical Physics*, 46(2):692–696, 1967.

[85] L.M. Barker and R.E. Hollenbach. Shock-wave studies of pmma, fused silica, and sapphire. *Journal of Applied Physics*, 41(10):4208–4226, 1970.

[86] T.E. Tsai, D.L. Griscom, and E.J. Friebele. Mechanism of intrinsic Si E´-center photogeneration in high-purity silica. *Physical Review Letters*, 61(4):444, 1988.

[87] M.A. Schildbach and A.V. Hamza. Sapphire ($11\bar{2}0$) surface: Structure and laser-induced desorption of aluminum. *Physical Review B*, 45(11):6197, 1992.

[88] R. Renoud, F. Mady, and J.P. Ganachaud. Monte carlo simulation of the charge distribution induced by a high-energy electron beam in an insulating target. *Journal of Physics: Condensed Matter*, 14(2):231, 2002.

[89] J. Cazaux. Surface potential and electric field induced by electron bombardment of insulators. *IEEE Transactions on Electrical Insulation*, 24(6):995–997, 1989.

[90] J. Cazaux and P. Lehuede. Some physical descriptions of the charging effects of insulators under incident particle bombardment. *Journal of Electron Spectroscopy and Related Phenomena*, 59(1):49–71, 1992.

[91] X. Xiang, X.T. Zu, S. Zhu, Q.M. Wei, C.F. Zhang, K. Sun, and L.M. Wang. Zno nanoparticles embedded in sapphire fabricated by ion implantation and annealing. *Nanotechnology*, 17(10):2636, 2006.

[92] A.l. Meldrum, L.A. Boatner, and K. Sorge. Microstructure and magnetic properties of co nanoparticles in ion-implanted al 2 o 3. *Nuclear Instruments and Methods in Physics Research Section B: Beam Interactions with Materials and Atoms*, 207(1):36–44, 2003.

[93] G. Xiong, Elam J.W., Feng H., Han C.Y., Wang H.H., Iton L.E., Curtiss L.A., Pellin M.J., Kung M., Kung H., and Stair P.C. Effect of atomic layer deposition coatings on the surface structure of anodic aluminum oxide membranes. *The Journal of Physical Chemistry B*, 109(29):14059–14063, 2005.

[94] R. Katamreddy, R. Inman, G. Jursich, A. Soulet, A. Nicholls, and C. Takoudis. Post deposition annealing of aluminum oxide deposited by atomic layer deposition using tris (diethylamino) aluminum and water vapor on si (100). *Thin Solid Films*, 515(17):6931–6937, 2007.

[95] S.J. Jokela, I.V. Veryovkin, A.V. Zinovev, J.W. Elam, A.U. Mane, Q. Peng, Z. Insepov, and the Large Area Picosecond Photodetector Collaboration. Secondary electron yield of emissive materials for large-area micro-channel plate detectors: surface composition and film thickness dependencies. *Physics Procedia*, 37:740–747, 2012.

Curriculum vitae

About the Author

Behrouz Raftari Tangabi was born in Ghasreshirin, Iran, on May 22, 1977. He finished his secondary education in 1996. He entered undergraduate studies of Pure Mathematics at Razi University and he received his BSc degree in 2001. With a top rank in graduate entrance exam, he pursued graduate studies at Amirkabir University of Technology and he obtained his MSc in Applied Mathematics in 2003.

With his sons Sepehr and Sam. The first winter snow of 2017/2018, Delft, The Netherlands.

After completing his MSc, he has had excellent opportunities to teach a wide variety of Mathematics courses over a nine-year career in Azad University of Kermanshah. Simultaneously and for a period of five years, he was lecturer at Razi University. Dedicated to outstanding teaching, he was always among the best math teachers.

As part of work, from 2008 to 2012, he was involved in number research projects which led to several publications in international journals of science and engineering. The focus of the research projects was on the analytical solutions of nonlinear ordinary differential equations. Related to this research topic, he has also reviewed papers for journals such as "Computers and Mathematics with Applications", "Mathematical Methods in the Applied Sciences" , "International Journal of Computer & Mathematics" and "Energy".

In 2013, he started his PhD in Applied Mathematics, conducting research

in the field of mathematical modelling, at Delft University of Technology under supervision of Prof. C. Vuik and Dr. N.V. Budko. His PhD project deals with modelling and simulation of charging phenomena in electron-beam irradiated insulators.

Publications

- B. Raftari, N.V. Budko and C. Vuik. A modified and calibrated drift-diffusion-reaction model for time-domain analysis of charging phenomena in electron-beam irradiated insulators. *AIP Advances*, 8:015307, 2018.

- F. Anvarifar, M. Kok, C. Zevenbergen, W. Thissen, B. Raftari. Cost-effectiveness analysis of reinforcement strategies for (multifunctional) flood defences in the Netherlands. *International Journal of Critical Infrastructures*, 13(4):297–328, 2017.

- H. van der Graaf, H. Akhtar, N.V. Budko, H.W. Chan, C.W. Hagen, C.C Hansson, G. Nützel, S.D. Pinto, V. Prodanović, B. Raftari, P.M. Sarro, J. Sinsheimer, J. Smedley, S. Taoe, A.M.M.G. Theulings and C. Vuik. The tynode: A new vacuum electron multiplier. *Nuclear Instruments and Methods in Physics Research Section A: Accelerators, Spectrometers, Detectors and Associated Equipment*, 847:148–161, 2017. Cited by 4.

- B. Raftari, N.V. Budko and C. Vuik. Self-consistent drift-diffusion-reaction model for the electron beam interaction with dielectric samples. *Journal of Applied Physics*, 118(20):204101, 2015. Cited by 11.

- B. Raftari, H. Khosravi, A. Yildirim. Homotopy analysis method for the one-dimensional hyperbolic telegraph equation with initial conditions. *International Journal of Numerical Methods for Heat & Fluid Flow*, 23:355–372, 2013. Cited by 8.

- B. Raftari. He's variational iteration method for nonlinear jerk equations: Simple but effective. *Shock and Vibration*, 20:351–356, 2013.

- B. Raftari, F. Parvaneh, K. Vajravelu. Homotopy analysis of the magnetohydrodynamic flow and heat transfer of a second grade fluid in a porous channel. *Energy*, 59:625–632, 2013. Cited by 12.

- B. Raftari, H. Adibi, A. Yildirim. Solution of the MHD Falkner-Skan flow by Adomian decomposition method and Pade approximants. *International Journal of Numerical Methods for Heat & Fluid Flow*, 22:1010–1020, 2012. Cited by 4.

- B. Raftari, A. Yildirim. Homotopy perturbation method for heat and Mass transfer in magnetohydrodynamic flow. *Journal of Thermophysics and Heat Transfer*, 26:154–160, 2012. Cited by 2.

- B. Raftari, K. Vajravelu. Homotopy analysis method for MHD viscoelastic fluid flow and heat transfer in a channel with a stretching wall. *Communications in Nonlinear Science and Numerical Simulation*, 17:4149–4162, 2012. Cited by 45.

- B. Raftari, A. Yildirim. Analytical solution of second-order hyperbolic telegraph equation by variational iteration and homotopy perturbation methods. *Results in Mathematics*, 61:13–28, 2012. Cited by 20.

- B. Raftari, A. Yildirim. A new modified homotopy perturbation method with two free auxiliary parameters for solving MHD viscous flow due to a shrinking sheet. *Engineering Computations*, 28:528–539, 2011. Cited by 11.

- B. Raftari, S.T. Mohyud-Din, A. Yildirim. Solution to the MHD flow over a non-linear stretching sheet by homotopy perturbation method. *Science China Physics, Mechanics and Astronomy*, 54:342–345, 2011. Cited by 34.

- B. Raftari, A. Yildirim. The application of homotopy perturbation method for MHD flows of UCM fluids above porous stretching sheets. *Computers and Mathematics with Applications*, 59:3328–3337, 2010. Cited by 81.

The citations are based on Google Scholar Citations as of September 17, 2018.

Aknowledgements

Accomplishing this PhD has been a great experience for me, which would not be possible without the support and guidance that I received from many people.

Foremost, I would like to express my sincere gratitude to both my supervisors Prof. Kees Vuik and Dr. Neil Budko, for the continuous support of my Ph.D study and research. Their guidance and abundant knowledge helped me throughout the research and writing of this thesis.

I am grateful to Thermo Fisher Scientific (formerly FEI), especially to Dr. S. Sluyterman and Dr. E. Bosch, for posing the problem and for the partial financial support. I would also like to thank Prof. H. van der Graaf, Dr. K. Hagen and the rest of the Charged Particle Optics group at TU Delft for many fruitful discussions.

Next, I would like to thank the external members of my thesis committee: Prof. U. Ebert, Prof. B.J. Thijsse, and Prof. A.W. Heemink for their positive feedbacks and comments.

Furthermore, I would like to extend my appreciation to all my friends and colleagues, in particular, Domenico, Rohit, Abdul, Fahim, Reinaldo and Baljaa, for all the great time we have had during the last five years. Special thanks to Anne and Roel for helping me with the Dutch translation of summary and propositions and to Fred, Dennis, Joost, Menel and Thea for their helpfulness.

Moreover, I would like to express my thankfulness to my parents, parents-in-law, brothers, brothers-in-law and my sister for their supports. I am particularly grateful to Masoud and Mahmoud for their unwavering support.

Last but not the least, I would like to express my deepest gratitude to my wife, Maryam, for her great support, understanding, patience and for her presence in the difficult periods. In the end, I want to add two names, Sepehr and Sam, my sons, who are the joy of my life.